Instituto Tecnológico y de Estudios Superiores de Monterrey

Campus Monterrey

School of Engineering and Sciences

Development of SERS substrates for the characterization of cellular systems and the determination of molecules of interest

A dissertation presented by

Iris Anahí Aguilar Hernández

Submitted to the
School of Engineering and Sciences
In partial fulfillment of the requirements for the degree of

Doctor of Philosophy

In

Engineering Science

Monterrey, Nuevo León, December 4th, 2017

Instituto Tecnológico y de Estudios Superiores de Monterrey

Campus Monterrey

School of Engineering and Sciences

The committee members, hereby, certify that have read the dissertation presented by Iris Anahí Aguilar Hernández and that it is fully adequate in scope and quality as a partial requirement for the degree of Doctor of Philosophy in Engineering Science.

Dra. Nancy Edith Ornelas Soto
Tecnológico de Monterrey
School of Engineering and Sciences
Principal Advisor

Dra. Alejandra García García
Centro de Investigación en Materiales Avanzados, S.C.
Committee Member

Tzarara López L.

Dra. Tzarara López Luke
Centro de Investigaciones en Óptica, A.C.
Committee Member

Dra. Diana Linda Cárdenas Chávez
Tecnológico de Monterrey
Committee Member

Dra. Melissa Marlene Rodríguez Delgado
Universidad Autónoma de Nuevo León
Committee Member

Dr. Rubén Morales Menéndez
Dean of Graduate Studies
School of Engineering and Sciences

Tecnológico de Monterrey
04 DIC 2017
Dirección Nacional de Posgrado
Dr. Rubén Morales Menéndez

Monterrey, Nuevo León, December 4th, 2017

Declaration of Authorship

I, Iris Anahí Aguilar Hernández declare that this dissertation titled, *Development of SERS substrates for the characterization of cellular systems and the determination of molecules of interest*, and the work presented in it are my own. I confirm that:

- This work was done wholly or mainly while in candidature for a research degree at this University.
- Where any part of this dissertation has previously been submitted for a degree or any other qualification at this University or any other institution, this has been clearly stated.
- Where I have consulted the published work of others, this is always clearly attributed.
- Where I have quoted from the work of others, the source is always given. With the exception of such quotations, this dissertation is entirely my own work.
- I have acknowledged all main sources of help.
- Where the dissertation is based on work done by myself jointly with others, I have made clear exactly what was done by others and what I have contributed myself.

Iris Anahí Aguilar Hernández
Monterrey, Nuevo León, December 4th, 2017

Acknowledgements

I would like to express my gratitude towards my advisor for the exceptional encouragement and impartial feedback through this enriching and sometimes frustrating PhD.

To my loved ones for their unconditional support and love, and helping me have a well-balanced life.

To everyone in our research group for, the openness and camaraderie.

To the professors and collaborators in CIO and CIMAV for their valuable feedback and willingness to lend a hand when specific equipment was needed.

I would also like to thank CONACyT for the financial support (scholarship #400488) and Tecnológico de Monterrey for covering the full extent of the tuition during the course of this program.

Development of SERS substrates for the characterization of cellular systems and the determination of molecules of interest

By

Iris Anahí Aguilar Hernández

Abstract

Raman spectroscopy is a powerful vibrational spectroscopy technique that provides useful information regarding the chemical composition of a sample. It is a label-free technique that can be successfully applied for both single analyte detection and the analysis of complex matrices. The only main limitation of Raman spectroscopy is the inherent low scattering efficiency. Surface Enhanced Raman Spectroscopy (SERS) is employed to overcome this limitation. SERS active structures are typically in the form of colloidal solutions, or as solid substrates with metallic nanostructures on the surface. The work included in this dissertation explores the development of SERS substrates for (a) the detection of a single molecule of interest, and (b) the analysis of cellular systems.

For the detection of molecules of interest, two studies were carried out: In the first study, the ideal synthesis conditions of colloidal silver nanoparticles that rendered the highest SERS enhancement was explored via principal component analysis (PCA). The selected silver nanoparticles were used for the ultrasensitive detection of phenolic compounds in solution.
The second work focused on the development of solid substrates, where gold nanoparticles were synthesized and immobilized on a carbon nanofibers matrix and enhancement capacity of the SERS substrate was evaluated with Rhodamine 110.

The use of SERS for the analysis of biological systems was also explored. First, the effect of an oxidative agent (CdTe quantum dots) on the freshwater microalgae *H. pluvialis* was studied with SERS via colloidal gold nanoparticles. Mammalian cell lines were also analyzed; Colloidal concave gold nanocubes were synthesized and immobilized onto a solid substrate for SERS enhancement of HeLa cells, showing that solid SERS substrates are also suitable for cell analysis.
Finally, radiation resistant and radiation sensitive murine leukemia sublines were characterized for the first time by normal Raman spectroscopy and SERS, with the aim of contributing the development of predictive radiosensitivity assays.

SERS substrates in colloidal and solid form were developed, and successfully used for the label-free detection of analytes in solution and complex biological samples, showing the versatility of SERS and contributing to this growing multidisciplinary field.

Contents

CHAPTER 1

Introduction

Raman spectroscopy is a vibrational spectroscopy technique that provides valuable information about the structure and functional groups of molecules [1]. When a monochromatic excitation source (laser) interacts with matter, it causes the scattering of light. Scattered light can either (a) the same frequency as the incident source (Rayleigh scattering), or (b) a different frequency from the incident source (Raman scattering) [2]. Therefore, the detected Raman shift is the frequency difference between excitation energy and scattered energy.

Each molecule has a unique Raman signature, thus making this technique highly specific and label-free. Molecules can be identified based on the spectral fingerprint; a complex sample will have a particular spectra arising from the combined Raman scattering of its constituents. Unlike IR spectroscopy, water has very weak Raman signal, making this technique ideal for analysis of aqueous solutions and biological samples [2]. In addition, Raman measurements require minimal to no sample pretreatment, and once the instrumental parameters are established, measurements can take less than a minute to be acquired. Nonetheless, Raman scattering is a relatively weak process, since photons in virtual states are re-irriadiated, and high amount of molecules or sample are needed in order to obtain an adequate spectrum [3]. Therefore, the analysis of complex samples is limited by the low scattering efficiencies encountered at low concentrations [4]. Spectral quality can be improved by using higher laser power, but some samples (e.g. cells and tissues) are susceptible to photo-damage [5].

Surface Enhanced Raman Spectroscopy (SERS) is a technique that allows overcoming the limitations faced by normal Raman spectroscopy at low concentrations. Amplification of Raman signal by SERS requires the interaction of the sample of interest with metallic nanoparticles (see scheme 1). Schlücker [6] summarizes the basic elements of SERS as the conjunction between the specificity (spectral fingerprint) of Raman spectroscopy and high sensitivity attained in the presence of metallic nanostructures that exhibit localized surface plasmon resonance (LSPR).

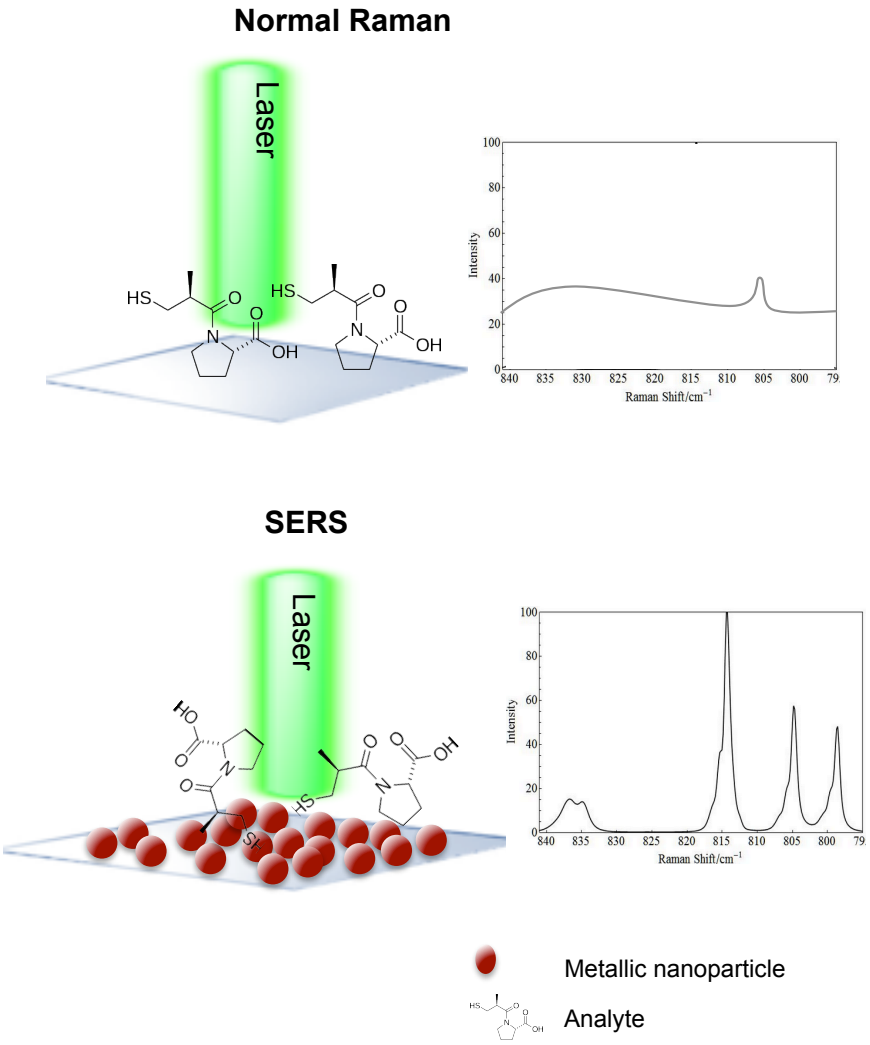

Scheme 1. Normal Raman spectroscopy compared to Surface Enhanced Raman Spectroscopy (SERS).

Fleischman et al. first observed the SERS effect in 1974 when studying analytes adsorbed onto a roughened metallic electrode. Nevertheless, the observed enhancement was incorrectly attributed to the high surface area of the electrode [7]. The correct interpretation of said observations, attributed to surface plasmon excitation, was published almost simultaneously by Albercht and Creighton, and Jeanmarie and Van Duyne in 1977 [8]–[10]. Forty years after its discovery, the exact mechanisms of enhancements are still being studied and debated [11]–[14]. To this point, the consensus is that the observed enhancements [8], [15] are mainly explained by two mechanisms: (a) chemical enhancement or charge transfer, and (b) electromagnetic enhancement (EM) [16], [11].

The chemical enhancement or charge transfer (CT) mechanism depends on the chemisorption of the analyte to a metallic nanostructure, which increases the polarizability of the analyte. This causes an interaction between the electrons of the metal and the molecule [18], where a charge transfer from the analyte to the metal surface takes place [17]. Enhancement factor due to CT

have been calculated at 10^2 and 10^3 orders of magnitude, which is considerably lower than the enhancements reported for the electromagnetic mechanism (10^6-10^{11}) [1].

Electromagnetic enhancement depends on plasmons, which are collective oscillation of delocalized electron [17]. Due to the presence of free electrons in metals, charge separation can be induced by an incident field that induce the oscillation of these electrons. In metallic nanostructures, localized surface plasmons (LSP) occur in the surface, causing an enhancement of the electromagnetic field located in the metallic interface [2]. Localized surface plasmon resonance (LSPR) generates an absorption band in the visible region λ_{max} . This λ_{max} depends on the shape, size, material, surrounding medium and interparticle distance [3]. In order to induce LSP, the incident field (i.e. laser source) must be in resonance with the λ_{max} of the plasmon [1]. Induction of LSP is key for obtaining SERS enhancements. Au and Ag nanostructures are usually used as SERS substrates since their surface plasmon λ_{max} is in the visible range, and correspond to available laser excitation wavelengths (e.g., 514, 633, 785 nm lasers) [6], [8]. In addition, Au and Ag nanostructures can be functionalized, and several functional groups can adsorb and bond to their surface [4]–[6]. SERS enhancement is also dependent on the distance between the analyte and the metallic surface, and can decrease considerably at distances over 20 nm [3]. Interparticle spacings ranging between 1-2 nm can generate coupling or hybridization of the LSP, resulting in higher electromagnetic enhacement [6].
In general, the process of electromagnetic SERS enhancement is described as follows: (1) an incident laser generates the excitation of the LSP; (2) the plasmon interacts with the molecules in proximity/or adsorbed to the surface of metallic nanostructures; (3) the molecule exhibits Raman scattering; (4) energy is transferred back to the plasmon [4]. In this process, both the Raman scattering and the excitation wavelength are enhanced by the LSP[6].

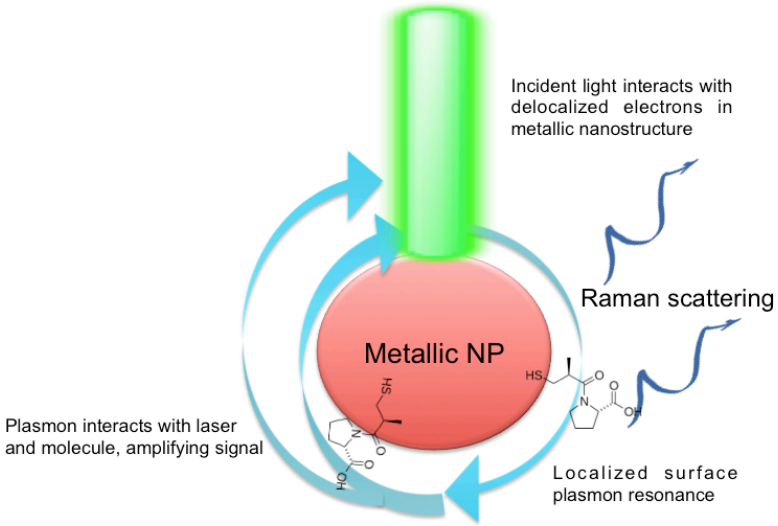

Scheme 2. General process of electromagnetic SERS mechanism.

SERS active systems or substrates are therefore defined as structures that can exhibit localized surface plasmon resonance (LSPR) and generate

Raman signal amplification [15]. SERS substrates can be metallic nanoparticles colloidal form, solid substrates supporting metallic nanostructures, or roughened metallic surfaces. Each type of substrate offers different advantages and limitations, but both types are worth exploring, as SERS enhancements can be tailored by changing the material, shape, size and dielectric environment of the metallic nanoparticles [19], [20]. The presence of aggregates is also a key parameter, since, it allows for the existence of *hot spots* or junctions between nanoparticles where electromagnetic field enhancement of the aggregated nanoparticles is coupled, and in consequence generates a very high and localized enhancement [21]–[23].

Fabrication of SERS substrates can be carried out by top-down and bottom-up methods [24], [25]. Top down methods require the use of specific sophisticated equipment, such is the case of lithographic techniques [26]. These types of SERS substrates allow for highly controlled array distribution and signal reproducibility, but sometimes sacrifice the higher enhancements caused by nanoparticle aggregates or small interparticle distances. Bottom up methods are based on wet-chemical synthesis, and the main advantage is that there is no need for expensive or sophisticated equipment. Changing synthesis parameters allows the tailoring of nanoparticle characteristics such as shape and size, and therefore LSPR excitation and SERS enhancements. In addition, nanostructures can be used as colloidal nanoparticles or immobilized in different materials (e.g. glass, silicon and carbon), depending on the application.

Since the initial observation 40 years ago, SERS has been employed for the detection of molecules in the environmental, biochemical and biomedical field, among others. In addition, SERS can be used to explore chemical changes in complex biological samples such as cells and tissues [17], [27]–[29]. Given the complex spectral signature of real-life samples, chemometric methods like principal component analysis (PCA), partial least squares (PLS) linear discriminant analysis (LDA), support vector machine (SVM), and decision tree, are employed in order to extract the most valuable information from spectral data, as well as data classification [2].
Like normal Raman spectroscopy, SERS analysis generates specific fingerprint of molecules, and it is a promising technique for the development of ultrasensitive sensors.

1.1. Motivation

Most sensing and biosensing applications require high-throughput and ultrasensitive detection. As established previously, the main limitation of normal Raman spectroscopy arises from the low scattering efficiencies, making SERS a technique worth exploring for fast analyte detection.
Recently, SERS substrates fabricated by sophisticated methods have emerged, yet, access to such highly sophisticated and expensive equipment is not available everywhere. The main motivation behind this work is to demonstrate that several SERS active substrates can be developed by cheaper, wet-chemical synthesis methods, and are versatile and efficient

enough to used for a wide array of samples. Finally, these efforts can contribute to the advancement and standardization of SERS-based sensors.

1.2. Problem Statement and Context

Most established techniques employed to characterize the biochemical state of cells depends on either specific fluorescent labeling [30], or chromatographic methods [31]–[33]. Chromatographic methods offer several advantages, but are limited by being labor intensive, destructive techniques that do not allow *in situ* monitoring. Spectroscopic methods like Raman spectroscopy offer a suitable alternative for biochemical characterization of cells and tissue that is non-destructive and label free [1], [34]–[36]. Nevertheless, in the case of biological system, a balance must be met between the signal-to-noise ratio and the laser intensity that is exerted upon the sample to avoid photo-damage [5]. Given that normal Raman scattering is limited at low concentrations, the development of SERS substrates facilitates detecting biomolecules *in situ* without compromising the sample integrity, while maintaining chemical specificity.

In the case of single molecule detection, reaching very low detection limits is key, especially for compounds of environmental concern, where concentrations can be in the order of ng/L [37], [38]. Therefore, it is important to develop alternate qualitative sensing techniques, reaching low levels of detection while fast and label-free.

1.3. Objectives

The main objective is to develop versatile label-free sensors based on Surface Enhanced Raman Spectroscopy (SERS) that allow the detection of molecules of interest, and the analysis of complex biological systems.

Specific objectives of this work are:

I. Synthesis and characterization of SERS-active colloidal metallic nanoparticles.
II. Development of colloidal SERS substrates.
III. Evaluation of colloidal SERS substrates (I,II) as sensors for the detection of a molecule of interest.
IV. Evaluation of colloidal SERS substrates (I,II) for the analysis of a biological system (cells).
V. Development of solid SERS substrate based on the chemical immobilization of metallic nanoparticles.
VI. Evaluation of solid SERS substrates (V) as sensors for the detection of a molecule of interest.
VII. Evaluation of solid SERS substrates (V) for the analysis of a biological system.

References

[1] M. Diem, A. Mazur, K. Lenau, J. Schubert, B. Bird, M. Miljković, C. Krafft, and J. Popp, “Molecular pathology via IR and Raman spectral imaging.,” J. Biophotonics, vol. 6, no. 11–12, pp. 855–86, Dec. 2013.

[2] J. R. Ferraro, K. Nakamoto, and C. W. Brown, Introductory Raman Spectroscopy. 2003.

[3] J. L. Gong, J. H. Jiang, H. F. Yang, G. L. Shen, R. Q. Yu, and Y. Ozaki, “Novel dye-embedded core-shell nanoparticles as surface-enhanced Raman scattering tags for immunoassay,” Anal. Chim. Acta, vol. 564, no. 2, pp. 151–157, 2006.

[4] D. Cialla, A. März, R. Böhme, F. Theil, K. Weber, M. Schmitt, and J. Popp, “Surface-enhanced Raman spectroscopy (SERS): progress and trends.,” Anal. Bioanal. Chem., vol. 403, no. 1, pp. 27–54, Apr. 2012.

[5] H. J. Butler, L. Ashton, B. Bird, G. Cinque, K. Curtis, K. Esmonde-white, N. J. Fullwood, B. Gardner, P. L. Martin-, M. J. Walsh, M. R. Mcainsh, N. Stone, F. L. Martin, H. J. Butler, and P. L. Martin-hirsch, “Using Raman spectroscopy to characterize biological materials,” Nat. Protoc., vol. 11, no. 4, pp. 1–47, 2016.

[6] S. Schlücker, “Surface-enhanced Raman spectroscopy: Concepts and chemical applications,” Angew. Chemie - Int. Ed., vol. 53, no. 19, pp. 4756–4795, 2014.

[7] M. Moskovits, “Surface-enhanced spectroscopy,” Rev. Mod. Phys., vol. 57, no. 3, pp. 783–826, 1985.

[8] K. Kneipp, M. Moskovits, and H. Kneipp, Surface Enhanced Raman Scattering: Physics and Applications, vol. 1. 2006.

[9] J. A. Creighton, C. G. Blatchford, and M. G. Albrecht, “Plasma Resonance Enhancement of Raman Scattering by Pyridine Adsorbed on Silver or Gold Sol Particles of Size,” J. Chem. Soc., Faraday Trans. 2, vol. 75, pp. 790–798, 1979.

[10] D. L. Jeanmaire and R. P. Van Duyne, “Surface raman spectroelectrochemistry,” Journal of Electroanalytical Chemistry and Interfacial Electrochemistry, vol. 84, no. 1. pp. 1–20, 1977.

[11] M. Moskovits, “Persistent misconceptions regarding SERS,” Phys. Chem. Chem. Phys., vol. 15, no. 15, p. 5301, 2013.

[12] E. C. Le Ru, S. a Meyer, C. Artur, P. G. Etchegoin, J. Grand, P. Lang, and F. Maurel, “Experimental demonstration of surface selection rules for SERS on flat metallic surfaces.,” Chem. Commun. (Camb)., vol. 47, no. 13, pp. 3903–3905, 2011.

[13] E. C. Le Ru, E. J. Blackie, M. Meyer, and P. G. Etchegoin, “Surface Enhanced Raman Scattering Enhancement Factors: A Comprehensive Study,” J. Phys. Chem. C, vol. 111, no. 37, pp. 13794–13803, 2007.

[14] K. Faulds, A. Hernandez-Santana, and W. E. Smith, “The inorganic chemistry of surface enhanced Raman scattering (SERS),” in Spectroscopic Properties of Inorganic and Organometallic Compounds, 2010, pp. 1–21.

[15] E. C. LeRu and P. Etchegoin, Principles of surface enhanced Raman spectroscopy and related plasmonic effects, First. Elsevier, 2009.

[16] Y. S. Yamamoto and T. Itoh, “Why and how do the shapes of surface-enhanced Raman scattering spectra change? Recent progress from mechanistic studies,” J. Raman Spectrosc., vol. 47, no. August 2015, pp. 78–88, 2016.

[17] M. K. Hossain, Y. Kitahama, G. G. Huang, X. Han, and Y. Ozaki, “Surface-enhanced raman scattering: Realization of localized surface plasmon resonance using unique substrates and methods,” Anal. Bioanal. Chem., vol. 394, no. 7, pp. 1747–1760, 2009.

[18] K. C. Bantz, A. Meyer, N. Wittenberg, H. Im, and C. L. Haynes, “Recent progress in SERS biosensing,” Phys. Chem. Chem. Phys., vol. 13, no. 24, pp. 11551–11567, 2011.

[19] K. L. Kelly, K. L. Kelly, E. Coronado, L. Zhao, E. Coronado, G. C. Schatz, L. L. Zhao, and G. C. Schatz, “The Optical Properties of Metal Nanoparticles: The Influence of Size, Shape, and Dielectric Environment,” J. Phys. Chem. B, vol. 107, no. 3, pp. 668–677, 2003.
[20] A. Sabur, M. Havel, and Y. Gogotsi, “SERS intensity optimization by controlling the size and shape of faceted gold nanoparticles,” J. Raman Spectrosc., vol. 39, pp. 61–67, 2008.
[21] M. Keating, Y. Chen, I. a Larmour, K. Faulds, and D. Graham, “Growth and surface-enhanced Raman scattering of Ag nanoparticle assembly in agarose gel,” Meas. Sci. Technol., vol. 23, no. 8, p. 84006, 2012.
[22] N. J. Borys, E. Shafran, and J. M. Lupton, “Surface plasmon delocalization in silver nanoparticle aggregates revealed by subdiffraction supercontinuum hot spots,” Sci. Rep., vol. 3, p. 2090, 2013.
[23] Shiohara Amane, Y. Wang, and L. M. Liz-Marzán, “Recent approaches toward creation of hot spots for SERS detection,” J. Photochem. Photobiol. C Photochem. Rev., vol. 21, pp. 2–25, 2014.
[24] B. Sharma, M. Fernanda Cardinal, S. L. Kleinman, N. G. Greeneltch, R. R. Frontiera, M. G. Blaber, G. C. Schatz, and R. P. Van Duyne, “High-performance SERS substrates: Advances and challenges,” MRS Bull., vol. 38, no. 8, pp. 615–624, 2013.
[25] M. Fan and A. G. Brolo, “Silver nanoparticles self assembly as SERS substrates with near single molecule detection limit.,” Phys. Chem. Chem. Phys., vol. 11, no. 34, pp. 7381–9, Sep. 2009.
[26] M. E. Stewart, C. R. Anderton, L. B. Thompson, J. Maria, S. K. Gray, J. a. Rogers, and R. G. Nuzzo, “Nanostructured plasmonic sensors,” Chem. Rev., vol. 108, no. 2, pp. 494–521, 2008.
[27] R. H. Lahr and P. J. Vikesland, “Surface-Enhanced Raman Spectroscopy (SERS) Cellular Imaging of Intracellulary Biosynthesized Gold Nanoparticles,” 2014.
[28] A. F. Palonpon, J. Ando, H. Yamakoshi, K. Dodo, M. Sodeoka, S. Kawata, and K. Fujita, “Raman and SERS microscopy for molecular imaging of live cells.,” Nat. Protoc., vol. 8, no. 4, pp. 677–92, Apr. 2013.
[29] R. a Halvorson and P. J. Vikesland, “Surface-enhanced Raman spectroscopy (SERS) for environmental analyses.,” Environ. Sci. Technol., vol. 44, no. 20, pp. 7749–55, Oct. 2010.
[30] X. Qu, J. Wang, Z. Zhang, N. Koop, R. Rahmanzadeh, and G. Hüttmann, “Imaging of cancer cells by multiphoton microscopy using gold nanoparticles and fluorescent dyes.,” J. Biomed. Opt., vol. 13, no. 3, p. 31217, 2008.
[31] O. Samek, A. Jonáš, Z. Pilát, P. Zemánek, L. Nedbal, J. Tříska, P. Kotas, and M. Trtílek, “Raman microspectroscopy of individual algal cells: sensing unsaturation of storage lipids in vivo.,” Sensors (Basel)., vol. 10, no. 9, pp. 8635–51, Jan. 2010.
[32] P. Bourget, A. Amin, F. Vidal, C. Merlette, and F. Lagarce, “Comparison of Raman spectroscopy vs. high performance liquid chromatography for quality control of complex therapeutic objects: Model of elastomeric portable pumps filled with a fluorouracil solution,” J. Pharm. Biomed. Anal., vol. 91, pp. 176–184, 2014.
[33] G. Wang, Z. Hao, Z. Huang, L. Chen, X. Li, C. Hu, and Y. Liu, “Raman spectroscopic analysis of a desert cyanobacterium Nostoc sp. in response to UVB radiation.,” Astrobiology, vol. 10, no. 8, pp. 783–8, Oct. 2010.
[34] I. Notingher, “Raman Spectroscopy Cell-based Biosensors,” Sensors, vol. 7, no. 8, pp. 1343–1358, Jul. 2007.

[35] J. Kneipp, H. Kneipp, M. McLaughlin, D. Brown, and K. Kneipp, “In vivo molecular probing of cellular compartments with gold nanoparticles and nanoaggregates.,” Nano Lett., vol. 6, no. 10, pp. 2225–31, Oct. 2006.
[36] E. Brauchle, S. Thude, S. Y. Brucker, and K. Schenke-Layland, “Cell death stages in single apoptotic and necrotic cells monitored by Raman microspectroscopy.,” Sci. Rep., vol. 4, p. 4698, Jan. 2014.
[37] S. Huntscha, H. P. Singer, C. S. McArdell, C. E. Frank, and J. Hollender, “Multiresidue analysis of 88 polar organic micropollutants in ground, surface and wastewater using online mixed-bed multilayer solid-phase extraction coupled to high performance liquid chromatography-tandem mass spectrometry,” J. Chromatogr. A, vol. 1268, pp. 74–83, 2012.
[38] M. S. Kostich, A. L. Batt, and J. M. Lazorchak, “Concentrations of prioritized pharmaceuticals in effluents from 50 large wastewater treatment plants in the US and implications for risk estimation,” Environ. Pollut., vol. 184, pp. 354–359, 2014.
[39] M. Fan, G. F. S. Andrade, and A. G. Brolo, “A review on the fabrication of substrates for surface enhanced Raman spectroscopy and their applications in analytical chemistry.,” Anal. Chim. Acta, vol. 693, no. 1–2, pp. 7–25, May 2011.

CHAPTER 2
Single molecule detection

Surface Enhanced Raman Spectroscopy of Phenolic Antioxidants: A Systematic Evaluation of Ferulic Acid, *p*-Coumaric Acid, Caffeic Acid and Sinapic Acid

This chapter has been published as:
I. Aguilar-Hernández, et al., Vib. Spectrosc. 89 (2017) 113–122.
DOI:10.1016/j.vibspec.2017.02.002

Chapter 2

Surface Enhanced Raman Spectroscopy of Phenolic Antioxidants: A Systematic Evaluation of Ferulic Acid, *p*-Coumaric Acid, Caffeic Acid and Sinapic Acid

1. Introduction

Ferulic acid, *p*-coumaric acid, caffeic acid and sinapic acid are examples of important natural phenolic antioxidants [1]. Due to the potential beneficial effects of these compounds regarding human health, considerable evidence about other properties such as UV-protection, anti-carcinogenic and anti-inflammatory properties, as well as cardiovascular protection have been reported [2]–[5]. Phenolic acids are rarely found in their free forms [6], [7]. Nonetheless, studies indicate that free phenolic compounds show an increase of their antioxidant capacity. Other studies about bioavailability indicate that free ferulic acid can be absorbed along the entire gastrointestinal tract, furthermore, free *p*-coumaric acid is also rapidly absorbed, but in an intact form [7]. Moreover, these compounds by themself, have many industrial applications, for example, they can be used as natural preservatives for foods, and applied in the production of paints, paper, and cosmetics [8]. Therefore, there is an increasing development of methods for liberation of natural antioxidants from plant materials for industrial applications [9], [10]. Characterization and quantification of phenolic compounds can be determined by various analytical instrumental methods of which liquid chromatography is the technique of choice, allowing to reach limits of detection in the order of 10^{-8} to 10^{-12} M [11]–[16]. However, in some cases, factors such as costs, real-time implementation of analysis, assortment of standards, use of solvents and pretreatment of samples can restrict the use of chromatography methods, thus limiting a high-throughput analytical quality control [17].

Raman spectroscopy is a well-known non-destructive vibrational technique for structural analysis and quantification of molecules. The fast analytical response and the safe contextual analysis to get measurements leading to a non-intrusive property [18]–[20] are only limited by the low scattering efficiency [21] which can restrict its applicability for analytes at low levels of concentration. To enhance the Raman scattering efficiency [22], [23], the use of particles of noble metals (e.g., Ag, Au) in the 10–100 nm size range is a procedure to create hot spots that ultimately interact with the analyte to produce resonant vibronic coupling of the adsorbate's vibration to the plasmon's transition dipole [24]–[28]. Such mechanism requires the formation of a metal–adsorbate chemical bond, sometimes referred as a first-layer effect [29]. Over the years, surface enhanced Raman scattering (SERS) has proven to be a powerful platform for the quantitative trace analysis of a large number of biomolecules including amino acids [30]–[32], proteins [33]–[35], DNA [36], [37], and in vivo detection of analytes in cellular environments [38]–[41]. Owing to the benefits of using the SERS technique for quantitative detection of important bioactive molecules [42]–[45] several factors have to be taken into consideration [46]. In particular nanoparticle size, shape and aggregation,

as well as the type of substrate (e.g., colloids and solid state) employed, and the pH of the solution studied are subjected to a more refined quality assessment to gain a criteria of sensitivity [47]. A survey of the literature reveals that a few SERS-based studies were focused on the collection of quantitative results in which the limits of detection have been well established [34], [48]–[51].

The main objective of this study was to develop a SERS method for the identification of four free phenolic antioxidants, namely, ferulic acid, *p*-coumaric acid, caffeic acid and sinapic acid. Principal Component Analysis (PCA) was applied and performed to classify the as-prepared silver colloids based on the concentration of reagent employed and the nanoparticle size obtained (including their aggregation). Semi-quantitative analysis with glycine as the probe molecule was carried out to gain an insight into the sensitivity in the SERS-determination for the phenolic compounds. The method proposed is more sensitive for detection of *p*-coumaric acid and caffeic acid than previous reports [42]–[45], [52] in which the limits of detection are within the range of 10^{-3} to 10^{-4} M. In this study, for the first time, the SERS-detection of sinapic acid is reported; the lowest limit of detection reached was in the order of 10^{-9} M.

2. Experimental details

2.1. Chemicals and reagents

Silver nitrate ($AgNO_3$, 99%), sodium borohydride ($NaBH_4$, 99%), glycine (Gly, 99%), ferulic acid (4-hydroxy-3-methoxy cinnamic acid, >98%), *p*-coumaric acid (3-(4-hydroxyphenyl)-2-propenoic acid, >98%), caffeic acid (3-(3,4-dihydroxyphenyl)-2-propenoic acid, >98%), sinapic acid (4-hydroxy-3,5-dimethoxy-cinnamic acid, >98%), nitric acid (HNO_3, 70%) and ethanol analytical pure reagent were purchased from Sigma–Aldrich. All the reagents are reactive grade and were used without additional purification. When it was required, aqueous solutions were prepared using ultrapure water (18.2 MΩ cm^{-1}) purified with a Milli-Q® System (Millipore Corp., USA).

2.2. Preparation of SERS-active silver colloids

Silver colloids were prepared by a modified Creighton method [53]. A stock solution was made by adding 10 mL of $AgNO_3$ (3.5 mM) dropwise to 30 mL of freshly prepared $NaBH_4$ solution (7 mM) cooled in an ice bath. The reaction was carried out in an open system under continuous stirring for 3 min [54]. Aging of the stock solution after synthesis was varied from 15 to 80 min, a factor that can influence in the size and aggregation of colloidal particles produced. Afterwards, aliquots of stock solution were transferred to clean beakers and diluted with deionized water to attain the final concentrations. A total number of 41 different silver colloidal suspensions were prepared by varying both the aging and final concentration (Table 1), which all were kept in darkness. No additional stabilizing agents besides excess $NaBH_4$ were used in order to prevent undesirable salt-mediated reactions [55].

2.3. Silver colloid characterization

The formation of silver nanoparticles (AgNPs) was confirmed by UV-Vis spectroscopy and transmission electron microscopy (TEM). All the UV-Vis absorption spectra of the silver colloidal solutions were obtained over the region from 325 to 550 nm using a photodiode array Agilent 8453 UV-Visible spectrophotometer (Agilent Technologies, Waldbronn, Germany). The morphology of AgNPs was investigated with a Morgagni 268 electron microscope (FEI, Co) operated at 80 kV.

TEM samples were prepared by casting 5 mL of selected colloidal samples onto carbon coated copper grids (Ted Pella, Redding, CA). Excess solution was then removed with paper filter and dried at room temperature for approximately 60 min. The average diameters of the nanoparticles were determined using ImageJ 1.43u software (Wayne Rasband National Institutes of Health, USA).

2.4. Principal Component Analysis

UV-Vis absorption spectra measurements taken from silver colloidal suspensions were analyzed by Principal Component Analysis (PCA) to cluster the colloids synthesized with different concentration of precursor and aging period of the stock solution. PCA is a useful statistical tool to estimate the effect of the preparation of colloids since PCA can reduce the dimensionality of a data set by finding an alternative set of coordinates called principal components [56]. This analysis linearly transforms a data matrix, which

contains information related to the UV-Vis absorption spectra, to new variables of few dimensions (e.g., concentration of reagents, nanoparticle size and aggregation). Thus the PCs are ranked according to their variance; PC1 corresponds to the new variable with the maximum variance (i.e., concentration of silver), and PC2 is the second variable (i.e., size of AgNPs) that contains all of the information not included in PC1. The score values of the principal components were used to associate the as-obtained silver colloids in clusters according to trends in the data obtained. Data analysis was carried out using The Unscrambler® X version 10.1 software package.

2.5. Surface-enhanced Raman spectra measurements

SERS measurements were acquired using a LabRam HR 800 Raman spectrometer (Horiba Scientific, France) equipped with a He-Ne laser (15 mW) operating at 633 nm. A 40 mm objective lens was used for sample focusing; the collection of Raman spectra were accumulated over 4 s. Scattered light was collected by a CCD camera thermoelectrically cooled at –70 ºC. Raman scattering was dispersed with a 200 lines/mm grating, which resulted in spectra in the range from 400 to 2600 cm^{-1}. SERS spectra were recorded in 1-mL quartz cells filled with silver colloidal mixed with the required amount of analyte.

2.5. Analysis of antioxidants

The effect of pH on the SERS enhancement was studied by mixing each analyte (FA, 4CA, CA and SA) with the silver colloid to obtain a final concentration of $7.5x10^{-6}$ M. The concentration was fixed, and pH was varied in a range from 2 to 12 using HNO3. The pH of the solution was measured with a pH meter.

For studying the variation of SERS spectra with concentration, a stock solution of $1x10^{-2}$ M of each analyte and silver colloid were mixed in a final volume of 1 mL, to obtain working concentrations between 2.5×10^{-9} M and 7.5×10^{-6} M. pH of the solution was 6.5, 6.3, 5.5 and 6.3 for FA, 4CA, CA and SA, respectively.

The area under the curve of each SERS spectra was calculated in the range of 1100 to 1700 cm^{-1} using the Origin 9.1 software package.

3. Results and discussion

3.1. Characterization of silver colloids

Aging time of the stock solution can allow the formation of individual nanoparticles of different sizes [30]. Subsequent dilution can induce precipitation [57] since the concentration of $NaBH_4$ is reduced. Such differences can be highlighted as the systematic changes observed in the shape of the UV-Vis absorption bands (e.g., broadening absorbance peak, shoulders and lmax shifts). The UV-Vis absorption spectra of the colloidal suspensions are shown in Figure 1A. It can be observed that the position of the main surface plasmon resonance peak is located at around 390 nm, providing evidence of AgNPs formation. Also, a pale yellow solution is a good indication that the chemical reaction took place and that the seeds available in the solution ranges from 5 to 20 nm in diameter, in agreement with previous studies reported elsewhere [30], [58]. In Figure 1A, the sharpness of some peaks suggests the uniqueness of the particle-size when the peak width half medium (PWHM) is approximately 25 nm. On the other hand, the existence of colloids with several particle sizes was observed through the formation of dark-brown color solutions, in which their corresponding absorption bands show the emergence of shoulders, which can be related with the presence of particles of different size [59], [60]. A red shift in the λ_{max} indicated the formation of larger particles [61], [62] whose bands of absorption are broader and located at 406 nm.

PCA analysis was carried out to cluster the colloidal suspensions according to variances in concentration, aggregation and size of nanoparticles. Table 1 shows the conditions of preparation of the used colloids. As observed in Figure 1C, the score plot of PC1 (88% of the total variance) *versus* the score plot of PC2 (9% of the total variance) separates the colloids in clusters that were grouped in the four quadrants. Samples of colloids observed in both the left and right side (e.g., colloids 3, 6, 8, 9, 11, 12, 14, 16, 28, etc.) were not clustered by the PCA since they correspond either the lowest or the highest concentrations tested respectively. However, several colloids were clustered at the center of the plot, which can be distinguished by variances along the PC1 and PC2 axes. In particular, the PC2 axis spans the variation in the nanoparticle size and aggregation, from large-aggregated (bottom) to small (top). The colloids prepared with a intermediate values of concentration are located at the center, namely, (A) the colloids obtained within an aging period of 60-80 min, which showed a largest nanoparticle sizes and aggregation ($-2 < PC2 < -1$); (B) the colloids obtained within a period between 15 and 30 min, which showed medium nanoparticle sizes ($-0.5 < PC2 < 0.5$); and finally (C) the colloids obtained within aging periods from 45-60 minutes, which exhibited the smallest nanoparticle sizes ($0.5 < PC2 < 1.5$). In the synthesis of the colloids, the reducer is also used as stabilizer ($NaBH_4$), therefore, the aging time affects not only the aggregation but also the nanoparticle size. These features confer together differentiation among UV spectra, which is reflected in the PCA study.

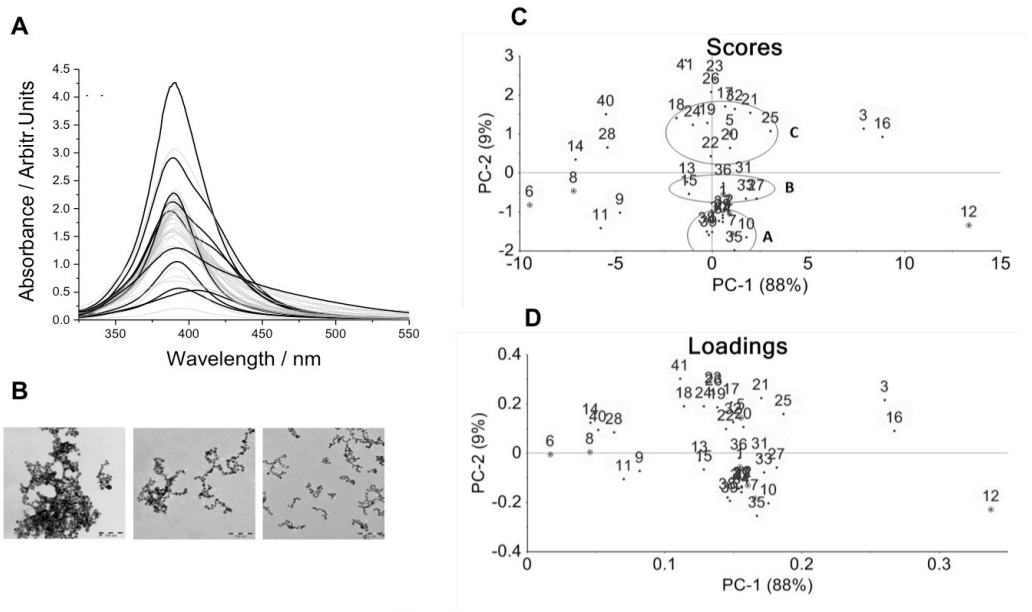

Figure 1. A) UV-Vis spectra of the synthesized Ag colloids. B) Representative TEM micrographs of colloids with high and low levels of aggregation (Left and right). C) PCA score plot and D) PCA loadings.

Representative TEM images of silver colloids are shown in Figure 1B. Although sample preparation for TEM measurements can impact the morphology of the nanoparticles, this technique has been used to reinforce the observations derived from the UV-spectra analysis regarding size and nanoparticle aggregation between selected colloids [7]. It was observed that AgNPs are predominantly spherical in shape. The profile measurements showed that the diameter of these particles is roughly 2-15 nm (small size), 3-20 nm (medium size) and 8-30 nm (large size). Moreover a lower degree of aggregation was observed for the colloids in which individual particles display an average size of about 8.5±3 nm (Fig. 1B, right, while the colloids with larger particles of 19.0 ± 2 nm showed a high level of aggregation (Fig. 1B, left). These observations suggested that the aging period of the stock solution could induce changes in the size and aggregation of the AgNPs.

Table 1. Synthesis conditions for silver colloids

AgNPs colloid	Stock aging time (min)	pH-value	$[AgNO_3]_f$ (mM)	$[NaBH_4]_f$ (mM)
1	30	8.04	0.15	0.87
2	65	8.02	0.15	0.87
3	15	8.35	0.22	1.31
4	60	7.99	0.15	0.87
5	50	8.38	0.15	0.87
6	15	7.94	0.01	0.20
7	65	8.21	0.15	0.87
8	45	7.90	0.08	0.48
9	45	8.38	0.10	0.58
10	60	8.00	0.15	0.87
11	45	8.01	0.10	0.58
12	45	8.20	0.29	1.75
13	20	8.02	0.15	0.87
14	15	7.95	0.08	0.48
15	30	8.00	0.15	0.87
16	15	8.38	0.22	1.31
17	50	8.04	0.15	0.87
18	45	8.00	0.15	0.87
19	45	7.99	0.15	0.87
20	50	8.05	0.15	0.87
21	50	8.00	0.15	0.87
22	45	8.01	0.15	0.87
23	55	8.02	0.15	0.87
24	45	8.00	0.15	0.87
25	50	8.02	0.15	0.87
26	55	7.99	0.15	0.87
27	30	8.04	0.15	0.87
28	15	7.95	0.10	0.58
29	65	8.02	0.15	0.87
30	65	8.02	0.15	0.87
31	30	8.00	0.15	0.87
32	50	7.98	0.15	0.87
33	30	8.05	0.15	0.87
34	65	8.03	0.15	0.87
35	75	8.00	0.15	0.87
36	25	8.02	0.15	0.87
37	65	8.04	0.15	0.87
38	70	8.00	0.15	0.87
39	80	8.04	0.15	0.87
40	15	7.90	0.10	0.58
41	55	8.00	0.15	0.87

3.2. Evaluation of SERS-active silver colloids with a probe molecule

Selected silver colloids from PCA clusters A, B and C, as well as non-clustered colloids were used to test the SERS activity using glycine (Gly) as a probe molecule with well known Raman and SERS peaks [63]–[65] in order to identify the optimal conditions of colloidal synthesis which allows the formation of hotspots caused by particle aggregation [66] and their further use for study of antioxidants.

The enhancement in the intensity of glycine (2.5×10^{-3} M) by using different AgNPs colloids against normal Raman scattering (1M) is shown in Fig. 2. The pH for all the synthesized colloids was adjusted to a value of 8.0 to promote deprotonation of COOH (pKa = 2.3, carboxylate) [30], [31], [63]. Therefore, the interaction of Gly with AgNPs was highly improved using a higher population of molecules with negative partial charges (i.e., Gly anion). As compared to the corresponding Raman spectrum, the SERS enhancement observed can be particularly remarked for the peak assigned to a symmetric stretching vibration for the carboxylate group ($–COO^–$) at ~1382 $cm^{–1}$. Such vibration corresponds to the adsorption of the amino acid onto the surface of AgNPs through the carboxylate [14]; there is no indication of the 1600-$cm^{–1}$ vibration related to the carboxyl group (–COOH) [15]. As Fig. 2 shows, the highest SERS intensities were obtained for colloids located at PC1>0, while lowest intensities were obtained for colloids located at PC1< 0. In particular, high intensities were observed for the colloids 2 and 7 located in cluster A. Moreover, it was observed that low nanoparticle concentration (e.g., colloids 6 and 8) produced no significant signals. According to PCA analysis, those colloids have a suitable nanoparticle size to allow detection of analytes at very low levels of concentration; nonetheless, a certain degree of nanoparticle aggregation [56, 57] is needed in order to obtain the enhancement. PCA analysis (PC2 < 0) suggested that the colloids obtained by aging stock solution between 60 and 80 min and high concentration can produce the highest enhancement of SERS signals (e.g. colloid 12). Therefore one of the most critical parameter on the SERS enhancement is the nanoparticle aggregation, possibly due to the number of active sites upon which the analytes are adsorbed, as reported for molecules like nile blue [19] caffeine [54], tryptophan [30] and proteins [48].

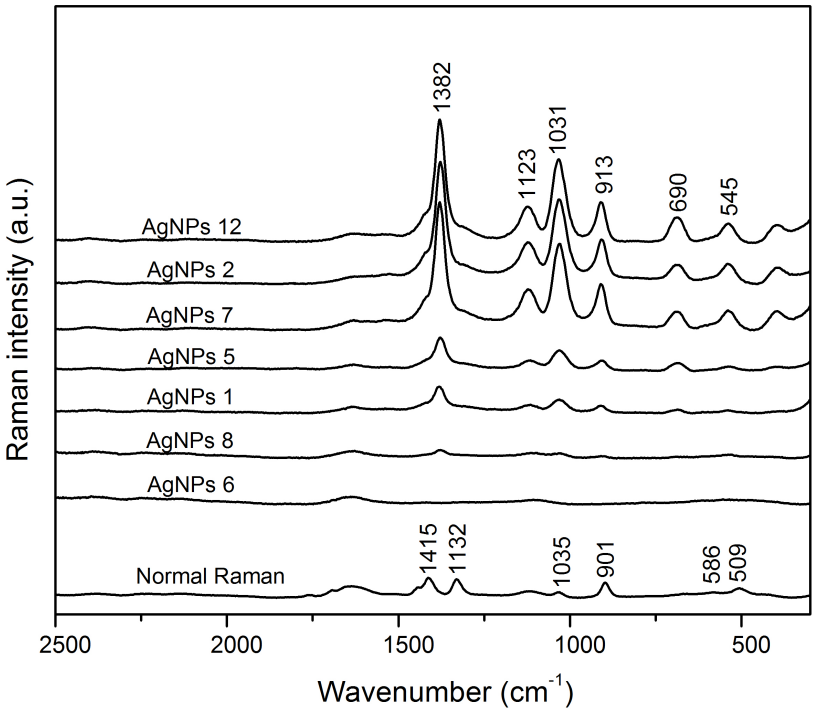

Figure 2. Comparison of normal Raman and SERS spectra of Gly adsorbed on several Ag colloids. These colloids are circled in the PCA scatter plot. Gly concentration was 1 M for normal Raman and $2.5x10^{-3}$ M for SERS test. Both measurements were carried out in solution. Spectra are ordered from highest to lowest signal enhancement.

3.3. SERS-based method for systematic evaluation of antioxidants

SERS spectra of ferulic acid (FA), *p*-coumaric acid (4CA), caffeic acid (CA) and sinapic acid (SA) obtained with silver colloidal solutions are shown in Figure 3. Initially, the SERS-active silver colloids tested were the samples 7, 2, 12, allocated in those variances representing the values PC1> 0 and PC2 <0 since they have shown high performance for SERS effect (data not shown). Finally, colloid 12 was employed for all further experiments with antioxidants. In Figure 3, FA, 4CA, CA and SA analytes were used with a concentration of 7.5×10^{-6} M, which was the highest concentration analyzed by SERS technique in this work, and where the peaks are more defined for their respective assignment. For comparison, the normal Raman spectra were obtained from a film made by drop casting an aliquot of 1 M solution of antioxidants molecules onto aluminum substrates and followed by air-drying. The background (i.e., silver colloids) level is as low as constant that do not contribute to the signals detected. Band assignments obtained from Raman and SERS measurements are provided in Table 2.

Table 2. Raman and SERS vibrational frequencies (in cm^{-1}) of ferulic acid (FA), *p*-coumaric acid (4CA), caffeic acid (CA) and sinapic acid (SA) and their tentative band assignments.

SERS (cm^{-1})				Assignment
FA	4CA	CA	SA	
487		485	502	*o*-dyphenlyl deformation, ring out-of-plane bending
	561	574		COO- in-plane bending
		752		C-H and C-C out-of-plane bending
			899	C-C stretching, C-OO- stretching
958	977	969	973	Out-of-plane C-H bending
		1107		-OH bending
1126	1162	1164	1156	In-plane C-H bending
1219	1238	1221	1284	C-O stretching
1360	1372	1351	1345	$-COO^-$ stretching
	1420	1435		Phenyl ring stretch, -OH bending, C-O stretching
1479			1452	$-OCH_3$ bending, -OH bending
1521	1584	1492	1580	C=C stretching
1605	1622	1599	1624	Phenyl ring deformation

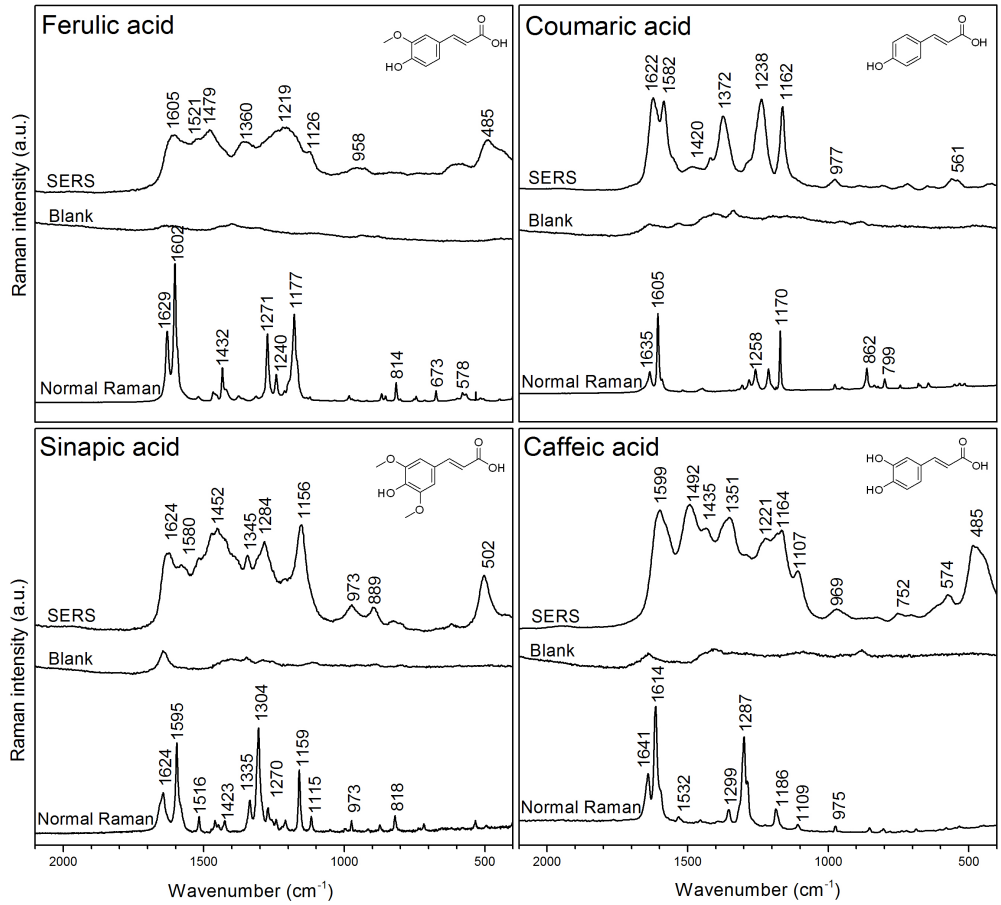

Figure 3. SERS (7.5×10^{-6} M), Ag colloid blank and normal Raman spectra (1M) of CA, FA, 4CA and SA. The Ag colloid blank consists of 2.56% of EtOH, 97.44% of AgNP colloid and was adjusted to pH 6.44 with HNO_3. Spectra are average of 5 individual measurements.

The main characteristic bands located in the SERS spectra are the stretching-type modes of the –COO^- moieties and C=C bonds that leads to deformation of phenyl rings. The symmetric –COO^- stretching appeared at 1360, 1372, 1351 and 1345 cm^{-1} while the C=C [52], [68] stretching were observed at 1521, 1584, 1492 and 1580 cm^{-1} for FA, 4CA, CA and SA analytes, respectively. The phenyl ring deformations appeared as intense bands at 1605, 1622, 1605 and 1624 cm^{-1} in the corresponding spectrum. The bands located at 1126, 1162, 1164 and 1156 cm^{-1} can be attributed to in-plane C–H bending vibrations, while the bands at 958, 977, 969 and 973 cm^{-1} may be assigned to out-of-plane C–H bending vibrations for FA, 4CA, CA and SA, respectively. The difference observed in the wavenumbers and relative intensities is explained in terms of physical adsorption of the analytes to the AgNPs surface [69, 70]. For instance, the presence of the band in the region 1370-1340 cm^{-1} pointed out a possible interaction via the carboxylate group. However, a close inspection reveals that the adsorption can also take place through other different conformations. This is the case for CA, in which the existence of two bands in the region 580-480 cm^{-1} suggested that the adsorption occurred through the *o*-diphenyl moiety, and thus the analyte can be adsorbed to AgNPs through a perpendicular orientation [46]. Moreover, the appearance of a high intensity band seen at 485 cm^{-1} was related to polymerization of CA [45]. In the case of FA, the SERS spectrum also showed the aforementioned bands but in contrast to CA, a broader and low intensity band was observed at about 550-500 cm^{-1}. In the cases of 4CA and SA, there was observed only a weak band at 561 and 502 cm^{-1}, respectively. The evident change observed at this region is a consequence of the chemical nature of the analytes, and thus can be directly dependent of the sum of the surface effects (e.g., electronic effects, steric hindrance and pH of the solution). Finally, the normal Raman spectra for each antioxidant (1 M) were obtained and compared to the corresponding SERS spectrum (1×10^{-6} M). The SERS enhancement factor ($EF = I_{SERS}/I_R \times C_R/C_{SERS}$) was calculated for the peak at about 1610 cm^{-1} and thus was estimated to be approximately 5.4×10^5. This definition is particularly suited to the case of SERS active liquids such as the case of colloidal solutions [71].

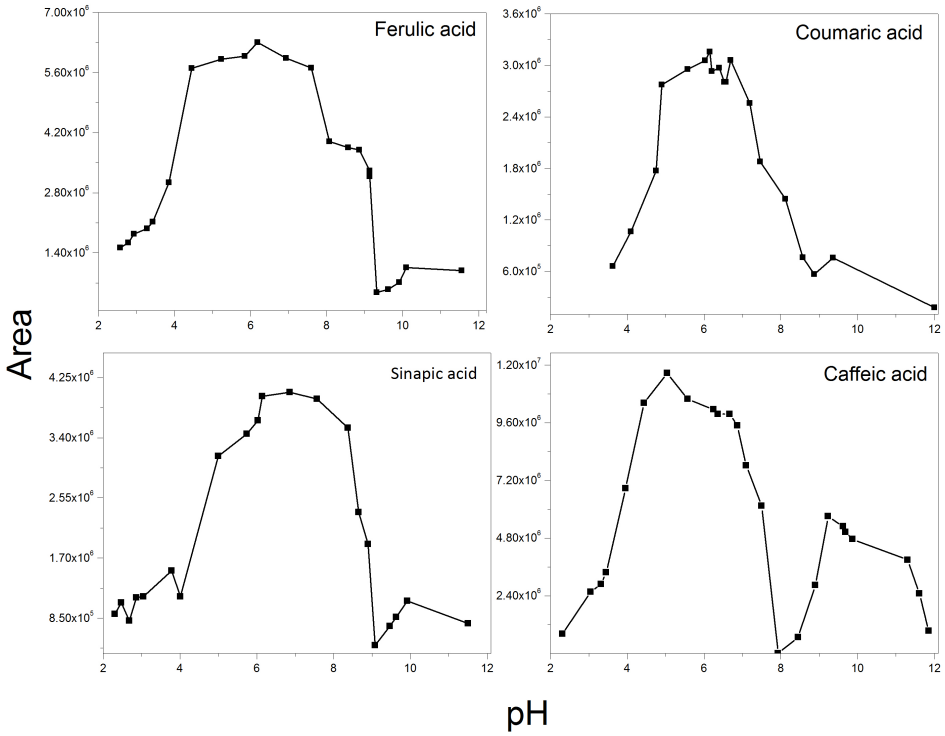

Figure 4. Dependence of SERS intensity on the pH value. Concentration was fixed at 7.5x10^{-6}M and the pH was modified from 2 to 12 and the SERS spectra were acquired for each value. The area under the curve was calculated for peaks in the region between 1100 and 1700 cm^{-1}.

Figure 4 shows the pH dependence for SERS spectra of phenolic antioxidants obtained in the pH range of 2 to 12. The SERS spectra were obtained and the areas were calculated for the spectral region between 1100 and 1700 cm^{-1}. This range was used to calculate absolute SERS enhancement, since the pH variations could affect the molecular conformation of the analyte and hence its interaction with the colloid surface. The maximum areas were observed at pH values from 5.0 to 6.5. The SERS spectra changed at different pH values, which suggested that the adsorption orientation on nanoparticles is pH-dependent [72]. Based on the pKa values [20] corresponding to the –COOH groups of the antioxidants analyzed (see Scheme 1), the latter indicated that the chemical analyte–AgNPs interaction occurred in anionic form (i.e., such as a carboxylate), as observed for Gly. At the more acidic pH values, the overall spectral quality is totally modified giving rise to smaller areas. Those changes in the spectrum can be attributed to decomposition of analytes. However, it is also well known that SERS spectra are elusive to detection because of the instability of colloids under extreme pH conditions [74]. Therefore, a less dramatically change in the SERS spectra was observed up to pH values within 7 and 7.5, which suggested the interaction of carboxylate group. It is noteworthy that other anionic species can be formed due to partial deprotonation of the –OH groups. Taking into account the second pKa value [73] of the antioxidants studied, it was observed that very weak bands in the SERS spectrum were obtained at pH > 9 values. For the case of CA,

enhancement of SERS signals were observed at basic pH values within 8 and 10, probably due to a reorientation of analyte on the silver surface. Thus, the enhancement in the SERS spectra was corroborated by the appearance of a strong band attributed to the phenol n(C–O) stretching vibration located at 1219, 1238, 1221 and 1284 cm^{-1} for FA, 4CA, CA and SA, respectively. The adsorption of the second anionic structure onto AgNPs may stabilize the phenolate form of antioxidants; however experimental limitations hinder the observation of a possible Ag–O interaction (~250-350 cm^{-1}) [75,76]. As a whole, these results pointed out the importance of the pH value to attain reproducible SERS spectra when using silver colloidal solutions.

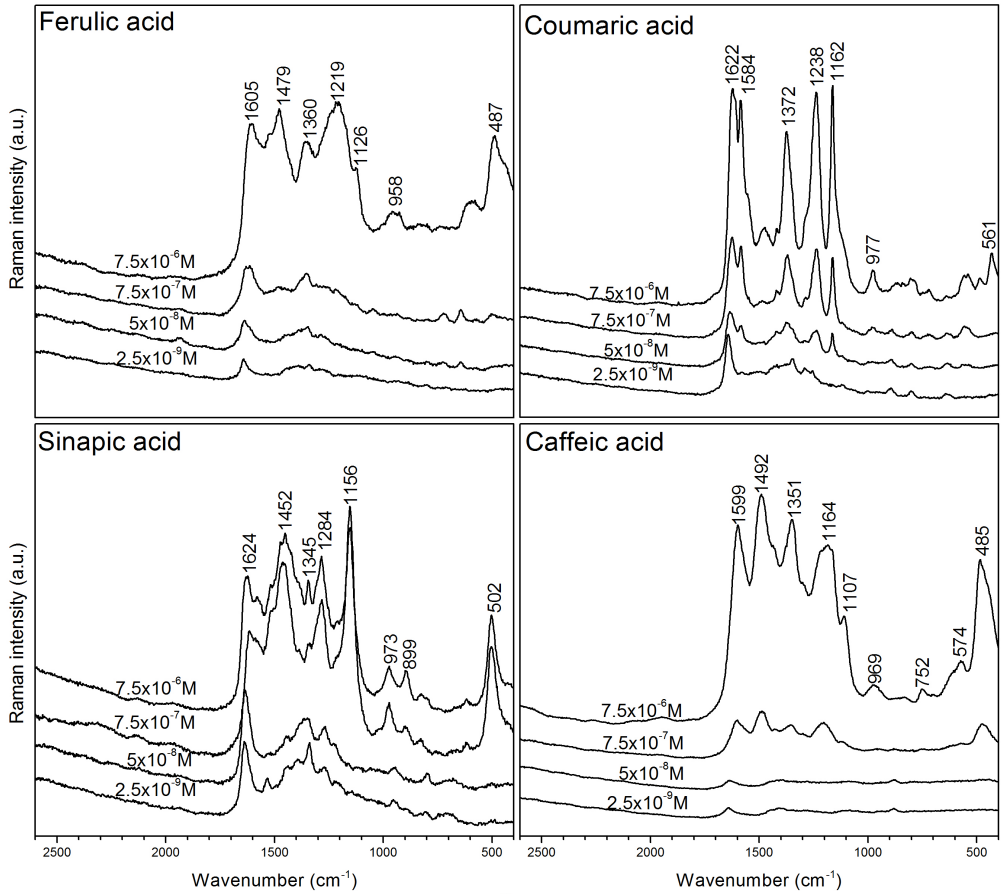

Figure 5. Concentration dependent SERS spectra of FA, 4CA, SA and CA adsorbed onto Ag colloids.

Figure 5 shows the SERS detection at different levels of concentration of analytes. The SERS spectra cover a concentration range between 7.5×10^{-6} M and 2.5×10^{-9} M. As described above, the largest SERS enhancements were obtained for dilute solutions of antioxidants that were particularly adjusted to those pH values. The SERS spectra of SA, FA, 4CA and CA were recorded at 6.3, 6.5, 6.3 and 5.5 pH value, respectively. The low-concentration (2.5×10^{-9} M) spectra showed two characteristic bands observed at about 1360 and 1610 cm^{-1} and attributable to n_s(COO–) and in-plane C=C stretching mode, respectively. On the other hand, the SERS spectra of SA were recorded at pH 6.1. The SERS spectrum of SA showed an intense band located at 1452 cm^{-1} attributable to $–OCH_3$ bending. However

fluctuations of the SERS intensities at concentrations lower than 1 × 10^{-8} M were observed. Differences in the relative intensities recorded can be explained in terms of chemical adsorption of the analytes to AgNPs. Due to steric hindrance of the –OCH_3 groups, which are adjacent to –OH group, SA can be only adsorbed to AgNPs through a nonperpendicular orientation. The interaction between the ring and the silver surface is supported by the strong intensity of the C=C ring stretching mode observed at 1605 cm^{-1}, which is clearly visible at higher concentrations. However, the orientation of SA is quite difficult to determine due to the analyte keeps very low symmetry (Cs point group).

To verify the univariate linear dependence of the SERS-based method, calibration curves were obtained by plotting the SERS intensities of the SERS spectra against the antioxidant concentration in a range from 2.5 × 10^{-9} M to 7.5 × 10^{-6} M.

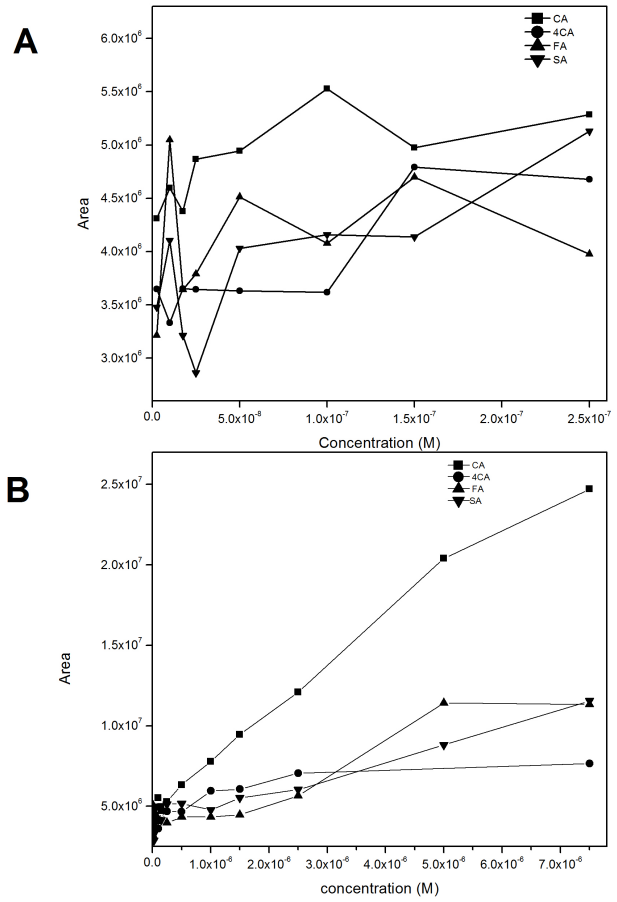

Figure 6. Calibration curves for of CA, 4CA, FA and SA from (A) 2.5x10^{-9} M to 2.5x10^{-7} M and (B) 2.5x10^{-9} M to 7.5 x10^{-6} M.

Figure 6A and 6B shows graphs of concentration versus areas, which were calculated for the spectral region between 1100 and 1700 cm^{-1}. For the purpose of semi-quantitative detection, high sensitivity was observed for CA, 4CA, FA and SA. However, there is no significant correlation at low concentrations, as shown in Fig. 6A. These results can be attributed to the chemical structure of the analytes, which should cover the surface of

nanoparticles only at a submonolayer level [77]. Particularly, despite the lack of correlation at low concentrations of SA, this is the first study in which this phenolic antioxidant was detected by a SERS method, with a limit of detection in the order of $1x10^{-9}$ M. In the case of higher concentrations of analyte (Figure 6B), a dependence of the SERS spectra on the concentration was observed, with correlation coefficients of 0.993, 0.986, 0.945, 0.989 for CA, 4CA, FA and SA, respectively.

4.Conclusions

A PCA analysis was employed as a useful tool to cluster the colloids prepared in this work on the basis of their concentration aggregation and nanoparticle size, in order to gain insights into the sensitive and quantitative SERS determination. Tests with diverse colloids show that not any colloidal solution can generate sensitive SERS measurements; some of them offered poor levels of enhancement or produced no signal at all, even when working with a test molecule like the amino acid glycine. Selected conditions for colloidal synthesis such as high concentration and long aging times (Table 1) were used for the development of a highly sensitive SERS-based method for the detection of ferulic acid, *p*-coumaric acid, caffeic acid, and sinapic acid. The prepared SERS-active silver colloids showed an effective enhancement of Raman signals allowing the sensitive detection of the analytes at low concentrations ($2.5x10^{-9}$M). For 4CA and CA, these low detections were reached for the first time. In addition, the SERS analysis of SA using silver colloids is also detected for the first time. Moreover, it was observed that the enhancement of SERS signals was highly dependent on pH, and subsequently on the chemical structure of each analyte at a specific pH value and its interaction with the surface of the metallic nanoparticles

References

[1] T. P. Kondratyuk and J. M. Pezzuto, “Natural Product Polyphenols of Relevance to Human Health,” Arch. Physiol. Biochem., vol. 42, no. s1, pp. 46–63, 2004.

[2] M. Srinivasan, A. R. Sudheer, and V. P. Menon, “Ferulic Acid: therapeutic potential through its antioxidant property.,” J. Clin. Biochem. Nutr., vol. 40, no. 2, pp. 92–100, 2007.

[3] C. Luceri, L. Giannini, M. Lodovici, E. Antonucci, R. Abbate, E. Masini, and P. Dolara, “p-Coumaric acid, a common dietary phenol, inhibits platelet activity in vitro and in vivo.,” Br. J. Nutr., vol. 97, no. 3, pp. 458–63, 2007.

[4] M. Touaibia, J. Jean-François, and J. Doiron, “Caffeic Acid, a versatile pharmacophore: an overview.,” Mini Rev. Med. Chem., vol. 11, no. 8, pp. 695–713, 2011.

[5] N. Nićiforović and H. Abramovič, “Sinapic acid and its derivatives: Natural sources and bioactivity,” Compr. Rev. Food Sci. Food Saf., vol. 13, no. 1, pp. 34–51, 2014.

[6] A. H. Laghari, S. Memon, A. Nelofar, K. M. Khan, and A. Yasmin, “Determination of free phenolic acids and antioxidant activity of methanolic extracts obtained from fruits and leaves of Chenopodium album,” Food Chem., vol. 126, no. 4, pp. 1850–1855, 2011.

[7] A. Ota, H. Abramovič, V. Abram, and N. Poklar Ulrih, “Interactions of p-coumaric, caffeic and ferulic acids and their styrenes with model lipid membranes,” Food Chem., vol. 125, no. 4, pp. 1256–1261, 2011.

[8] K. Hayat, X. Zhang, H. Chen, S. Xia, C. Jia, and F. Zhong, “Liberation and separation of phenolic compounds from citrus mandarin peels by microwave heating and its effect on antioxidant activity,” Sep. Purif. Technol., vol. 73, no. 3, pp. 371–376, 2010.

[9] V. A. Papillo, P. Vitaglione, G. Graziani, V. Gokmen, and V. Fogliano, “Release of antioxidant capacity from five plant foods during a multistep enzymatic digestion protocol,” J. Agric. Food Chem., vol. 62, no. 18, pp. 4119–4126, 2014.

[10] A. de Camargo, M. A. B. Regitano-d’Arce, C. Telles Biasoto, and F. Shahidi, “Enzyme-assisted extraction of phenolics from winemaking by-products: Antioxidant potential and inhibition of alpha-glucosidase and lipase activities,” Food Chem., vol. 212, pp. 395–402, 2016.

[11] V. Nour, I. Trandafir, and S. Cosmulescu, “HPLC determination of phenolic acids, flavonoids and juglone in walnut leaves,” J. Chromatogr. Sci., vol. 51, no. 9, pp. 883–890, 2013.

[12] A. Zhang, L. Wan, C. Wu, Y. Fang, G. Han, H. Li, Z. Zhang, and H. Wang, “Simultaneous determination of 14 phenolic compounds in grape canes by HPLC-DAD-UV using wavelength switching detection,” Molecules, vol. 18, no. 11, pp. 14241–14257, 2013.

[13] J. Yang, P. D. Bowman, S. M. Kerwin, and S. Stavchansky, “Development and validation of an LCMS method to determine the pharmacokinetic profiles of caffeic acid phenethyl amide and caffeic acid phenethyl ester in male Sprague-Dawley rats,” Biomed. Chromatogr., vol. 28, no. 2, pp. 241–246, 2014.

[14] B. Bayram, B. Ozcelik, G. Schultheiss, J. Frank, and G. Rimbach, “A validated method for the determination of selected phenolics in olive oil using high-performance liquid chromatography with coulometric electrochemical detection and a fused-core column,” Food Chem., vol. 138, no. 2–3, pp. 1663–1669, 2013.

[15] E. Porgali and E. Büyüktuncel, “Determination of phenolic composition and antioxidant capacity of native red wines by high performance liquid chromatography and spectrophotometric methods,” Food Res. Int., vol. 45, no. 1, pp. 145–154, 2012.

[16] A. M. Tarola, F. Van de Velde, L. Salvagni, and R. Preti, “Determination of Phenolic Compounds in Strawberries (Fragaria ananassa Duch) by High Performance Liquid Chromatography with Diode Array Detection,” Food Anal. Methods, vol. 6, no. 1, pp. 227–237, 2013.
[17] P. Bourget, A. Amin, F. Vidal, C. Merlette, and F. Lagarce, “Comparison of Raman spectroscopy vs. high performance liquid chromatography for quality control of complex therapeutic objects: Model of elastomeric portable pumps filled with a fluorouracil solution,” J. Pharm. Biomed. Anal., vol. 91, pp. 176–184, 2014.
[18] A. Jenkins, R. Larsen, and T. Williams, “Characterization of amino acids using Raman spectroscopy.,” Spectrochim. Acta. A. Mol. Biomol. Spectrosc., vol. 61, no. 7, pp. 1585–94, May 2005.
[19] S.-M. Choi and C.-Y. Ma, “Structural characterization of globulin from common buckwheat (Fagopyrum esculentum Moench) using circular dichroism and Raman spectroscopy,” Food Chem., vol. 102, no. 1, pp. 150–160, Jan. 2007.
[20] K. Virkler and I. Lednev, “Raman spectroscopy offers great potential for the nondestructive confirmatory identification of body fluids.,” Forensic Sci. Int., vol. 181, no. 1–3, pp. e1–e5, Oct. 2008.
[21] B. Pettinger, “Adsorption of Molecules at Metal Electrodes,” in Adsorption of Molecules at Metal Electrodes, J. Lipowski and P. N. Ross, Eds. 1992, p. 285.
[22] D. L. Jeanmaire and R. P. Van Duyne, “Surface raman spectroelectrochemistry,” Journal of Electroanalytical Chemistry and Interfacial Electrochemistry, vol. 84, no. 1. pp. 1–20, 1977.
[23] M. G. Albrecht and J. A. Creighton, “Anomalously Intense Raman Spectra of Pyridine at a Silver Electrode,” J. Am. Chem. Soc., vol. 99, pp. 5215–5217, 1977.
[24] M. Moskovits, “Surface-enhanced spectroscopy,” Rev. Mod. Phys., vol. 57, no. 3, pp. 783–826, 1985.
[25] L. Jensen, C. M. Aikens, and G. C. Schatz, “Electronic structure methods for studying surface-enhanced Raman scattering.,” Chem. Soc. Rev., vol. 37, no. 5, pp. 1061–1073, 2008.
[26] J. R. Lombardi and R. L. Birke, “A Unified Approach to Surface-Enhanced Raman Spectroscopy,” J. Phys. Chem. C, vol. 112, no. 14, pp. 5605–5617, 2008.
[27] J. R. Lombardi and R. L. Birke, “A unified view of surface-enhanced Raman scattering.,” Acc. Chem. Res., vol. 42, no. 6, pp. 734–742, 2009.
[28] C. L. Haynes, C. R. Yonzon, X. Zhang, and R. P. Van Duyne, “Surface-enhanced Raman sensors: early history and the development of sensors for quantitative biowarfare agent and glucose detection,” J. Raman Spectrosc., vol. 36, no. 6–7, pp. 471–484, Jun. 2005.
[29] M. Moskovits, “Persistent misconceptions regarding SERS.,” Phys. Chem. Chem. Phys., vol. 15, no. 15, pp. 5301–11, 2013.
[30] A. Kandakkathara, I. Utkin, and R. Fedosejevs, “Surface-enhanced raman scattering (SERS) detection of low concentrations of tryptophan amino acid in silver colloid.,” Appl. Spectrosc., vol. 65, no. 5, pp. 507–13, May 2011.
[31] X. Dou, Y. M. Jung, H. Yamamoto, S. Doi, and Y. Ozaki, “Near-Infrared Excited Surface-Enhanced Raman Scattering of Biological Molecules on Gold Colloid I: Effects of pH of the Solutions of Amino Acids and of Their Polymerization,” Appl. Spectrosc., vol. 53, no. 2, pp. 133–138, 1999.
[32] F. Wei, D. Zhang, N. J. Halas, and J. D. Hartgerink, “Aromatic amino acids providing characteristic motifs in the Raman and SERS spectroscopy of peptides.,” J. Phys. Chem. B, vol. 112, no. 30, pp. 9158–64, Jul. 2008.
[33] E. Podstawka, Y. Ozaki, and L. M. Proniewicz, “Adsorption of S-S containing proteins on a colloidal silver surface studied by surface-enhanced Raman spectroscopy.,” Appl. Spectrosc., vol. 58, no. 10, pp. 1147–56, Oct. 2004.
[34] O. Dong and D. C. C. Lam, “Silver nanoparticles as surface-enhanced Raman substrate for quantitative identification of label-free proteins,” Mater. Chem. Phys., vol. 126, no. 1–2, pp. 91–96, Mar. 2011.

[35] X. X. Han, H. Y. Jia, Y. F. Wang, Z. C. Lu, C. X. Wang, W. Q. Xu, B. Zhao, and Y. Ozaki, “Analytical technique for label-free multi-protein detection based on Western blot and surface-enhanced Raman scattering.,” Anal. Chem., vol. 80, no. 8, pp. 2799–804, Apr. 2008.
[36] J. V. García-Ramos and S. Sánchez-Cortés, “Metal colloids employed in the SERS of biomolecules: activation when exciting in the visible and near-infrared regions,” J. Mol. Struct., vol. 405, no. 1, pp. 13–28, Mar. 1997.
[37] Y. He, S. Su, T. Xu, Y. Zhong, J. A. Zapien, J. Li, C. Fan, and S.-T. Lee, “Silicon nanowires-based highly-efficient SERS-active platform for ultrasensitive DNA detection,” Nano Today, vol. 6, no. 2, pp. 122–130, Apr. 2011.
[38] T. Smith-Palmer, C. Douglas, and P. Fredericks, “Rationalizing the SER spectra of bacteria,” Vib. Spectrosc., vol. 53, no. 1, pp. 103–106, May 2010.
[39] N. E. Marotta and L. A. Bottomley, “Surface-enhanced raman scattering of bacterial cell culture growth media,” Appl. Spectrosc., vol. 64, no. 6, pp. 601–606, 2010.
[40] G. V Pavan Kumar, B. a Ashok Reddy, M. Arif, T. K. Kundu, and C. Narayana, “Surface-enhanced Raman scattering studies of human transcriptional coactivator p300.,” J. Phys. Chem. B, vol. 110, no. 33, pp. 16787–92, Aug. 2006.
[41] E. Cepeda-Perez, I. Aguilar-Hernandez, T. Lopez-Luke, V. Piazza, R. Carriles, N. Ornelas-Soto, and E. de la Rosa, “Interaction of TGA@CdTe Quantum Dots with an Extracellular Matrix of Haematococcus pluvialis Microalgae Detected Using Surface-Enhanced Raman Spectroscopy (SERS),” Appl. Spectrosc., vol. 70, no. 9, pp. 1571–1572, 2016.
[42] R. E. Clavijo, D. J. Ross, and R. F. Aroca, “Surface enhanced raman scattering of trans-p-coumaric and syringic acids,” J. Raman Spectrosc., vol. 40, no. 12, pp. 1984–1988, 2009.
[43] S. Sánchez-Cortés and J. V. García-Ramos, “FT surface-enhanced Raman evidence of the oxidative condensation reactions of caffeic acid in solution and on silver surface,” Appl. Spectrosc., vol. 54, no. 2, pp. 230–238, 2000.
[44] S. Sánchez-Cortés and J. V. García-Ramos, “Photoinduced coupling and adsorption of caffeic acid on silver surface studied by surface-enhanced Raman spectroscopy,” Spectrochim. Acta - Part A Mol. Biomol. Spectrosc., vol. 55, no. 14, pp. 2935–2941, 1999.
[45] S. Sánchez-Cortés and J. García-Ramos, “Adsorption and Chemical Modification of Phenols on a Silver Surface.,” J. Colloid Interface Sci., vol. 231, no. 1, pp. 98–106, 2000.
[46] M. Sackmann and a. Materny, “Surface enhanced Raman scattering (SERS)—a quantitative analytical tool?,” J. Raman Spectrosc., vol. 37, no. 1–3, pp. 305–310, 2006.
[47] D. Zhang, R. Haputhanthri, S. M. Ansar, K. Vangala, H. I. De Silva, A. Sygula, S. Saebo, and C. U. Pittman, “Ultrasensitive detection of malondialdehyde with surface-enhanced Raman spectroscopy,” Anal. Bioanal. Chem., vol. 398, no. 7–8, pp. 3193–3201, 2010.
[48] X. X. Han, G. G. Huang, B. Zhao, and Y. Ozaki, “Label-free highly sensitive detection of proteins in aqueous solutions using surface-enhanced Raman scattering.,” Anal. Chem., vol. 81, no. 9, pp. 3329–33, May 2009.
[49] J. Moger, P. Gribbon, a Sewing, and C. P. Winlove, “Feasibility study using surface-enhanced Raman spectroscopy for the quantitative detection of tyrosine and serine phosphorylation.,” Biochim. Biophys. Acta, vol. 1770, no. 6, pp. 912–8, Jun. 2007.
[50] J. Gao, H. Gu, F. Liu, X. Dong, M. Xie, and Y. Hu, “Effect of concentration and pH on the surface-enhanced Raman scattering of captopril on nano-colloidal silver surface,” J. Mol. Struct., vol. 998, no. 1–3, pp. 171–178, Jul. 2011.

[51] Y. Rao, Q. Chen, J. Dong, and W. Qian, “Growth-sensitive 3D ordered gold nanoshells precursor composite arrays as SERS nanoprobes for assessing hydrogen peroxide scavenging activity.,” Analyst, vol. 136, pp. 769–774, 2011.
[52] M. Dendisova-Vyskovska, G. Broncova, M. Clupek, V. Prokopec, and P. Matejka, “In situ SERS spectroelectrochemical analysis of antioxidants deposited on copper substrates: What is the effect of applied potential on sorption behavior?,” Spectrochim. Acta - Part A Mol. Biomol. Spectrosc., vol. 99, pp. 196–204, 2012.
[53] J. A. Creighton, C. G. Blatchford, and M. G. Albrecht, “Plasma Resonance Enhancement of Raman Scattering by Pyridine Adsorbed on Silver or Gold Sol Particles of Size,” J. Chem. Soc., Faraday Trans. 2, vol. 75, pp. 790–798, 1979.
[54] X. Chen, H. Gu, G. Shen, X. Dong, and J. Kang, “Spectroscopic study of surface enhanced Raman scattering of caffeine on borohydride-reduced silver colloids,” J. Mol. Struct., vol. 975, no. 1–3, pp. 63–68, 2010.
[55] W. Meng, F. Hu, X. Jiang, and L. Lu, “Preparation of silver colloids with improved uniformity and stable surface-enhanced Raman scattering,” Nanoscale Res. Lett., vol. 10, no. 1, pp. 1–8, 2015.
[56] G. Das, F. Gentile, M. L. Coluccio, A. M. Perri, A. Nicastri, F. Mecarini, G. Cojoc, P. Candeloro, C. Liberale, F. De Angelis, and E. Di Fabrizio, “Principal component analysis based methodology to distinguish protein SERS spectra,” in Journal of Molecular Structure, 2011, vol. 993, no. 1–3, pp. 500–505.
[57] S. V. Sokolov, K. Tschulik, C. Batchelor-McAuley, K. Jurkschat, and R. G. Compton, “Reversible or Not? Distinguishing Agglomeration and Aggregation at the Nanoscale,” Anal. Chem., vol. 87, no. 19, pp. 10033–10039, 2015.
[58] A. Barbara, F. Dubois, A. Ibanez, L. M. Eng, and P. Quémerais, “SERS correlation spectroscopy of silver aggregates in colloidal suspension: Quantitative sizing down to a single nanoparticle,” J. Phys. Chem. C, vol. 118, no. 31, pp. 17922–17931, Jul. 2014.
[59] S. Agnihotri, S. Mukherji, and S. Mukherji, “Size-controlled silver nanoparticles synthesized over the range 5–100 nm using the same protocol and their antibacterial efficacy,” RSC Adv., vol. 4, no. 8, pp. 3974–3983, 2014.
[60] D. D. Evanoff and G. Chumanov, “Synthesis and optical properties of silver nanoparticles and arrays,” ChemPhysChem, vol. 6, no. 7, pp. 1221–1231, 2005.
[61] D. Paramelle, A. Sadovoy, S. Gorelik, P. Free, J. Hobley, and D. G. Fernig, “A rapid method to estimate the concentration of citrate capped silver nanoparticles from UV-visible light spectra.,” Analyst, vol. 139, no. 19, pp. 4855–61, 2014.
[62] K. B. Mogensen and K. Kneipp, “Size-dependent shifts of plasmon resonance in silver nanoparticle films using controlled dissolution: Monitoring the onset of surface screening effects,” J. Phys. Chem. C, vol. 118, no. 48, pp. 28075–28083, 2014.
[63] Y. Xiaojuan, G. Huaimin, and W. Jiwei, “Surface-enhanced Raman spectrum of Gly-Gly adsorbed on the silver colloidal surface,” J. Mol. Struct., vol. 977, no. 1–3, pp. 56–61, Aug. 2010.
[64] J. S. Suh and M. Moskovits, “Surface-Enhanced Raman Spectroscopy of Amino Acids and Nucleotide Bases Adsorbed on Silver,” J. Am. Chem. Soc., vol. 108, no. 21, pp. 44711–4718, 1986.
[65] A. Sabur, M. Havel, and Y. Gogotsi, “SERS intensity optimization by controlling the size and shape of faceted gold nanoparticles,” J. Raman Spectrosc., vol. 39, pp. 61–67, 2008.
[66] Shiohara Amane, Y. Wang, and L. M. Liz-Marzán, “Recent approaches toward creation of hot spots for SERS detection,” J. Photochem. Photobiol. C Photochem. Rev., vol. 21, pp. 2–25, 2014.
[67] C. P. Shaw, M. Fan, C. Lane, G. Barry, A. I. Jirasek, and A. G. Brolo, “Statistical Correlation Between SERS Intensity and Nanoparticle Cluster Size,” J. Phys. Chem. C, vol. 117, no. 32, pp. 16596–16605, Aug. 2013.

[68] V. R. R. Cunha, V. R. L. Constantino, and R. A. Ando, “Raman spectroscopy and DFT calculations of para-coumaric acid and its deprotonated species,” Vib. Spectrosc., vol. 58, pp. 139–145, 2012.
[69] J. L. Castro, M. R. López Ramírez, I. López Tocón, and J. C. Otero, “Vibrational study of the metal-adsorbate interaction of phenylacetic acid and α-phenylglycine on silver surfaces,” J. Colloid Interface Sci., vol. 263, no. 2, pp. 357–363, 2003.
[70] X. Dou, Y. M. Jung, Z. Q. Cao, and Y. Ozaki, “Surface-enhanced Raman scattering of biological molecules on metal colloid II: Effects of aggregation of gold colloid and comparison of effects of pH of glycine solutions between gold and silver colloids,” Appl. Spectrosc., vol. 53, no. 11, pp. 1440–1447, 1999.
[71] E. C. Le Ru, E. J. Blackie, M. Meyer, and P. G. Etchegoin, “Surface Enhanced Raman Scattering Enhancement Factors: A Comprehensive Study,” J. Phys. Chem. C, vol. 111, no. 37, pp. 13794–13803, 2007.
[72] U. K. Sarkar, “A pH-dependent SERS study of thiophene-2-carboxylic acid adsorbed on Ag-sols,” Chem. Phys. Lett., vol. 374, no. 3–4, pp. 341–347, 2003.
[73] S. P. Ozkorucuklu, J. Beltrán, G. Fonrodona, D. Barrón, G. Alsancak, and J. Barbosa, “Determination of dissociation constants of some hydroxylated benzoic and cinnamic acids in water from mobility and spectroscopic data obtained by CE-DAD,” J. Chem. Eng. Data, vol. 54, no. 3, pp. 807–811, 2009.
[74] I. Pavel, a Szeghalmi, D. Moigno, S. Cîntă, and W. Kiefer, “Theoretical and pH dependent surface enhanced Raman spectroscopy study on caffeine.,” Biopolymers, vol. 72, no. 1, pp. 25–37, 2003.
[75] C.-B. Wang, G. Deo, and I. E. Wachs, “Interaction of Polycrystalline Silver with Oxygen, Water, Carbon Dioxide, Ethylene and\rMethanol: In Situ Raman and Catalytic Studies,” J. Phys. Chem. B, vol. 103, no. 27, pp. 5645–5656, 1999.
[76] G. I. N. Waterhouse, G. A. Bowmaker, and J. B. Metson, “Oxygen chemisorption on an electrolytic silver catalyst: A combined TPD and Raman spectroscopic study,” Appl. Surf. Sci., vol. 214, no. 1–4, pp. 36–51, 2003.
[77] L. Wu, Z. Wang, S. Zong, Z. Huang, P. Zhang, and Y. Cui, “A SERS-based immunoassay with highly increased sensitivity using gold/silver core-shell nanorods,” Biosens. Bioelectron., vol. 38, no. 1, pp. 94–99, 2012.

CHAPTER 3
Single molecule detection

Carbon-Based Electrospun Nanofibers Decorated With Gold Nanoparticles as Substrate for SERS

Chapter 3

Carbon-Based Electrospun Nanofibers Decorated With Gold Nanoparticles as Substrate for SERS

1. Introduction

There has been an increasing interest in Au and Ag plasmonic substrates with well-controlled architecture for providing Surface Enhanced Raman Spectroscopy (SERS) for improved sensitivity and high-speed monitoring at low concentrations of target analytes [1]. 3D substrates composed of nanofibers provide higher surface area for nanoparticle attachment and generation of SERS hot spots [2]. Previous studies of electrospun nanofibers based on embedding of metallic nanostructures directly inside of fibers in the polymer matrix [3-5] or the direct growth on the fibers [2]. However the main drawback of these approaches is the limited control over the final shape of the metallic nanostructure. Furthermore, these approaches are not compatible with all nanoparticles, such as gold, which have very lower melting temperature than carbon pyrolysis temperatures. Gold nanoparticles (AuNPs) have low susceptibility to oxidation and are known to be highly stable. In addition, gold nanostructures are biocompatible and adequate materials for detection of biological analytes and environmental samples [6, 7]. A main drawback of polymeric nanofibers is that when in contact with water, the fibers swell and consequently lose their advantageous morphological characteristics such as porosity and high surface area. In some cases, fibers are completely dissolved [8, 9]. Carbonized polymer fibers are highly water-stable substrates and maintain the desirable properties of porosity, hierarchical structure and high superficial area provided. Furthermore, enrichment of the carbon surface by means of oxidative processes can offer a high degree of control over the post-synthesis decoration with nanostructures.

In this work a novel methodology to prepare SERS-active substrates composed of carbon electrospun nanofibers decorated with Au nanoparticles was developed. Nanofibers employed in this study were modified by several steps which include: an oxidation process for producing oxidized functional groups into the surface, a covalent functionalization with alcoxi-amine-silanols through one-step methodology with 3-aminopropyl-trimethoxysilane (APTMS), and the deposition of Au nanoparticles that were attached throughout a metal-NH linkage.

2. Experimental details

2.1. Gold nanoparticle synthesis and characterization

Gold nanoparticles (AuNPs) were synthesized by the method of chloroauric acid ($HAuCl_4 \cdot 3H_2O$; Sigma–Aldrich, USA, 99%) reduction with trisodium citrate dihydrate (Sigma–Aldrich, USA, 99%).

AuNPs were characterized by UV-Vis spectrophotometry and scanning electron microscopy. UV-Vis spectra were recorded in the range of 200-800 nm by a photodiode array (Agilent 8453 UV-Visible spectrophotometer, Agilent Technologies, Waldbronn, Germany). UV-Visible Chem-Station was used for data acquisition. The samples for Scanning Electron Microscope analysis (JEOL, JSM-7800F Field Emission Scanning Electron Microscope, Japan) were prepared on a carbon-coated copper grid cleaned previously with chloroform by dropping a very small amount of the sample onto the grid. The sample was dispersed and extra solution was removed by using a blotting paper and then the film on the grid was allowed to dry for 60 minutes. The average particle diameter of AuNPs on CNFs was calculated from the following formula: $\langle d \rangle_{AuNP} = \Sigma n_i d_i / \Sigma n_i$, where n_i is the number of particles of diameter d_i. The histograms of the AuNPs sizes were established from the measurements of 500 to 1000 particles by using ImageJ 1.43u.

2.2. Carbon nanofibers fabrication and characterization

CNFs were fabricated by a far-field electrospinning technique and carbonized in a pyrolytic oven (UC, Irvine). Briefly, a 10% w/v solution of commercial polyacrylonitrile (PAN) and *N,N*- dimethylformamide (DMF) was prepared and vigorously stirred at room temperature with sodium phosphate until the solution reached a conductivity of 0.71 mS/cm. Then, the solution was loaded for electrospinning process, in which a high voltage (typically 10 kV) is used to create an electrically charged jet of the polymeric solution. A distance of 10 cm between the tip of the needle and the collector was fixed and thus the positive voltage was applied to the needle. A flow rate of 0.1 ml/hr was controlled with a PHD 70-2001 syringe pump (Harvard Apparatus, Holliston, MA, USA). In the air gap between the nozzle and the collector, the solvent evaporates from the polymeric jet, giving rise to the formation of nanofibers; silicon wafers were used as collector substrates. Afterwards, the obtained mats were subjected to an open air thermal stabilization step at a temperature of 280°C for 1 h (6.9°C/min between 25°C and 280°C). Finally, a carbonization step at 900°C for 2 h was conducted (7.5°C/min; between 25°C and 700°C and 2.2°C/min between 700°C and 900°C) under a N_2 flow rate of 2500 SCCM (standard cubic centimeters per minute).

2.3. SERS substrate preparation

To attach oxidized functional groups into the surface of the CNFs substrates, 1 mg of $KMnO_4$ was carefully added to a solution composed of 3:1 (H_2SO_4:HNO_3) v/v and gently stirred for 5 minutes resulting in a green solution. Each CNFs mat was placed in a 50 ml beaker containing the acidic mixture and then was heated at 70°C during 6 h; during this time the color of the solution changed from green to

yellow, then to brown, and finally to purple. After, three drops of hydrogen peroxide were added in order to stop the oxidation process; the color of the solution changed from purple to transparent white. The nanofibers were washed with ultrapure water until it reached pH 7. Then, CNFs mats were allowed to stand in ultrapure water for 1 h. After that, CNFs were left in a desiccator overnight for further surface functionalization.

The functionalization reaction was performed to introduce amine functional groups instead of the oxidized groups by mixing the CNFs with 10 ml of a solution (10:0.5:0.5 v/v) consisting of methanol, NH_4OH, and 3-aminopropyl-trimethoxysilane (APTMS, Sigma-Aldrich USA, 97%) for 24 h at room temperature in darkness. The prepared nanofibers were washed with methanol, isopropanol and water three times. Afterward, nanofibers were allowed to stand in ultrapure water for 30 min.

Finally, CNFs were decorated with the synthesized AuNPs by placing them for 24 hours in a petri dish containing 9 ml of the colloidal gold solution. The mats were collected and soaked in ultrapure water in order to remove unattached nanoparticles. Finally, Au coated CNFs were placed into a desiccator until their use. Immobilization of AuNPs onto the carbon-based nanofibers was confirmed with a JEOL JSM-7800F field-emission scanning electron microscope (SEM) operating at 15 kV.

2.4. SERS measurements

Surface-enhanced Raman spectroscopy (SERS) spectra were acquired with a Renishaw inVia Raman system (Renishaw, UK) equipped with an electronically cooled (-70^{o}C) CCD camera and a research grade Leica microscope. A 50× objective was used for sample focusing and collection of Raman scattering. Raman signal was dispersed with a 2400 lines/mm diffraction grating, which resulted in spectra in the range 200 cm^{-1} to 3200 cm^{-1}. Sample excitation was provided by a 514.4 nm Argon laser (Modu-Laser, USA) with a nominal output power of 50mW; for SERS measurements the laser was attenuated to 2.5% of the total nominal output. Exposure time was set to 10s. The streamline configuration was employed using a 20×20 um^2 area irradiated. The spectral resolution was 4 cm^{-1} and the sample was exposed to air. Integration and data treatment of SERS spectra were carried out using the OriginPro 9.1 software (OriginLab Corporation, USA).

3. Results

The absorption spectrum of the synthesized AuNPs colloids is shown in Figure 1a. The surface plasmon resonance (spr) is observed by the absorption maximum (A_{spr}) at 523 nm. The plasmon bandwidth was measured as twice the distance from the low-energy side of the absorption band to the maximum position at half the maximum intensity (Assuming symmetric band). The plasmon bandwidth is calculated to be 82 nm.

A typical SEM image of the colloidal AuNPs employed in this study is shown in Figure 1b. There, the image reveals that the spherical nanoparticles are well dispersed. From the size distribution histogram, Figure 1c, the as-prepared AuNPs have an average particle size of about 17.1 ± 1.1 nm with a narrow size distribution (ImageJ software; averaged for 700 particles), which should enhance its contact with the substrate.

The Raman spectra of pristine CNFs is shown in Figure 2a, in which a total of three peaks can be observed at ~1593 cm^{-1} (width 98 cm^{-1}), ~1360 cm^{-1} (width 308 cm^{-1}), and an intense peak centered at about 2905 cm^{-1} (width 344 cm^{-1}) corresponding to D, G, and 2D vibrational modes found in polycrystalline carbon-based structures [11].

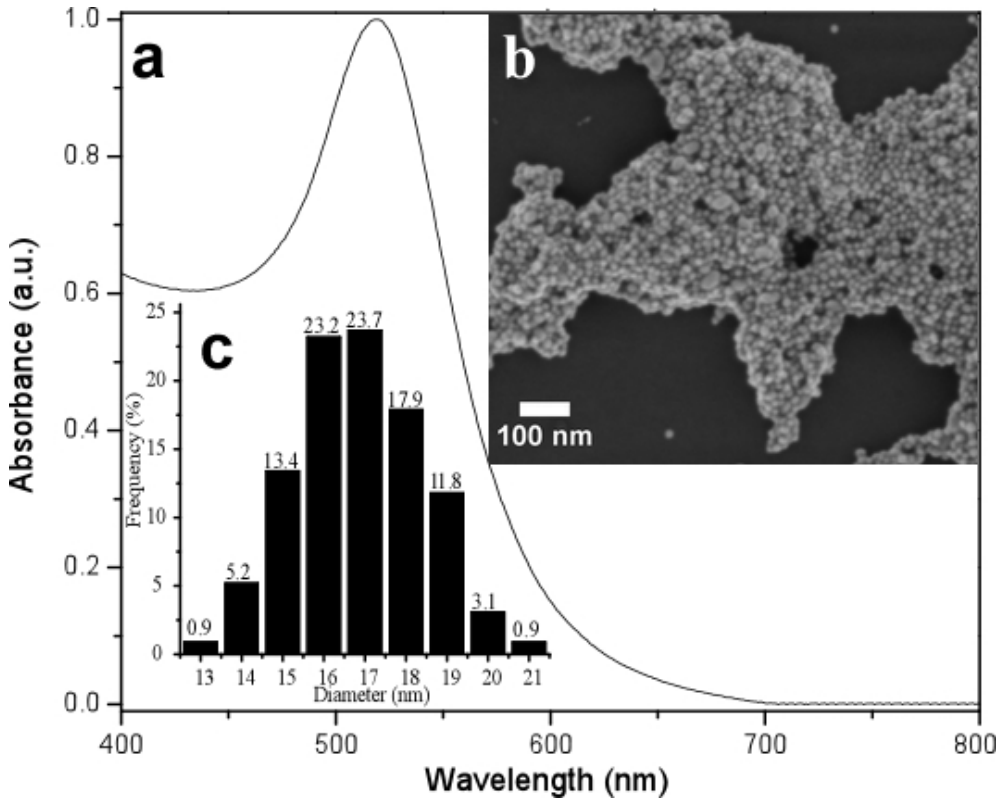

Fig. 1. a) UV–Vis absorption spectra of AuNPs in water with the surface plasmon resonance at 523 nm. b) Representative SEM image of AuNPs. c) Size distribution histogram obtained from SEM image.

Figure 2b shows the normal Raman spectrum of Rh110 adsorbed onto CNFs without surface-decorated process of AuNPs. As can be seen, normal Raman spectrum of concentrated Rh110 is largely hidden by a huge amount of fluorescence. A 1×10^{-4} M Rh110 solution was also analyzed in the same experimental conditions; the resulting Raman spectrum is shown in Fig. 3c. This spectrum resembles those most frequently obtained for pristine CNFs (see Fig. 2a). Then, the background for CNFs was subtracted and thus the Raman spectrum for 1×10^{-4} M Rh110 solution was obtained and depicted in Fig. 2d. It is believed that the signal seen in this figure (Figure 2d) is a result of equipment noise, which is obscuring the broad background signals. Therefore, a selected region of the experimental Raman spectrum is shown in the inset (Fig. 2e). A number of weaker signals emitted at 355, 423, 636, 769, 1369, 1565 and 1644 cm^{-1} can be observed when fitted using third-order Savitzky-Golay filter [12].

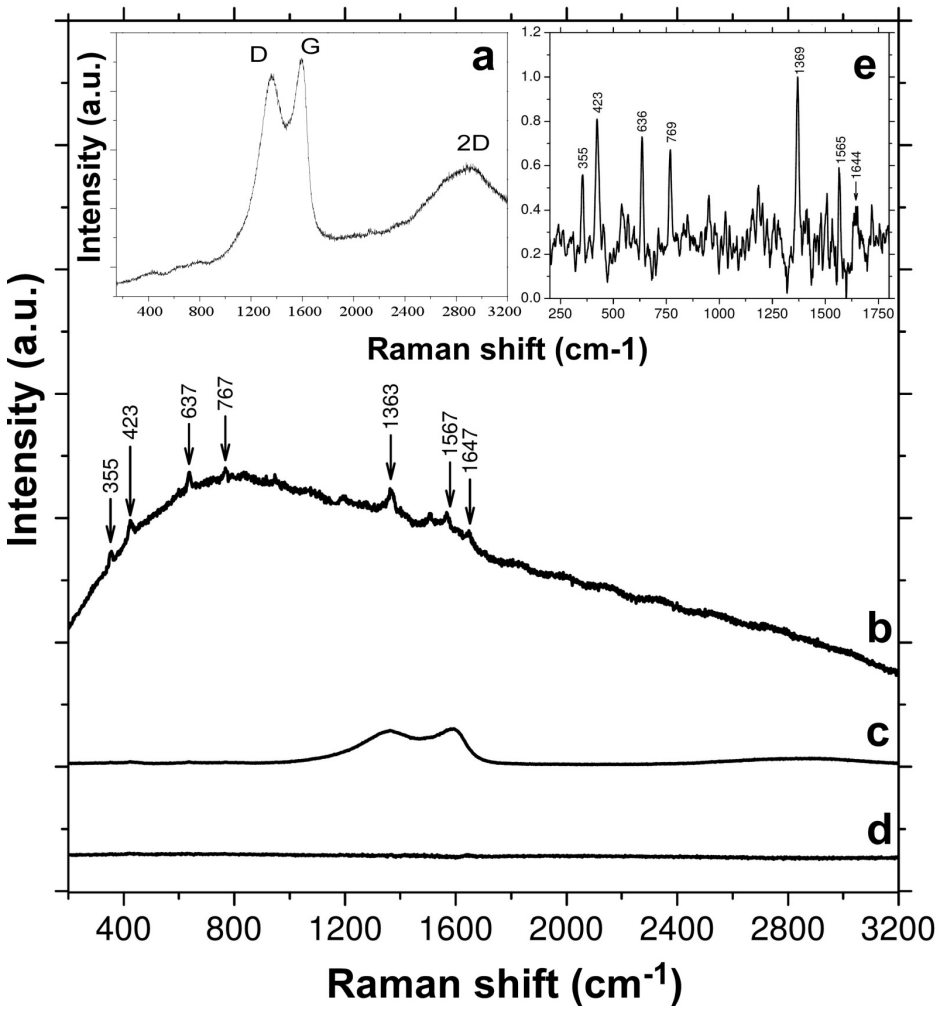

Fig. 2. a) Raman spectra for pristine CNFs. b) Concentrated Rh110. c) Rh110 1×10^{-4} M on pristine CNFs and (d) 1×10^{-4} M Rh110 on CNFs subtracting the background due to CNFs signals; selected range from d) was fitted, normalized and amplified in the inset (e).

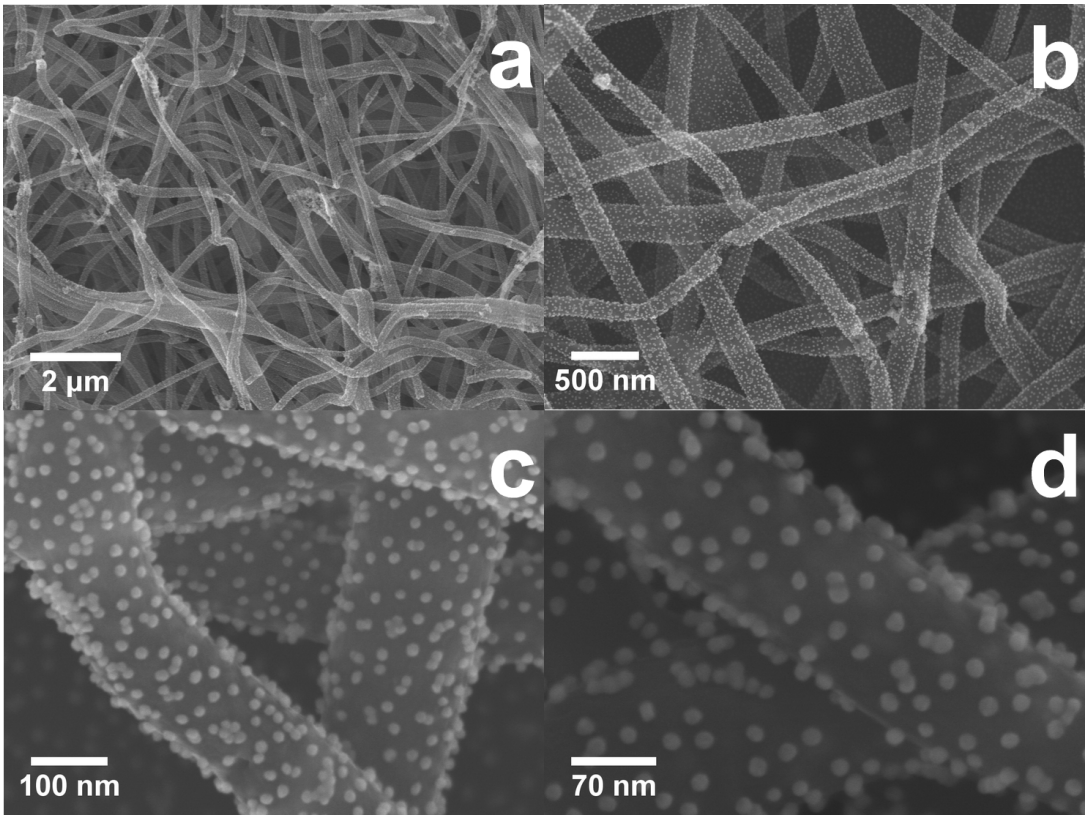

Fig. 3. SEM images of carbon nanofibers decorated with AuNPs at different magnifications. Scale bar, a) 2 µm , b) 500 nm, c) 100 nm, and d) 70 nm.

Figure 3 shows the SEM images of the CNFs decorated with AuNPs at different magnifications. From the figure, it can be seen a typical rigid, thin and well-controlled nanofibers surface structure. CNFs appear to have 1000 microns in length but on rare occasions, very small fibers was also observed whereas the diameter was in the nano-scale ranging from 90 nm to 170 nm.

The average diameter of nanofibers was measured as 131 ± 37.2 nm. Although it is not possible to distinguish the incorporated APTMS material, it can suggest that the inorganic material totally covers the surface of nanofibers. As it seen from Fig. 3b, the nanoparticles are uniformly dispersed throughout, implying an efficient performance as a SERS-active substrate. Conditions employed in this functionalization process can effectively attach nanoparticles and thus produce a dense coverage all over the surface. A close inspection form Fig. 3d reveals the spheroidal morphology of the nanoparticles arranged as small dots forming clusters of 2-5 particles. The average diameter of 673 nanoparticles on the surface of the CNFs was calculated as 17.3 ± 1.6 nm.

The SERS intensity of Rh110 as a function of its molecular concentration during the sensing was observed in detail using three concentrations of Rh110 at 1×10^{-4}, 1×10^{-5} and 1×10^{-6} M. The resulting spectra are shown in Figure 4, where it can be seen the dependence of SERS intensity on Rh110 concentration. The peaks detected at 1×10^{-5} M are similar to those observed at 1×10^{-4} M with lower intensity

of the bands, especially at the range of 500-1200 cm^{-1} at which the peaks at 703, 725, 987 cm^{-1} are at the level of the instrument noise and thus cannot be distinguished. Although the intensity decreased as the concentration of Rh110 was reduced, the SERS signals are still identifiable at 1×10^{-6} M. The capability of sensing Rh110 at such concentration is confirmed by the peaks observed at 351, 422, 634, 766, 946, 1188, 1365, 1504, 1565, and 1646 cm^{-1}. The limit of detection is obtained with these substrates is high, since rhodamine has ben detected at $10x10^{-9}$ M to $1x10^{-12}$ M [13],[14] and can be caused by the separation between nanoparticles in the substrates, since it is known that interparticle distance affects SERS enhancement [14], [15]. Although some nanoparticle clusters are observed, interparticle distance in some fibers is higher than 20 nm (Fig. 3d). Ideally, an interparticle distance of 1-2 nm allows for plasmonic coupling. Subsequent immobilization of more nanoparticles using small linker molecules[16] could help improve SERS enhancements.

Nevertheless, the observation that similar bands appear in all the three concentrations employed suggest a reproducible SERS methodology. In addition, fluorescence quenching was observed, which can be caused by the SERS and the graphitic carbon surface [17].

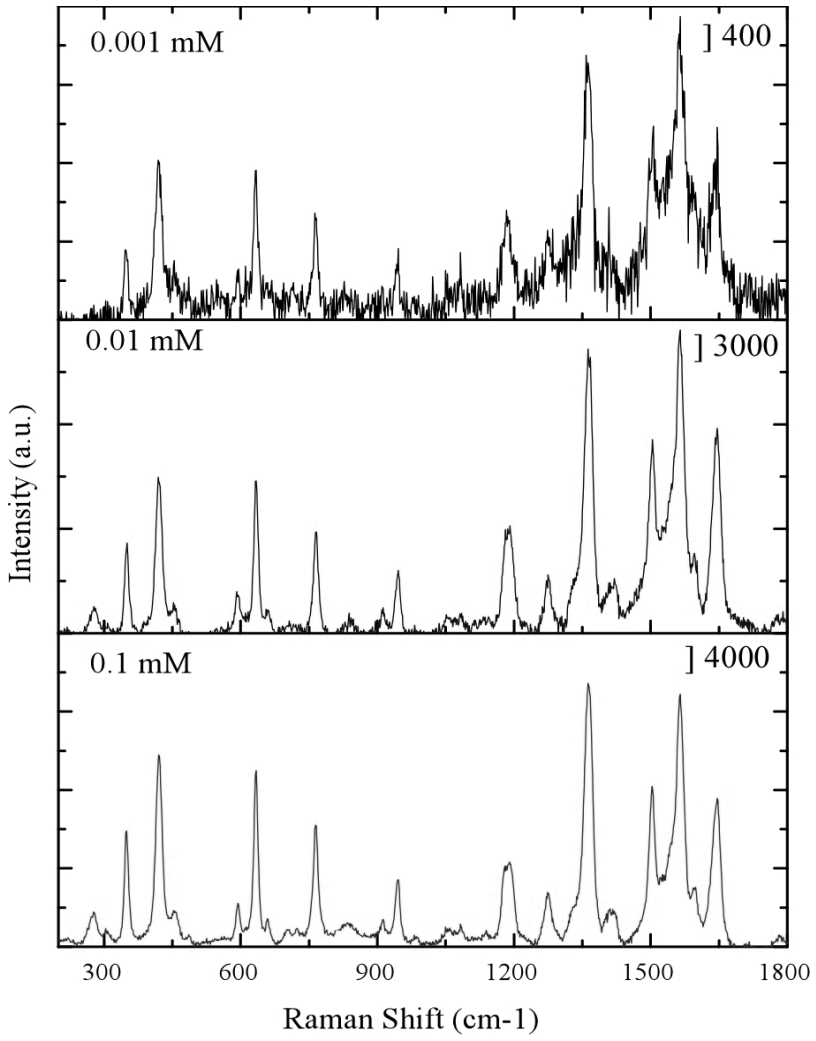

Fig. 4. SERS spectra of several rhodamine 110 concentrations: 1×10^{-4} M, 1×10^{-5} M and 1×10^{-6} M (bottom-to-top).

It is evident that the Rh110 can interact mainly with the gold particles through the NH group and thus explaining the Au–NH bonding observed at 280 cm^{-1}. This comparison suggests that adsorption of Rh110 on the gold particles through the Au–NH bonding would be present; therefore, the NH group should lie in the proximity of the gold surface.

4.Conclusions

A SERS-active substrate was obtained by using carbon nanofibers (CNFs) that were prepared by combining far-field electrospinning with a high-temperature carbonization technique, and chemically modified by oxidation, silanization and AuNPs surface-decorated processes. Substrates based on CNFs are simple to fabricate; due to the large surface area of the nanofibers, this property can be used to maximize the SERS enhancement factor and due to their chemical composition they can be modified for the immobilization of AuNPs.

AuNPs covered CNFs, including non-superficial layers, however interparticle distance was high. SERS enhancement with these substrates was tested with Rh110, reaching a 1×10^{-6} M detection limit. The detection limit is not adequate, however this sets the basis for further tailoring of the substrates.

References

[1] S. Nie, S.R. Emory, Science, 275 (1997) 1102-1106.
[2] L. Zhang, X. Gong, Y. Bao, Y. Zhao, M. Xi, C. Jiang, H. Fong, Langmuir, 28 (2012) 14433-14440.
[3] M. Cao, S. Cheng, X. Zhou, Z. Tao, J. Yao, L.-J. Fan, Journal of Polymer Research, 19 (2011).
[4] D. He, B. Hu, Q.-F. Yao, K. Wang, S.-H. Yu, ACS Nano, 3 (2009) 3993-4002.
[5] X. Li, M. Cao, H. Zhang, L. Zhou, S. Cheng, J.-L. Yao, L.-J. Fan, Journal of Colloid and Interface Science, 382 (2012) 28-35.
[6] D. Arockia Jency, M. Umadevi, G.V. Sathe, Journal of Raman Spectroscopy, 46 (2015) 377-383.
[7] L. Sun, Z. Zhang, S. Wang, J. Zhang, H. Li, L. Ren, J. Weng, Q. Zhang, Nanoscale Res Lett, 4 (2009) 216-220.
[8] Y. Liu, B. Bolger, P.A. Cahill, G.B. Mcguinness, Proceedings of the Institution of Mechanical Engineers, Part N: Journal of Nanomaterials, Nanoengineering and Nanosystems, 223 (2009) 99-111.
[9] H. Zhu, M. Du, M. Zhang, P. Wang, S. Bao, M. Zou, Y. Fu, J. Yao, Biosens Bioelectron, 54 (2014) 91-101.
[10] W. Haiss, N.T.K. Thanh, J. Aveyard, D.G. Fernig, Analytical Chemistry, 79 (2007) 4215-4221.
[11] F. Tuinstra, J.L. Koenig, The Journal of Chemical Physics, 53 (1970) 1126-1130.
[12] A. Savitzky, M.J.E. Golay, Analytical Chemistry, 36 (1964) 1627-1639.
[13]B. Pettinger, Adsorption of Molecules at Metal Electrodes, J. Lipowski and P. N. Ross, Eds. 1992, p. 285.
[14]D. L. Jeanmaire and R. P. Van Duyne, Journal of Electroanalytical Chemistry and Interfacial Electrochemistry, vol. 84, no. 1. pp. 1–20, 1977.
[15]M. G. Albrecht and J. A. Creighton, J. Am. Chem. Soc., vol. 99, pp. 5215–5217, 1977.[
[16]B. Sharma, M. Fernanda Cardinal, S. L. Kleinman, N. G. Greeneltch, R. R. Frontiera, M. G. Blaber, G. C. Schatz, and R. P. Van Duyne, MRS Bull., vol. 38, no. 8, pp. 615–624, 2013.
[17] M. R. Kagan and R. L. Mccreery, vol. 66, no. 23, pp. 4159–4165, 1994.

Chapter 4
Characterization of cellular systems

Interaction of TGA@CdTe Quantum Dots with an Extracellular Matrix of *Haematococcus pluvialis* Microalgae Detected Using Surface-Enhanced Raman Spectroscopy (SERS)

This chapter has been published as:
E. Cepeda-Pérez, I. Aguilar-Hernández, et al., Appl. Spectrosc. 70 (2016) 1561–1572.
DOI: 10.1177/0003702816654076

Chapter 4

Interaction of TGA@CdTe Quantum Dots with an Extracellular Matrix of *Haematococcus pluvialis* Microalgae Detected Using Surface-Enhanced Raman Spectroscopy (SERS)

1.Introduction

The use of engineered nanomaterials has significantly increased in recent years, for example in electronic devices [1], medical applications [2], cosmetics [3], and food products [4,5]. Nanostructured materials have emerged as a new class of environmental contaminants and this growth generates an environmental impact and increases the likelihood of an accidental interaction with organisms such as plants [6,7]. Moreover bioaccumulation is usually the means of entry of a nanomaterial into the trophic web and its toxic consequences are directly linked to higher trophic levels.

Within the different nanostructured materials quantum dots (QDs) are attractive for biotechnology applications, partially due to their optical properties. Among several other uses, QDs have been used for long-term tracking of biological processes in living systems and biological imaging with reduced photobleaching [8]. QDs are mostly synthesized in a non-polar organic solvent and therefore have a hydrophobic surface that often leads to aggregation in aqueous media, limiting their biological application [9,10]. Considering this problem, modified CdTe QDs are one of the most successful type of materials applied to biotechnology. CdTe QDs have been encapsulated or surface-modified in order to prevent aggregation and increase water-solubility and biocompatibility [10,11] . Some CdTe QD stabilizer thiols are: thioglycolic acid (TGA), 3-mercaptopropionic acid (MPA), and mercaptoethanol (ME). Thioglycolic acid and MPA stabilized CdTe QDs have been tested in the most common buffers (pH, 5–11) for the indirect immunofluorescence labeling of cells [11–13]. Nevertheless, when CdTe QDs are used to decorate living cells, their toxicity represents a problem. It is believed that the main cause of CdTe QDs cytotoxicity is the generation of reactive oxygen species (ROS) caused by the release of Cd2 ions, and the formation of TeO_2 and CdO [11,14,15] . The addition of surface coatings to the QDs, such as ZnS, polyacrylate, or dihydrolipoic acid, reduces the QD surface oxidation and the subsequent liberation of free Cd2 improving the biocompatibility [11,16]. Some studies have concluded that by conjugating CdTe QD with antioxidants toxicity can be reduced [11,15]. It has been reported that bovine serum albumin (BSA) could significantly decrease QD-induced toxicity [15].

Haematococcus pluvialis (Chlorophyceae) microalgae (HPM) is a freshwater unicellular microalgae studied for its adaptive response under conditions of environmental stress such as nutrient depletion, high salinity, high light intensities, or the presence of ROS [17].
A complete understanding of how a microalgae responds to adverse environmental conditions such as the presence of heavy metals [7] is an open issue and in the case of HPM has become critical due to the increasing interest in this organism as a biotechnological source of the ketocarotenoid astaxanthin [17–20]. *H. pluvialis* display a green color due to the high contents of photosynthetic pigments, chlorophyll, and b-carotene [18]. Typical HPMs that are less than 3 weeks old exhibit an extracellular matrix (ECM) of variable thickness that consists mostly of hydroxyproline rich glycoproteins [21,22]. At this age, HPMs show little to no presence of the chemical non-enzymatic antioxidant astaxanthin, making them more susceptible to ROS [18,23,24].
Stressed *H. pluvialis* microalgae (SHPM) undergo several morphological and biochemical changes [17,18]. When stress conditions are present, HPM grow a thick outer secondary wall, exhibit a decrease in chloroplasts and protein content, and accumulate astaxanthin, turning into red color cyst cells that have virtually lost all the ECM [21,22,25]. Internalization of QDs in plant and algal cells is not common since QDs generally are adsorbed into the cell wall [26]. In plants, the cell wall pore size is in the range of 5–20 nm [27]. It has been stated that in certain algae species QDs can damage the wall and membrane and are known to generate ROS within the microalgae, thus inducing the activation of enzymatic antioxidant systems [23,27]. For instance, it has been reported that higher oxidative stress is observed when microalgae are incubated with QDs [24].
This oxidative stress and the interaction of HPMs and QDs may lead to cellular content changes in the HPM that can be studied by Raman spectroscopy [28,29]. The spectroscopic observation of the interaction of nanoparticles, such as QDs, with cells using gold nanoaggregates was proposed by Kneipp et al.[30] and is of particular interest for bio- accumulation studies and drug delivery.

The early bioaccumulation of TGA capped CdTe QDs on living microalgae cells is largely unknown. With the aim of contributing on this topic we studied the early interaction of HPM with TGA capped CdTe QDs using surface enhanced Raman spectroscopy (SERS) as a tool for detecting possible molecular structural changes due to an interaction of the QDs with the ECM, using SHPM as control sample since they do not present an ECM. Surface enhanced Raman spectroscopy is obtained through naked anisotropic gold nanoparticles (AuNPs), which did not alter the previously reported characteristic Raman signal of the algae. Spectral differences between HPM/AuNPs and HPM-QDs/AuNPs manifest as changes in the intensity of characteristic shifts associated to chlorophyll and the appearance of a band at 940 cm^{-1}. By confocal microscopy, it is confirmed that CdTe@TGA QDs are located in the ECM of HPM. Stressed *H. pluvialis* lack such ECM and a very small amount of CdTe@TGA QDs is observed on the outside of the secondary cell wall; given our experimental results it is proposed that the secondary wall of SHPM prevents or reduces the interaction of QDs with the cells. The presence of Au, Cd, and Te on the surface of algae samples is confirmed by energy dispersive

spectroscopy (EDS). The successful detection of changes in the Raman spectra of unicellular algae due to an early interaction with TGA–CdTe QDs has not been reported before and may lead to a deeper understanding of the response mechanisms of plant cells in the presence of QDs.

2. Experimental details

2.1.Materials

All chemicals were analytical grade. Cadmium perchlorate hydrate ($Cd(ClO_4)_26H_2O$), thioglycolic acid (TGA), gold(III) chloride hydrate ($HAuCl_4$), and sodium hydroxide (NaOH) were purchased from Sigma-Aldrich. Aluminum telluride (Al_2Te_3) was acquired from Advanced Chemicals. Sulfuric acid (H_2SO_4) and acetone were purchased from Karal. Sodium borohydride ($NaBH_4$) was purchased from Fluka. Deionized water was purchased from Quimicurt. Fluoro Care Anti-Fade Mountant was purchased from Biocare Medical. Standard Wright's Cryptophyte was prepared according to established protocols.

2.2.Preparation of TGA-Capped CdTe Quantum Dots

The synthesis of TGA-capped CdTe QDs is based on the method reported by Gaponik et al.[31] Added to 125 mL of distilled water and stirred for 5 min was 2.35 mmol of $Cd(ClO_4)_26H_2O$ and 5.7 mmol of TGA. The pH was adjusted to 11.4 by addition of 1 M solution of NaOH. The solution was heated to 100°C for 20 min under an N_2 atmosphere using a condenser with recirculate water (12°C). H_2Te gas generated by the reaction of 0.2 g (0.416 mmol) of Al_2Te_3 and ~20 mL of 0.5 M H_2SO_4 under N_2 atmosphere,was passed through the Cd-TGA solution flask and stirring for 20 min, resulting in TGA-capped CdTe QDs. The reaction time for the growth of QDs was 4 h.

2.3.Preparation of Gold Anisotropic Nanoparticles

Preparation of AuNPs was based on the method reported by Martin et al.[32]. A total of 0.1 M of $NaBH_4$ were added, under stirring, to a solution of 1 M of $HAuCl_4$ and 90 mL of distilled water previously cooled to 5°C. The resulting nanoparticles were aged at room temperature for 4 days to allow aggregation [33].

2.4. Cell culture

Haematococcus pluvialis was obtained from the Culture Collection of Algae at the University of Texas at Austin (UTEX). *H. pluvialis* was cultured at room temperature in Erlenmeyer flasks and kept in orbital shakers under illumination with white fluorescent lights (125 μmol photons m^{-2} s^{-1}) and a 12:12 light–dark photoperiod. The culture media consisted of standard Wright's Cryptophyte (WC). In order to induce stress in the HPM, a nitrogen-limited culture was prepared; this together with suitable culturing periods lead to the development of red cysts [34].The nitrogen limited culture had five times less nitrogen than the standard WC media. Algae concentrations in cell culture were 145 500 and 125 000 cells/mL for HPM and SHPM, respectively.

2.5. Incubation of microalgae with CdTe@TGA QDs and AuNPs.

The procedure was conducted at room temperature. The microalgae were washed with deionized water in order to remove traces of culture media. A volume of 200 mL of cells suspended in WC were dispersed in 1 mL of deionized water, stirred for a few seconds and centrifuged at 3600 rpm for 3 min. The supernatant was decanted and cells were resuspended in 1 μL of deionized water. At this point the

sample was divided into two Eppendorff tubes, each one containing 500 µL of algae dispersed in deionized water; an additional 500 µL of deionized water were added to each tube. A sample of algae suspended in deionized water was used as a control sample. The cell-QDs sample was obtained by the addition of 100 µL of QDs to cells, followed by a 5 min incubation period; the excess of CdTe@TGA QDs was removed by centrifugation. The samples were suspended in 0.5 mL of deionized water and 50 µL of the suspension were taken and placed on microscope slides for confocal microscopy.
For Raman spectroscopy measurements, 200 µL of AuNPs were added. After an incubation time of 30 min the samples were centrifuged and 50 µL are taken and placed on a silicon wafer [35,36]. For EDS measurements, 25 µL of the algae suspension were placed on a silicon wafer in a preheated oven at 100°C for 3 min and then cooled to room temperature. *H. Pluvialis* cells were selected by their encystment stage: to obtain data for HPM only non-mobile (green vegetative cells) palmella stage cells are considered whereas for SHPM mature cyst cells are studied [37]. The results shown are the average of these measurements.

2.6.*Morphological and Optical Characterization*
High resolution transmission electron microscopy (HRTEM) was carried out using a FEI-Titan 80–300 kV microscope equipped with an ultra-stable Schottky field emitter gun. Field emission scanning electron microscopy (SEM) images were acquired with a JEOL JSM-7800F microscope; EDS analysis was performed with an Oxford Instruments analyzer. Microphotographs of the cells are taken at 1 kV while the EDS analysis was performed at 8–10 kV. Three individual cells from each wafer were selected randomly. For each sample, one SEM image was obtained and the EDS analysis was performed on six different regions of the surface.
The ultraviolet–visible (UV-Vis) absorption spectra of colloidal AuNPs and of CdTe@TGA QDs were measured in transmittance using an Agilent Technologies Cary Series UV-Vis near-infrared (NIR) spectrophotometer (Cary 5000). Photoluminescence (PL) characterization of the CdTe@TGA QD, cell, and cell-QD was carried out using a 75 W Xe lamp. All measurements were taken under identical conditions. Fluorescence emission was analyzed with an Acton Research modular 2300 spectrofluorometer and a R955 Hamamatsu photomultiplier tube for visible emission under excitation of 350–500 nm. The system is PC controlled through the Spectra-Sense software. All measurements were performed at room temperature.

2.7.Optical Imaging and Confocal Microscopy of Algae Samples
Bright-field imaging was performed using an Olympus IX81 microscope controlled by an Olympus IX2-UCB microscope controller. A 20X objective lens was used. Confocal microscopy was carried out using a Zeiss LSM-710-NLO confocal microscope. Algae samples were excited at 405 nm and the emission was collected in three different spectral regions: 440–476 nm, 592–631 nm, and 670–707 nm corresponding to carotenoid, QD and chlorophyll emission, respectively. Z-stacks were collected for the selected algae with 20X/0.4 objective lens.

2.8. Raman Spectroscopy

Three cells from each wafer were selected randomly. About 150 Raman spectra were recorded in different points for each of the selected algae, and averaged to obtain a representative spectrum of each cell sample. The spectra were collected using a Renishaw Raman System (inVia Raman Microscope) with a 20X objective lens; the excitation laser wavelength was 785 nm with a power of approximately 5 mW on the sample. Integration time for each Raman measurement was 1 s [38]. For the Raman signal detection, the laser light was directly focused onto the surface of the sample. Cell and cell-QDs-AuNPs samples were measured on dry silicon substrates prepared with the previously mentioned method; the peak frequencies were calibrated by means of the silicon wafer.

2.9. Zeta Potential

Zeta potential measurements of the TGA-capped CdTe QDs and AuNPs colloids were carried out using a Malvern Instrument Zetasizer Nano (red laser 633 nm).

3.Results

3.1. Optical and Morphological Characterization of AuNPs and QDs

In order to characterize the absorption and emission properties of the CdTe@TGA QDs, UV-Vis absorption and PL spectra were acquired in colloid (Fig.1a). The absorption peak is centered at 520 nm while the emission peak is located at 560 nm under excitation at 400 nm. The emission spectra shows a wide band of 63 nm, suggesting that the sample contains a distribution of nanocrystal sizes [39]. Figure 1b shows the UV-Vis spectrum of AuNPs dispersed in aqueous solution. The surface plasmon resonance (SPR) is centered at 535 nm. The wide band in the absorption is consistent with some agglomeration of the particles due to the lack of surfactant [33]. The UV-Vis spectrum of AuNPs mixed with CdTe@TGA QDs is also presented to show that the absorption of AuNPs remains unchanged.

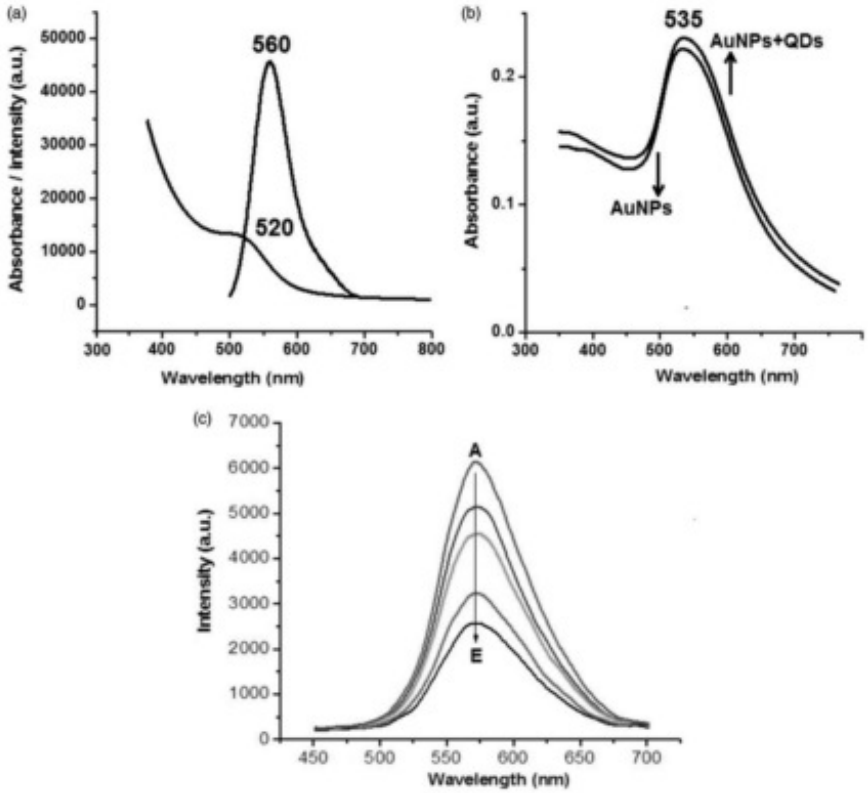

Figure 1. a) Emission and absorption spectra of TGA-CdTe QD. b) AuNPs absorption spectra. c) Photoluminescence spectra of CdTe@TGA QD in the presence of AuNPs at various concentrations (a)–(e): 0, 0.25, 0.5, 0.75, and 1.2x10^{-10}mol L^{-1}).

The PL of QDs was monitored in a mixture of QDs with different concentrations of AuNPs and no changes on the emission wavelength of the QDs due to the presence of AuNPs was found (Figure 1c). The changes in emission intensity of

QDs in the presence of AuNPs, which SRP is close to the emission of the QD, have been widely reported as a consequence of energy transfer from the QD to the AuNP [40].

CdTe@TGA QDs and AuNPs morphology was studied by HRTEM and STEM, respectively. Figure 2a shows a HRTEM image of CdTe@TGA QDs, the measured average nanocrystal size is approximately 3 nm. In order to adequately characterize the size of the CdTe@TGA QD, the following empirical fitting function, deduced by Yu et al., was used [41].

$$\mathrm{D} = (9.8127\mathrm{x}10^{-7})\lambda^3 - (1.7147\mathrm{x}10^{-3})\lambda^2 + (1.0064)\lambda - 194.84$$

In Eq. 1, D (nm) is the QDs size and h (nm) is the wavelength of the first excitonic absorption peak of the corresponding CdTe QDs sample. According to the equation the size of the CdTe@TGA QD is 2.8 nm; this is consistent with the nanoparticle size obtained by HRTEM images. The concentration of QDs is around 0.56 10^{-5}mol L^{-1}; this value is also derived from the first excitonic absorption peak [41]. This concentration is suitable for our purposes [42]. STEM micrographs were acquired for the characterization of AuNPs. A representative micrograph is shown in Figure 2b. This figure shows anisotropic AuNPs with an average diameter of 20 nm and a concentration of $7.1\mathrm{x}10^{10}$ particles/mL; these estimates were obtained based on previous reports [43,44].

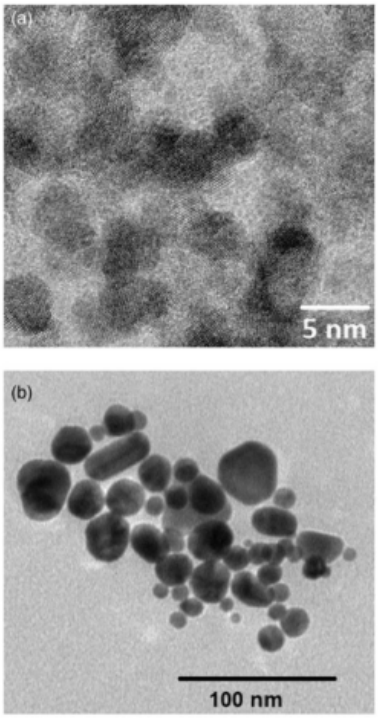

Figure 2. a) High resolution transmission electron microscopy image of CdTe@TGA QDs and b) STEM image AuNPs.

3.2. Photoluminescence Spectra of Microalgae Samples

Photoluminescence spectra of the algae samples were acquired to assess the emission wavelength of the QD after incubation with microalga. These measurements also helped to estimate the overlapping of the fluorescence emitted by the QDs and algal auto-fluorescence. The excitation wavelength in all cases was 400 nm. Figure 3 shows the PL spectrum of (a) HPM, (b) SHPM, and the normalized PL spectrum of (c) HPM-QD and (d) SHPM-QD both in the presence and absence of AuNPs; the emission band located at 449 nm corresponds to primary carotenoids and the band at 682 nm can be attributed to chlorophyll in the photosystem II [45]. The band related to the presence of secondary carotenoids appears in the region around 470–550 nm which in this case is related to the presence of astaxanthin [46]. Therefore the presence of these band is more remarkable in Figure 3b. However, in Figure 3c and 3d, this band overlaps with the strong fluorescence of the QDs. On the other hand, non-stressed cells have a higher emission associated to chlorophyll (Figure 3a) than in the case of stressed cells (Figure 3b). Both samples containing QDs (Figure 3c and d) exhibit a strong emission at 562 nm, which is attributed to the presence of QDs, and smaller peaks corresponding to the photosynthetic pigments (449 and 682 nm). The presence of AuNPs does not alter the emission wavelength of the samples, only intensity changes are observed.

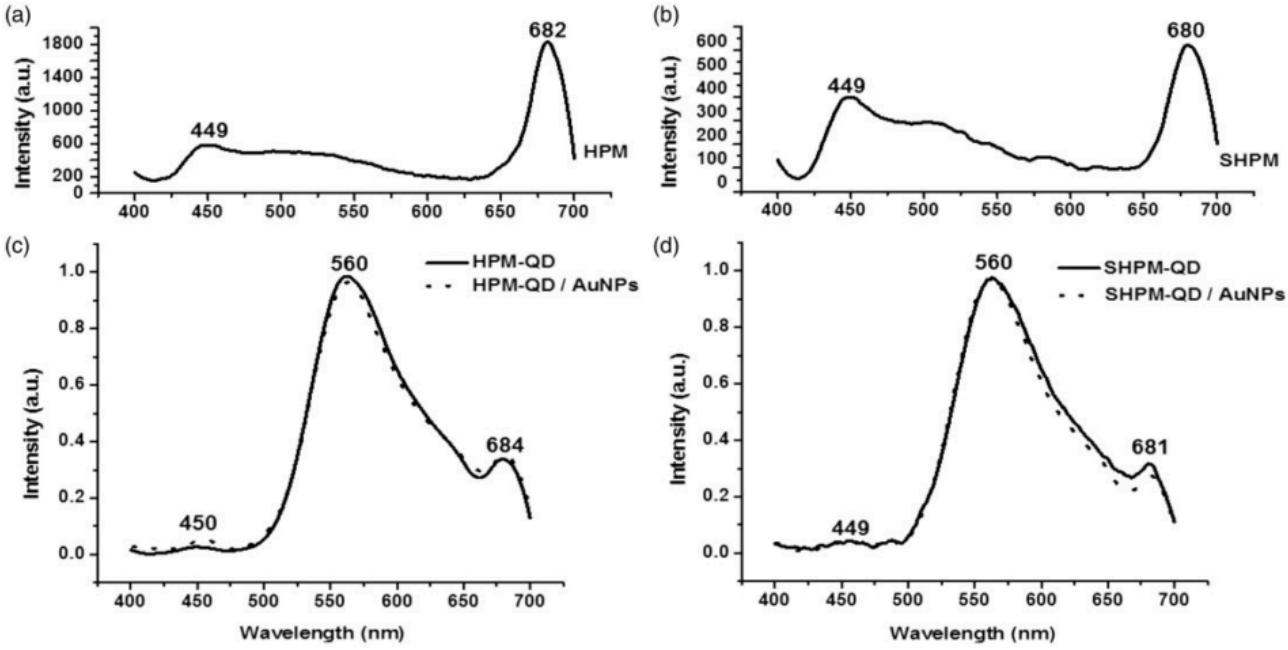

Figure 3. Photoluminescence spectrum of a) HPM, b) SHPM, c) HPM-QD and HPM-QD/AuNPs, and d) SHPM-QD and SHPM-QD/ AuNPs. Samples were exited at 400 nm.

3.3. Bright Field and Scanning Electron Microscopy

Figure 4 shows images of HPM and SHPM samples with and without QDs, obtained by optical microscopy and SEM. Figure 4a–d shows fresh algae in bright field. The presence of the ECM is clearly visible in HPM and HPM-QDs samples as a nearly transparent layer of variable thickness (Figure 4a and b) and HPM-QDs sample shows a change in color (Figure 4a and b) while as expected the ECM is absent in SHPM and SHPM-QDs cells (Figure 4c and d). Mature cyst SHPM show no significant changes when viewed in a bright field (Figure 4c and d). Scanning electron microscopy images of algae fixed on silicon are displayed in Figure 4e–h.

A distinctive round shape is observed in the control cells (Figure 4e and g). The collapse in the structure of the algae is observed for the HPM-QDs sample (Figure 4f), indicating damage to the cell. Stressed *H. pluvialis* microalgae QDs do not show such damage (Figure 4h), which is attributed to the existence of the secondary wall.

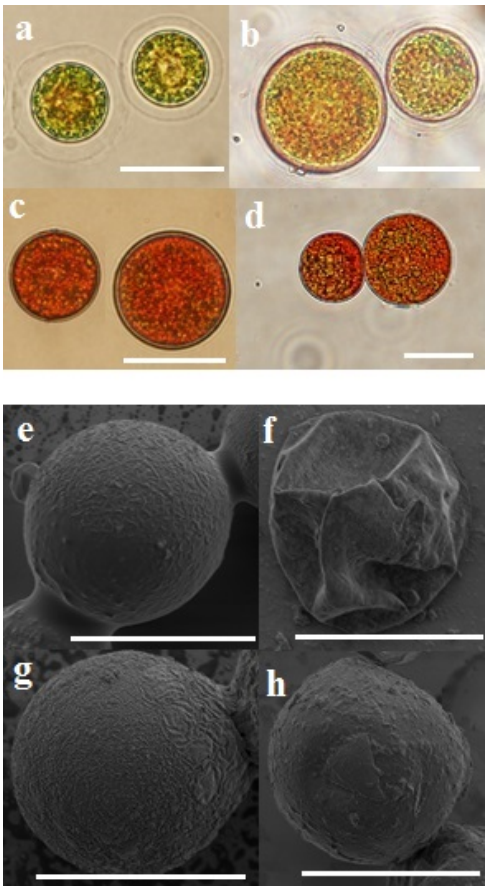

Figure 4. Bright field microscopic images of fresh HPM samples. Non- mobile “palmella” stage: a) HPM, b) HPM-QD; and mature cyst: c) SHPM, d) SHPM-QD. FSEM images of HPM fixed on silicon: e) HPM, f) HPM-QD, g) SHPM, h) SHPM-QD. Scale bar represents 20 μm.

The presence of Cd and Te on the surface of QD-treated algae was analyzed by EDS element analysis; obtained EDS spectra in the range of 2–5 keV are shown in Figure 5. The elements found in the cell-QDs samples are as follow: cadmium (Cd), tellurium (Te), carbon (C), Oxygen (O), nitrogen (N), phosphorus (P), sulfur (S), sodium (Na), and chlorine (Cl) as obtained by EDS analysis for the different algae samples. For the HPM-QD samples, Cd and Te were detected, with a larger concentration of Cd (15.6%) than Te (3.9%) (Fig. 5a and b). In contrast, for SHPM-QD smaller amounts of Cd (2.8%) and Te (0.4%) were observed than in the case of HPM-QD (Fig. 5b and d). As a control sample, EDS analysis was obtained for a drop of QDs; a greater presence of Cd is observed compared to that of Te and this has been widely reported as a result of the presence of CdS in the colloidal synthesis which can be given in the form of a shell around the CdTe core created by mercapto groups covalently attached to the surface Cd atoms [31].

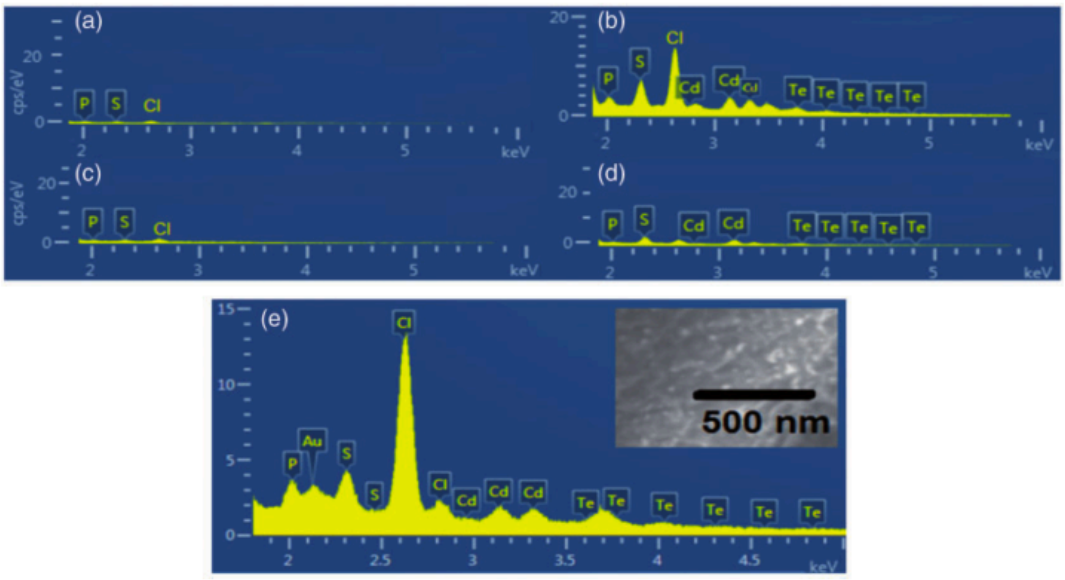

Figure 5. Energy dispersive spectrum showing the composition of a) HPM, b) HPM-QD, c) SHPM, d) SHPM-QD, and e) HPM- QDs/AuNPs, in the range of 2–5 keV. The inset in e) shows the adsorbed AuNPs.

Disruption of algal cells in samples incubated with QDs is observed (Fig. 4f). This damage to the cell structure may be a consequence of ROS and/or the occurrence of Cd ions. Both sources of CdTe QDs toxicity have been widely discussed and reported [14,15]. Also, Cd ions could have been attracted to the cell membrane, due to its negative potential[47]. The cell wall of SHPM is approximately 2 mm thick and has low permeability, therefore making it mechanically and chemically resistant[21]. Consequently, during the incubation period, few QDs are capable of interacting with the secondary wall of SHPM.

Figure 5e shows the EDS spectrum of HPM- QDs/AuNPs, the inset shows AuNPs aggregates that are found on the cell sample. These aggregates are known to promote SERS due to the high local optical fields in the hot spots of gold cluster structures. As reported, AuNP aggregates exceeding a size of 100–150 nm and

consisting of a minimum of 5–10 individual nanoparticles provide at least one hot spot exhibiting an enhancement at a level that makes these nanostructures SERS-active for non-resonant single-molecule Raman detection [38].

3.4.Confocal Microscopy

The localization of the CdTe@TGA QDs in the ECM of HPM was studied by confocal microscopy. Emission and excitation ranges were proposed based on the PL spectra presented earlier (Fig. 3). Samples were excited at 405 nm and the emission was collected in three specific bands: 440–476 nm, 560–631 nm, and 670–707 nm, corresponding to the emission of primary carotenoids, QDs, and chlorophyll, respectively. The plane in depth at which the diameter of the algae is maximum is regarded as the plane of interest for the Z-scan, was based on previously reported criteria[48]. To delimit the ECM and the plasmalemma, the emission of chlorophyll (shown in red) was taken as reference since it is known that chlorophyll is not present in the ECM [21]. In HPM (Fig. 6a–d), a considerable auto-fluorescence due to chlorophyll was seen while the signal from the primary carotenoids is low. *Haematococcus pluvialis* microalgae QDs (Fig. 6e–h) show similar chlorophyll auto- fluorescence and the QDs appear to be localized within the ECM. The SHPM-QD sample shows non-specific localization of the QDs, which appear to be in some parts on the outside of the secondary wall (Fig. 6m–p). These results are in agreement with the spectra shown in Figure 3c and d. The small signal observed in the band of 562–631 nm in HPM and SHPM samples (Fig. 6d and l) corresponds to secondary carotenoids (Fig. 3a and b).

After 5 min of incubation, CdTe@TGA QDs were not internalized and accumulate in the ECM of HPM. Confocal images for SHPM-QD show a very small amount of QDs on the outside of the secondary wall. The secondary wall of SHPM is thought to be acting as a barrier. Complete internalization was probably prevented by the thick cell wall of these algae. Internalization of AuNPs is also not observed/ Since HPM has no such secondary wall, CdTe@TGA QDs could adsorb onto the ECM. This is consistent with that reported by Mahan et al.[27]. Complete internalization was probably prevented by the thick cell wall of these algae.

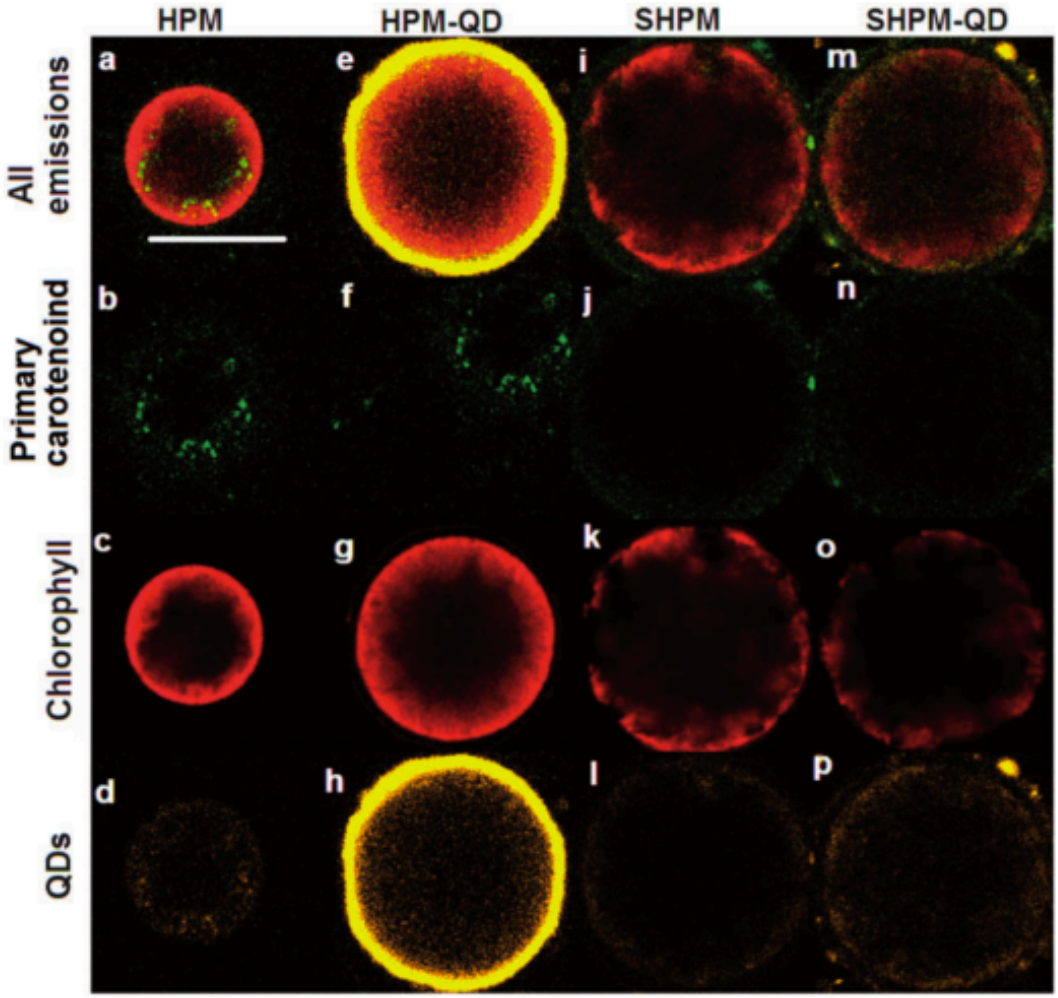

Figure 6. Confocal microscopy images of microalgae: (a–d) HPM, (e–h) HPM-QD, (i–l) SHPM, and (m–p) SHPM-QD. First row corresponds to all emissions, second row shows the florescence of primary carotenoids, third row corresponds to chlorophyll emission, and fourth row corresponds toQD emission. Samples are excited at 405 nm and the emission is collected in three specific bands: 440–476 nm, 592–631 nm, and 670–707nm, corresponding to the emission of carotenoids, QDs, and chlorophyll, respectively. Scale bar 20mm.

3.5. Raman Spectroscopy

SERS measurements were carried out by the incubation of the algae with the naked AuNPs that do not present any bands in the Raman spectrum. Since the SRP of the AuNPs is located at 535 nm while the excitation signal used is 785 nm, observation of SERS enhancement is explained by the formation of aggregates that could resonate at wavelengths greater than its SRP [28,30,38].

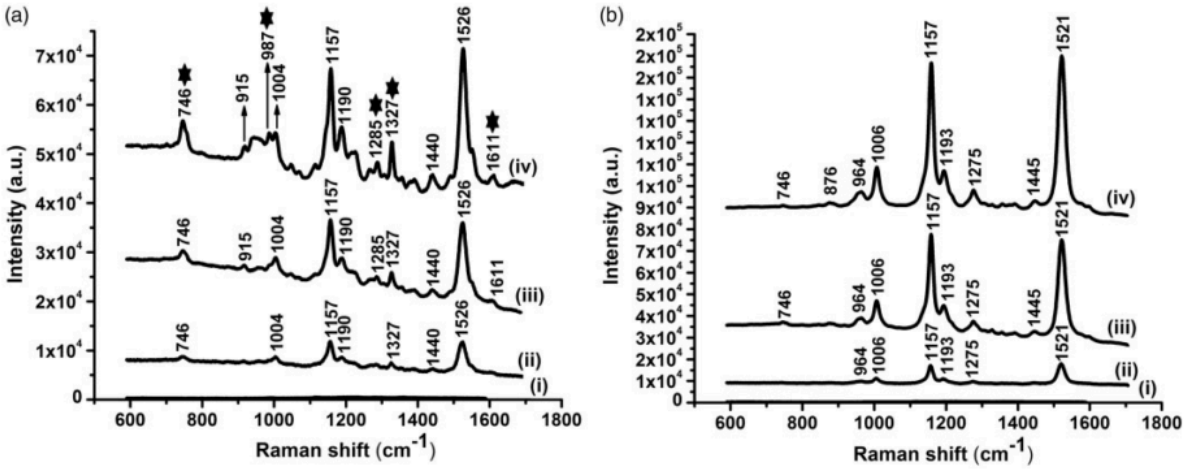

Figure 7. a) Raman spectra obtained from: (i) AuNPs, (ii) HPM, (iii) HPM/AuNPs, and (iv) HPM-QDs/AuNPs. Stars indicate the bands that increased intensity after incubation with CdTe@TGA QDs. b) Raman spectra obtained from: (i) AuNPs, (ii) SHPM, (iii) SHPM/ AuNPs, and (iv) SHPM-QDs/AuNPs. Peaks

Figure 7 displays the SERS spectra obtained for the HPM and SHPM samples. The AuNPs enhanced the Raman signal by approximately five times in comparison to normal Raman measurements (Figure 7a and b, panels (ii) and (iii)). Figure 7a (iii) shows the Raman spectrum of HPM/AuNPs, characteristic peaks associated to chlorophyll (746, 987, 1046, 1285, 1305, 1327, 1490, 1550, and 1611 cm^{-1})[49–53] and carbohydrates (1069 and 1112 cm^{-1})[22,50,54,55] are present. As reported, around 42% of HPM volume is constituted by chloroplasts [22]. The bands at 1157 and 1526 cm^{-1} are assigned to the presence of both primary and secondary carotenoids, being the primary carotenoids those known to be found in a higher concentration in the HPM (Figure 7a (iii)). In the Raman spectrum of HPM-QDs/ AuNPs, some peaks associated with chlorophyll increased their intensity; these peaks are marked with stars in Figure 7a (iv), and the range between 915 and 1004 cm^{-1} shows significant changes. For instance, whereas HPM/ AuNPs (Figure 7a (iii)) shows a band at 963 cm^{-1} attributed to the O–C–H bending vibration of carbohydrates, features at 940 cm^{-1} appear in HPM-QDs/AuNPs (Figure 7a (iv)).

Peaks associated to chlorophyll are absent or minimal in the SHPM/AuNPs (Figure 7b (iii)) sample; however, carotenoid (964, 1006, 1157, 1193, 1275, 1445, 1521, and 1596 cm^{-1})[19,49,56–59] and lipid (876 cm^{-1}) bands corresponding to astaxanthin accumulation [20,21] are present polysaccharides like algaenan and mannan [21] (Figure 7b (iii)). The band at 1157 cm^{-1} is assigned to v2 carotenoids (stretching C–C) while the band at 1521–1522 cm^{-1} is assigned to v1 carotenoids (in-phase C=C) [19,60]. Overall, no spectral changes after incubation with QDs are detected for SHPM-QD/AuNPs (Figure 7b (iv)). CdTe@TGA QDs were not internalized but adsorbed and distributed in the ECM, this meets the optimum

conditions for SERS enhancement that enables chemical probing of the interaction of QD with the ECM in the nano-environment of the AuNPs.

It is not surprising that changes between HPM/AuNPs and HPM-QDs/AuNPs manifest in a band assigned mostly to carbohydrates since the main component of the ECM of HPM are glycoproteins which have a high carbohydrate content such that protein content constitutes in some cases only 5% of the glycoprotein weight [67]. In addition, the chemical composition of the ECM and the algae cell wall consists of cellulose, polysaccharides, and the aforementioned glycoproteins. Therefore it has numerous binding sites for CdTe@TGA QDs through nonspecific interactions (such as electrostatic, hydrophobic, and hydrogen bonding) or the interaction between the carboxylic groups (–COOH) of the TGA and the amine groups ($–NH_2$) of the ECM and the algal cell wall [27]. Moreover the band with maximum at 940 cm^{-1} has been reported as out-of-phase C–O–C ring vibrations of poly- saccharides [68]. Therefore the manifestation of this band after incubation with CdTe@TGA QDs strongly suggests the interaction of the CdTe@TGA QDs with the saccharides. Sugar-modified CdTe@TGA QDs have been widely discussed and can be produced by simple incubation of CdTe@TGA with saccarides [69]. As has been reported, quantum yields are related to traps on the surface of CdTe QDs that mainly originate from Te atoms with dangling bonds and these traps could be occupied by saccharides that can adhere to the surface of the CdTe QDs by electrostatic forces. This occurs, for example, with D-glucose, a sugar present in plant cells [69].

Previous reports show that Raman modes corresponding to the crystalline core, Te defects of the CdTe QDs, and the interactions between the QD core and the thiol capping are found in the low Raman shift regime (100–310 cm^{-1}) and vibrational modes of the thiol capping agents have been reported between 310 and 1750 cm^{-1}. Reported CdTe@TGA QDs shifts are not found in any spectra of the alga samples due to their weak Raman scattering in aqueous media compared to elastic scattering [65].
Several peaks of HPM-QDs/AuNps, in the region of 1100–1620 cm^{-1} assigned to chlorophyll increased their intensity (approximately three times) compared to the intensities of the same peaks of HPM/AuNPs and with reference to the characteristic peaks of carotenoid bands (1157–1526 cm^{-1}). This increase of the intensity given the presence of the CdTe@TGA QDs may indicate that ROS are already attacking the HPM. This is consistent with previous reports indicating that when HPM are subjected to ROS the chloroplast is found to be the main site of oxidative damage [25]. Therefore the increase in intensity of chlorophyll-associated bands in HPM-QDs/AuNps could be a direct result of ROS interacting with the chloroplasts and damaging the structure, thus releasing the chlorophyll.
Raman spectrum of SHPM exhibits no changes after incubation with QDs, indicating that the interaction between the CdTe@TGA QD and the secondary cell wall is very low. However, a small presence of TGA CdTe-QDs in SHPM-QDs sample is confirmed by EDS analysis, the PL spectrum, and confocal microscopy. A protective role of astaxanthin against QD toxicity is not confirmed due to the absence of internalized QDs in SHPM-QD.

3.6.*Interaction of CdTe@TGA QDs with AuNPs*

The well-dispersed AuNPs possess a slightly negative charge (10 mV), probably due to the adsorption of ions on the surface of the AuNPs [61], and the zeta potential of CdTe@TGA QDs was measured to be 27.3 mV. Due to the ionization of the –COOH group [62], there is no electrostatic attraction between the negatively charged AuNPs and QDs. Moreover, the absorption spectrum of AuNPs remained unchanged in the presence of CdTe@TGA QDs, therefore the observed fluorescence decrease of CdTe@TGA QDs in the presence of AuNPs should be attributed to the inner filter effect in which there is no chemical interaction between the two nanoparticles [63]. The chemical interactions between these nanoparticles after being adsorbed on the cell remains unknown.

4.Conclusions

The findings in this study prove that CdTe@TGA QDs interact with the ECM of *Haematococcus pluvialis* microalgae cells after 5 min of incubation. Evidence of an interaction between the ECM and CdTe@TGA QDs in the Raman spectrum of a unicellular microalga is obtained by SERS, the Raman signal is highly increased when using aggregated AuNPs. Changes between in the Raman spectrum of HPM/AuNPs and HPM-QDs/AuNPs are found and suggest the existence of interactions between the –COOH group of CdTe@TGA QDs with saccharides present in the ECM as well as possible damage to chloroplasts due to ROS. While for SHPM and SHPM-QDs no changes in the Raman spectra are detected. Future endeavors will focus on the detection and isolation of sugars present in the ECM to analyze and validate these observations and the possible formation of QDs conjugates.

References

[1] S. Paul, C. Pearson, A. Molloy, M. Cousins, M. Green, S. Kolliopoulou,

[2] P. Dimitrakis, P. Normand, D. Tsoukalas, M. Petty. ‘‘Langmuir-Blodgett Film Deposition of Metallic Nanoparticles and Their Application to Electronic Memory Structures’’. Nano Letters. 2003. 3: 533–536.

[3] K.S. Soppimath, T.M. Aminabhavi, A.R. Kulkarni, W.E. Rudzinski. ‘‘Biodegradable Polymeric Nanoparticles as Drug Delivery Devices’’.

[4] J. Controlled Release. 2001. 70: 1–20.

[5] V.L. Colvin. ‘‘The Potential Environmental Impact of Engineered Nanomaterials’’. Nat. Biotechnol. 2003. 21: 1166–1170.

[6] M.P. Sk, A. Jaiswal, A. Paul, S.S. Ghosh, A. Chattopadhyay. ‘‘Presence of Amorphous Carbon Nanoparticles in Food Caramels’’. Scientific Reports. 2012. 2: 383.

[7] T. Wang, J. Bai, X. Jiang, G.U. Nienhaus. ‘‘Cellular Uptake of Nanoparticles by Membrane Penetration: A Study Combining Confocal Microscopy with FTIR Spectroelectrochemistry’’. ACS Nano. 2012. 6(2): 1251–1259.

[8] I.A. Worms, J. Boltzman, M. Garcia, V.I. Slaveykova. ‘‘Cell-Wall- Dependent Effect of Carboxyl-Cdse/Zns Quantum Dots on Lead and Copper Availability to Green Microalgae’’. Environmental Pollution. 2012. 167: 27–33.

[9] T. J. Stewart, J. Szlachetko, L. Sigg, R. Behra, M. Nachtegaal. ‘‘Tracking the Temporal Dynamics of Intracellular Lead Speciation in a Green Alga’’. Environmental Sci. Technol. 2015. 49(18): 11176–11181.

[10] F. Yuriel Núñez, I. V. Mikhail. ‘‘Optical Properties of Bulk and Nanocrystalline Cadmium Telluride’’. In: J.F. Donegan, Y.P. Rakovich (eds) Cadmium Telluride Quantum Dots: Advances and Applications. Singapore: Pan Stanford Publishing, 2013, pp.1–22.

[11] G. Iyer, F. Pinaud, J. Tsay, S. Weiss. ‘‘Solubilization of Quantum Dots with a Recombinant Peptide from Escherichia Coli’’. Small. 2007. 3(5): 793–798.

[12] M. Nurunnabi, K.J. Cho, J.S. Choi, K.M. Huh, Y.-K. Lee. ‘‘Targeted Near-IR Qds-Loaded Micelles for Cancer Therapy and Imaging’’. Biomaterials. 2010. 31(20): 5436–5444.

[13] W. Yvonne, C. Jennifer, V. Yuri. ‘‘Biocompatibility and Cellular Localisation of CdTe Quantum Dots’’. In: J.F. Donegan, Y.P. Rakovich (eds) Cadmium Telluride Quantum Dots: Advances and Applications. Singapore: Pan Stanford Publishing, 2013, pp.205–229.

[14] C. Anthony Le, S. Alyona, N. Igor. ‘‘Biological Applications of Cadmium Telluride Semiconductor Quantum Dots’’. In: J.F. Donegan,

[15] Y.P. Rakovich (eds) Cadmium Telluride Quantum Dots: Advances and Applications. Singapore: Pan Stanford Publishing, 2013, pp.173–204.

[16] K. Boldt, O. T. Bruns, N. Gaponik, A. Eychmüller. ‘‘Comparative Examination of the Stability of Semiconductor Quantum Dots in Various Biochemical Buffers’’. The J. Phys. Chem. B. 2006. 110(5): 1959–1963.

[17] R. Schneider, C. Wolpert, H. Guilloteau, L. Balan, J. Lambert,

[18] C. Merlin. ‘‘The Exposure of Bacteria to CdTe-Core Quantum Dots: The Importance of Surface Chemistry on Cytotoxicity’’. Nanotechnology. 2009. 20(22): 225101

[19] J. Lovrić, H.S. Bazzi, Y. Cuie, G.R. Fortin, F.M. Winnik, D. Maysinger. ‘‘Differences in Subcellular Distribution and Toxicity of Green and Red Emitting CdTe Quantum Dots’’. J. Mol. Med. (Heidelberg, Germany). 2005. 83(5): 377–385.

[20] G. Nikolai. ‘‘Assemblies of Thiol-Capped CdTe Nanocrystals’’. In: J.F. Donegan,

Y.P. Rakovich (eds) Cadmium Telluride Quantum Dots: Advances and Applications. Singapore: Pan Stanford Publishing, 2013, pp.61–77.
[21] M. Kobayashi, Y. Kurimura, Y. Tsuji. ‘‘Light-Independent, Astaxanthin Production by the Green Microalga Haematococcus Pluvialis under Salt Stress’’. Biotechnology Letters. 1997. 19(6): 507–509.
[22] S. Boussiba. ‘‘Carotenogenesis in the Green Alga Haematococcus Pluvialis: Cellular Physiology and Stress Response’’. Physiol. Plant. 2000. 108(2): 111–117.
[23] A.M. Collins, H.D. Jones, D. Han, Q. Hu, T.E. Beechem, J.A. Timlin. ‘‘Carotenoid Distribution in Living Cells of Haematococcus Pluvialis (Chlorophyceae)’’. PloS One. 2011. 6: e24302.
A. Kaczor, K. Turnau, M. Baranska. ‘‘In Situ Raman Imaging of Astaxanthin in a Single Microalgal Cell’’. Analyst. 2011. 136: 1109–1112.
B. Hagen, S. Siegmund, W. Braune. ‘‘Ultrastructural and Chemical Changes in the Cell Wall of Haematococcus Pluvialis (Volvocales, Chlorophyta) During Aplanospore Formation’’. European Journal of Phycology. 2002. 37: 217–226.
[24] M. Wayama, S. Ota, H. Matsuura, N. Nango, A. Hirata, S. Kawano. ‘‘Three-Dimensional Ultrastructural Study of Oil and Astaxanthin Accumulation During Encystment in the Green Alga Haematococcus Pluvialis’’. PLOS One. 2013. 8: e53618.
[25] E. Morelli, P. Cioni, M. Posarelli, E. Gabellieri. ‘‘Chemical Stability of Cdse Quantum Dots in Seawater and Their Effects on a Marine Microalga’’. Aquat. Toxicol. 2012. 122–123: 153–162.
[26] E. Morelli, E. Salvadori, R. Bizzarri, P. Cioni, E. Gabellieri. ‘‘Interaction of Cdse/Zns Quantum Dots with the Marine Diatom Phaeodactylum Tricornutum and the Green Alga Dunaliella Tertiolecta: A Biophysical Approach’’. Biophys. Chem. 2013. 182: 4–10.
[27] D. Han, J. Wang, M. Sommerfeld, Q. Hu. ‘‘Susceptibility and Protective Mechanisms of Motile and Non Motile Cells of Haematococcus Pluvialis (Chlorophyceae) to Photooxidative Stress’’. J. Phycol. 2012. 48(3): 693–705.
[28] Y. Wang, A.-J. Miao, J. Luo, Z.-B. Wei, J.-J. Zhu, L.-Y. Yang. ‘‘Bioaccumulation of CdTe Quantum Dots in a Freshwater Alga Ochromonas Danica: A Kinetics Study’’. Environ. Sci. Technol. 2013. 47(18): 10601–10610.
[29] S. Lin, P. Bhattacharya, N.C. Rajapakse, D.E. Brune, P.C. Ke. ‘‘Effects of Quantum Dots Adsorption on Algal Photosynthesis’’. J. Phys. Chem. C. 2009. 113(25): 10962–10966.
[30] J. Kneipp, H. Kneipp, K. Kneipp. ‘‘SERS—a Single-Molecule and Nanoscale Tool for Bioanalytics’’. Chem. Soc. Rev. 2008. 37(5): 1052–1060.
[31] T.-H. Lee, H.-Y. Wang. ‘‘Simultaneous Quantification of Cellular Lipids and Carotenoids inside Chlorella Vulgaris Using Raman Spectrometry’’. Energy Procedia. 2014. 61: 829–833.
[32] K. Kneipp, H. Kneipp, J. Kneipp. ‘‘Surface-Enhanced Raman Scattering in Local Optical Fields of Silver and Gold Nanoaggregates from Single- Molecule Raman Spectroscopy to Ultrasensitive Probing in Live Cells’’. Acc. Chem. Res. 2006. 39(7): 443–450.
[33] N. Gaponik, D.V. Talapin, A.L. Rogach, K. Hoppe, E.V. Shevchenko,
[34] Kornowski, A. Eychmüller, H. Weller. ‘‘Thiol-Capping of CdTe Nanocrystals: An Alternative to Organometallic Synthetic Routes’’. J. Phys. Chem. B. 2002. 106(29): 7177–7185.
[35] M.N. Martin, J.I. Basham, P. Chando, S.-K. Eah. ‘‘Charged Gold Nanoparticles in

Non-Polar Solvents: 10-min Synthesis and 2D Self- Assembly''. Langmuir. 2010. 26(10): 7410–7417.
[36] M. Hossain, Y. Kitahama, G. Huang, T. Kaneko, Y. Ozaki. ''SPR and SERS Characteristics of Gold Nanoaggregates with Different Morphologies''. Applied Physics B. 2008. 93(1): 165–170.
[37] L. Recht, A. Zarka, S. Boussiba. ''Patterns of Carbohydrate and Fatty Acid Changes under Nitrogen Starvation in the Microalgae Haematococcus Pluvialis and Nannochloropsis Sp''. Appl. Microbiol. Biotechnol. 2012. 94(6): 1495–1503.
A. Goldstein, Y. Soroka, M. Frušić-Zlotkin, I. Popov, R. Kohen. ''High Resolution SEM Imaging of Gold Nanoparticles in Cells and Tissues''. J. Microsc. (Oxford, U.K.). 2014. 256(3): 237–247.
[38] C.M. Krishna, G. Sockalingum, J. Kurien, L. Rao, L. Venteo, M. Pluot,
[39] M. Manfait, V. Kartha. ''Micro-Raman Spectroscopy for Optical Pathology of Oral Squamous Cell Carcinoma''. Appl. Spectrosc. 2004. 58(9): 1128–1135.
[40] A.S. Kristoffersen, Ø. Svensen, N. Ssebiyonga, S.R. Erga, J.J. Stamnes, Ø. Frette. ''Chlorophyll a and NADPH Fluorescence Lifetimes in the Microalgae Haematococcus Pluvialis (Chlorophyceae) under Normal

[41] and Astaxanthin-Accumulating Conditions''. Appl. Spectrosc. 2012. 66(10): 1216–1225.
[42] K. Kneipp, A.S. Haka, H. Kneipp, K. Badizadegan, N. Yoshizawa,
[43] C. Boone, K.E. Shafer-Peltier, J.T. Motz, R.R. Dasari, M.S. Feld. ''Surface-Enhanced Raman Spectroscopy in Single Living Cells Using Gold Nanoparticles''. Appl. Spectrosc. 2002. 56(2): 150–154.
[44] Z.-Z. Sun, D. Ding, Q. Gong, W. Zhou, B. Xu, Z.-G. Wang. ''Quantum- Dot Superluminescent Diode: A Proposal for an Ultra-Wide Output Spectrum''. Opt. Quantum Electron. 1999. 31(12): 1235–1246.
[45] J. Guo, X. Liu, H. Gao, J. Bie, Y. Zhang, B. Liu, C. Sun. ''Highly Sensitive Turn-on Fluorescent Detection of Cartap via a Nonconjugated Gold Nanoparticle–Quantum Dot Pair Mediated by Inner Filter Effect''. RSC Advances. 2014. 4(52): 27228–27235.
[46] W.W. Yu, L. Qu, W. Guo, X. Peng. ''Experimental Determination of the Extinction Coefficient of CdTe, CdSe, and CdS Nanocrystals''. Chem. Mater. 2003. 15(14): 2854–2860.
[47] J.K. Jaiswal, H. Mattoussi, J.M. Mauro, S.M. Simon. ''Long-Term Multiple Color Imaging of Live Cells Using Quantum Dot Bioconjugates''. Nat. Biotechnol. 2003. 21: 47–51.
[48] W. Haiss, N.T. Thanh, J. Aveyard, D.G. Fernig. ''Determination of Size and Concentration of Gold Nanoparticles from UV-Vis Spectra''. Anal. Chem. 2007. 79(11): 4215–4221.
[49] N.G. Khlebtsov. ''Determination of Size and Concentration of Gold Nanoparticles from Extinction Spectra''. Anal. Chem. 2008. 80(17): 6620–6625.
[50] F. Franck, P. Juneau, R. Popovic. ''Resolution of the Photosystem I and Photosystem II Contributions to Chlorophyll Fluorescence of Intact Leaves at Room Temperature''. Biochim. Biophys. Acta, Bioenerg. 2002. 1556(2–3): 239–246.
[51] P. Régnier, J. Bastias, V. Rodriguez-Ruiz, N. Caballero-Casero,
[52] Caballo, D. Sicilia, A. Fuentes, M. Maire, M. Crepin,
[53] Letourneur. ''Astaxanthin from *Haematococcus Pluvialis* Prevents Oxidative Stress on Human Endothelial Cells without Toxicity''. Mar. Drugs. 2015. 13(5): 2857–2874.

[54] Z. Wu, Y. Zhu, W. Huang, C. Zhang, T. Li, Y. Zhang, A. Li. ‘‘Evaluation of Flocculation Induced by Ph Increase for Harvesting Microalgae and Reuse of Flocculated Medium’’. Bioresour. Technol. 2012. 110: 496–502.
A. Tatyana, K. Min Seok, H. Jong Won, M. Taizo, N. Chikako, K. Gwang Hoon. ‘‘Cold-Tolerant Strain of *Haematococcus Pluvialis* (Haematococcaceae, Chlorophyta) from Blomstrandhalvøya (Svalbard)’’. Algae. 2013. 28(2): 185–192.
[55] P. Heraud, J. Beardall, D. McNaughton, B.R. Wood. ‘‘In Vivo Prediction of the Nutrient Status of Individual Microalgal Cells Using Raman Microspectroscopy’’. FEMS Microbiol. Lett. 2007. 275(1): 24–30.
[56] B.R. Wood, P. Heraud, S. Stojkovic, D. Morrison, J. Beardall,
[57] D. McNaughton. ‘‘A Portable Raman Acoustic Levitation Spectroscopic System for the Identification and Environmental Monitoring of Algal Cells’’. Anal. Chem. 2005. 77(15): 4955–4961.
[58] Z.-L. Cai, H. Zeng, M. Chen, A.W. Larkum. ‘‘Raman Spectroscopy of Chlorophyll D from Acaryochloris Marina’’. Biochim. Biophys. Acta, Bioenerg. 2002. 1556(2–3): 89–91.
[59] X. Wei, D. Jie, J.J. Cuello, D.J. Johnson, Z. Qiu, Y. He. ‘‘Microalgal Detection by Raman Microspectroscopy’’. TrAC Trends Anal. Chem. 2014. 53: 33–40.
[60] Y. Koyama, Y. Umemoto, A. Akamatsu, K. Uehara, M. Tanaka. ‘‘Raman Spectra of Chlorophyll Forms’’. J. Mol. Struct. 1986. 146: 273–287.
I. Notingher. ‘‘Raman Spectroscopy Cell-Based Biosensors’’. Sensors. 2007. 7(8): 1343–1358.
[61] J. De Gelder, K. De Gussem, P. Vandenabeele, L. Moens. ‘‘Reference Database of Raman Spectra of Biological Molecules’’. J. Raman Spectrosc. 2007. 38(9): 1133–1147.
A. Kaczor, M. Baranska. ‘‘Structural Changes of Carotenoid Astaxanthin in a Single Algal Cell Monitored in Situ by Raman Spectroscopy’’. Anal. Chem. 2011. 83(20): 7763–7770.

[62] Z. Pilát, S. Bernatová, J. Ježek, M. Šery, O. Samek, P. Zemánek,
[63] L. Nedbal, M. Trtílek. ‘‘Raman Microspectroscopy of Algal Lipid Bodies: b-Carotene Quantification’’. J. Appl. Phycol. 222222. 24(3): 541–546
[64] C. Uragami, E. Yamashita, A. Gall, B. Robert, H. Hashimoto. ‘‘Application of Resonance Raman Microscopy to in Vivo Carotenoid’’. Acta Biochim. Pol. 2012. 59(1): 53–56.
[65] J.C. Merlin. ‘‘Resonance Raman Spectroscopy of Carotenoids and Carotenoid-Containing Systems’’. Pure Appl. Chem. 1985. 57(5): 785–792.
A. Dementjev, J. Kostkevičiene. ‘‘Applying the Method of Coherent
[66] Anti-Stokes Raman Microscopy for Imaging of Carotenoids in Microalgae and Cyanobacteria’’. J. Raman Spectrosc. 2013. 44(7): 973–979.
[67] J.S. Kim, E. Kuk, K.N. Yu, J.-H. Kim, S.J. Park, H.J. Lee, S.H. Kim,
[68] Y.K. Park, Y.H. Park, C.-Y. Hwang. ‘‘Antimicrobial Effects of Silver Nanoparticles’’. Nanomedicine (NY, NY, US). 2007. 3(1): 95–101.
[69] L. Vladimir, G. Nikolai, E. Alexander. ‘‘Aqueous Synthesis of Colloidal CdTe Nanocrystals’’. In: J.F. Donegan, Y.P. Rakovich (eds) Cadmium Telluride Quantum Dots: Advances and Applications. Singapore: Pan Stanford Publishing, 2013, pp.23–59.
[70] X. Cui, M. Liu, B. Li. ‘‘Homogeneous Fluorescence-Based Immunoassay Via Inner Filter Effect of Gold Nanoparticles on

[71] Fluorescence of CdTe Quantum Dots''. Analyst. 2012. 137(14): 3293–3299.
A. Albanese, W.C. Chan. ''Effect of Gold Nanoparticle Aggregation on Cell Uptake and Toxicity''. ACS Nano. 2011. 5(7): 5478–5489.
[72] J.S. Mak, A.A. Farah, F. Chen, A.S. Helmy. ''Photonic Crystal Fiber for Efficient Raman Scattering of CdTe Quantum Dots in Aqueous Solution''. ACS Nano. 2011. 5(5): 3823–3830.
[73] J. Zhao, Z. Zhang, Z. Yu, Z. He, S. Yang, H. Jiang. ''Nucleation and Characterization of Hydroxyapatite on Thioglycolic Acid-Capped Reduced Graphene Oxide/Silver Nanoparticles in Simplified Simulated Body Fluid''. Appl. Surf. Sci. 2014. 289: 89–96.
[74] M. Josè-Estanyol, P. Puigdomènech. ''Plant Cell Wall Glycoproteins and Their Genes''. Plant Physiol. Biochem. 2000. 38(1–2): 97–108.
A. Galat. ''Study of the Raman Scattering and Infrared Absorption Spectra of Branched Polysaccharides''. Acta Biochim. Pol. 1980. 27(2): 135–142.
[75] J. Coulon, I. Thouvenin, F. Aldeek, L. Balan, R. Schneider. ''Glycosylated Quantum Dots for the Selective Labelling of Kluyveromyces Bulgaricus and Saccharomyces Cerevisiae Yeast Strains''. J. Fluoresc. 2010.

CHAPTER 5
Characterization of cellular systems

Surface Enhanced Raman Spectroscopy Analysis of HeLa Cells Using a Multilayer Substrate

This chapter has been published as:
I. Aguilar-Hernández, et al., Proc. SPIE 10453, Third Int. Conf. Appl. Opt. Photonics 1045312 (2017).
DOI: 10.1117/12.2272026

Chapter 5

Surface Enhanced Raman Spectroscopy Analysis of HeLa cells Using a Multilayer Substrate

1.introduction

Non-destructive techniques like IR and Raman spectroscopy can provide useful information regarding the overall biochemical composition of cells and tissues in their native state [1], where no extraction steps are needed, and sample preparation is minimal. Unlike IR spectroscopy, water has very weak Raman scattering and does not cause interference within the sample. Consequently, Raman spectroscopy is an ideal technique for the fast chemical analysis of biological samples.

Some cells and tissues have been analyzed by normal Raman spectroscopy with adequate resolution (e.g., carotenoid [2] or heme group-containing cells [3]) but for other cell types the resulting spectra can exhibit low signal-to-noise ratio. A known limitation of normal Raman spectroscopy is the low sensitivity when the analytes are present at very low concentrations[4], as in the case of biological samples. In addition, since the analytical signal is proportional to the laser power, the sample can be suffer damage when attempting to obtain adequate spectra [5]. Surface Enhanced Raman Spectroscopy (SERS) is a technique that can help overcome the above limitations, allowing the ultrasensitive detection of molecules within cells. SERS is a based on the plasmonic properties of metallic nanostructures. The degree of signal enhancement is influenced by the material, size, degree of aggregation and shape of the nanostructure [6]; Nanoparticles with sharp corners or edges are known to generate exceptionally high SERS enhancements [6]–[8].

SERS can be obtained when working with nanoparticle colloids, SERS tags [9], [10] or solid substrates[11], [12]. SERS substrates can be assembled by both top-down and bottom-up methods in a control and reproducible approach, and tuned for a specific excitation wavelength. A main advantage when analyzing cells with SERS substrates is that there is no need for nanoparticle internalization or incubation, and is label free [13].Substrates with solely nanospheres or nanocubes have been previously studied using probe molecules [6], [14]–[16], though little efforts have been made in the analysis of samples of biological importance using this type of solid substrate and no previous reports have been found on the analysis of cells.

In this work, a multilayer solid substrate was assembled via a layer-by layer deposition of spherical nanoparticles with a top layer of concave nanocubes. The HeLa cell line was used as a model biological sample. High enhancement of representative bands associated to proteins, lipids and carbohydrates were obtained. To the best of our knowledge, this is the first study where the SERS spectra of HeLa cells have been obtained with such high resolution/signal-to-noise ratio using a solid SERS substrate [17]. The properties of this new substrate endow to conventional Raman with exciting odds to be a successful analytical tool for cell analysis. By incorporating new SERS substrates into the biological sample analysis, the molecular structural scanning and cell imaging technique can be improved.

2.Experimental details

2.1. Reagents

Tetrachloroauric acid ($HAuCl_4$), trisodium citrate dihydrate, sodium borohydride ($NaBH_4$), silver nitrate ($AgNO_3$), cetyltrimethylammonium chloride (CTAC), ascorbic acid, hydrochloric acid, 1-3 propanedithiol and 3-(aminopropyl)trimethoxysilane (APTMS) were obtained from Sigma-Aldrich. Hydrofluoric acid 50 % was purchased from Tedia. Methanol and isopropyl alcohol were HPLC grade (J.T. Baker). Water used for cleaning, preparation of aqueous solutions and substrate fabrication was ultrapure (Resistivity> 18.2 mΩ/cm) obtained with a Millipore MQ system.

2.2. Synthesis of colloidal nanoparticles

Spherical gold nanoparticles were prepared by a well established method of gold citrate reduction [18], [19] with slight modifications. Briefly, 125 mL of deionized water were vigorously stirred and brought to a rolling boil. Then, 2 mL of a $HAuCl_4$ solution (28.9 mM) were added, immediately followed by 10 mL of sodium citrate (17 mM). The reaction mixture was removed from heat and stirring continued for 15 minutes.

Concave gold nanocubes were synthesized by a seed mediated method previously reported [20]. Seed solution was prepared by the consecutive addition of 125 μL of $HAuCl_4$ (10mM) and 300 μL of fresh ice-cold $NaBH_4$ (10mM) to 5mL of CTAC (0.1M) under continuous stirring. Stirring was maintained for 2 minutes after the addition of $NaBH_4$, and left undisturbed for 2 hours. A growth solution was prepared by adding 250 μL of $HAuCl_4$ (10mM) to 4mL of CTAC (0.1mM), followed by 50 μL of ice cold $AgNO_3$ (10mM), 100 μL of HCl (1M) and 50 μL of ascorbic acid (0.1M). For growth initiation, 20 μL of a diluted seed solution (1:10) were added to the growth solution, gently stirred for 3 minutes and left undisturbed overnight.

2.3. Assembly of multilayer nanosphere substrates (GNSS)

Gold nanosphere substrates (GNSS) were fabricated by the self-assembly of metallic nanoparticles in the surface of a functionalized glass slide [18], [21]. 1 cm^2 glass slides were cleaned thoroughly and rinsed with deionized water. Slides were treated with hydrofluoric acid (5% v/v) for 45 minutes and rinsed. Afterwards, slides were silanized by incubation in a methanolic solution of *APTMS* 9% (v/v). In order to assemble a monolayer of gold nanospheres, silanized slides were immersed in a gold nanosphere colloidal solution for 24 hours and rinsed with ultrapure water.

For the multilayer substrate assembly, monolayer substrates were submerged in an aqueous solution of 1,3-propanedithiol for 30 minutes, washed with methanol and immersed in a gold nanoparticle solution for 30 minutes. This process was repeated 3 times.

2.4. Assembly of concave nanocube substrates (GNCS)

Multilayer nanosphere substrates (GNSS) were immersed in a fresh solution of 1,3-propanedithiol and allowed to react for 45 minutes. Afterwards, substrates were rinsed with methanol and submerged in a colloidal solution of gold nanocubes for 2 hours.

2.5. Cell culture

HeLa cells were cultured in DMEM media supplemented with 10% fetal bovine serum and 1% penicillin−streptomycin solution (100×) in a humidified incubator at 37 °C, 5% CO2 [43]. For harvesting, media was removed and cells were washed once with PBS and incubated with a trypsinization reagent for 5 minutes at 37^{o}C. Reaction was neutralized with PBS/0.5% BSA once cells were detached. Medium was added and cells were transferred to a falcon tube, centrifuged and resuspended in HEPES buffer [23].

2.7. Instrumentation

Morphological characterization of gold nanoshpheres, nanocubes and SERS substrates was carried out with a JEOL JSM-7800F field-emission scanning electron microscope. UV-Vis absorption spectra of nanoparticles were recorded in the wavelength range of 400 to 800 nm with a UV-Visible spectrophotometer (Hach, DR 5000). Size distribution of nanoparticles was determined by image analysis using the public domain software ImageJ 1.48. Raman and SERS spectra were acquired with an InVia Raman spectrometer (Renishaw). A 50X objective was used for sample focusing and signal collection. Raman measurements were carried out with a laser excitation of 830nm and a 1200 lines/mm grating. Raman spectra were analyzed with Origin Pro 8.5.

3.Results

3.1.Characterization of colloidal nanoparticles

Gold nanospheres showed an average size of 19±2 nm and λ_{max} =523 nm (Fig.1A). Nanocubes (Fig. 1B), exhibit a characteristic concave shape with square depression in each face. Nanocubes have sharp corners and average edge length of 54±8 nm. λ_{max}=644 nm.

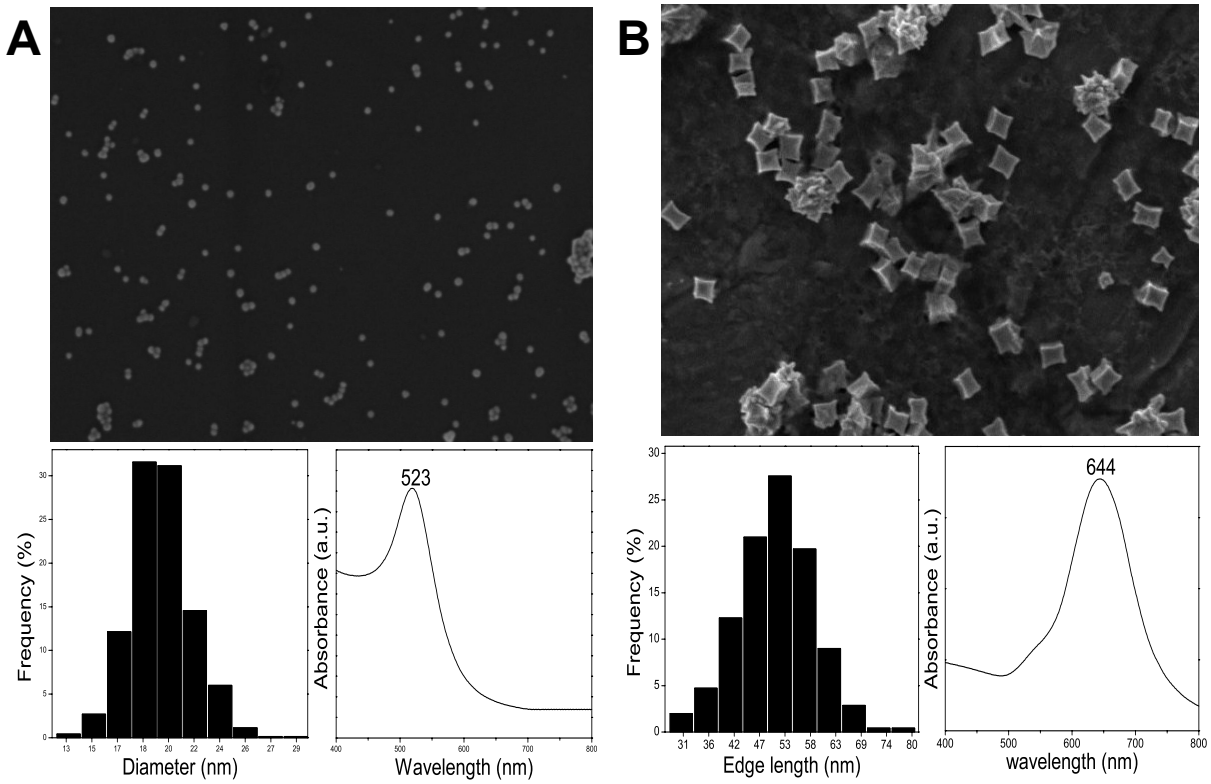

Figure 1. Characterization of A) colloidal gold nanospheres and B) Concave gold nanocubes.

3.2.Assembly and characterization of substrates

The layer-by-layer assembly of nanoparticles using bifunctional linkers provided good nanoparticle coverage on the GNSS (Fig. 2A). Most nanoparticles were packed close together without being completely aggregated.

For the GNCS, nanocubes were immobilized over a GNSS. SEM images (Fig. 2B) show a high coverage of both nanospheres and nanocubes. The arrangement of nanocubes on the substrate is mostly face-to-face and face to corner. Further characterization of the optical properties of the substrates is still being carried out.

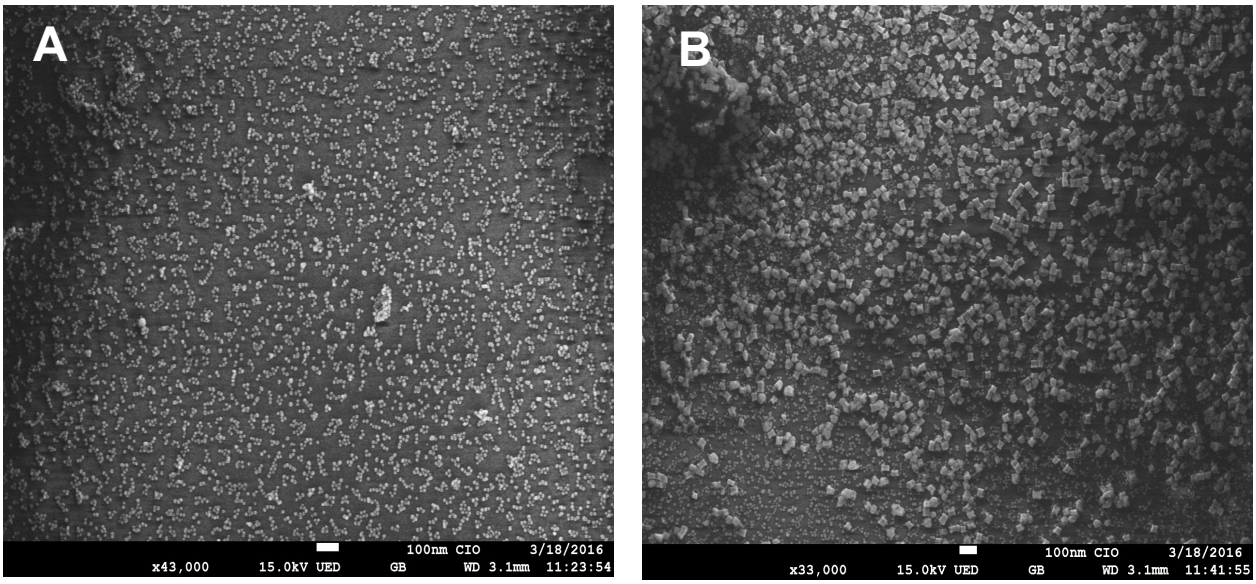

Figure 2. SEM micrograph of A) gold nanosphere substrate (GNSS) and B) gold nanocube substrate (GNCS).

3.4.SERS analysis of HeLa cells

The normal Raman spectra of cells were obtained by depositing cells on a glass microscope slide. For SERS measurements, substrates were allowed to air dry at room temperature before adding an aliquot of HeLa cells and analyzed without further preparation. Spectra of HeLa cells on GNCS, GNSS and normal Raman is shown in figure 3A. Particularly high enhancements were observed with GNCS in comparison to the GNSS and normal Raman. A magnification of the latter spectra is shown in Fig. 3B, where it can be noted that bands at ~848,1002 and 1235 cm^{-1} are also enhanced with the GNSS, with significantly lower intensities and slight shifts in position. The strong signal enhancements obtained with the GNCS can be attributed to the particular shape of the nanocubes. It is known that nanoparticles with pronounced corners have strong local field enhancement in the tips and edges [24], [25]. In addition, particle aggregation can generate a higher average SERS intensities due to the presence of hot spots [26], [27] . As observed by electron microscopy, nanocubes were slightly clustered (Fig. 2B). Normal Raman analysis of HeLa cells has been achieved by some research groups when carried out with *in-house* built equipment and specific conditions [28]–[30]. Still, it has been noted that normal and non-resonant Raman scattering from the analytes present in tissues and cells tend to be very weak and unreliable and might not be strong enough to discriminate biological molecules that share the same building blocks [31].

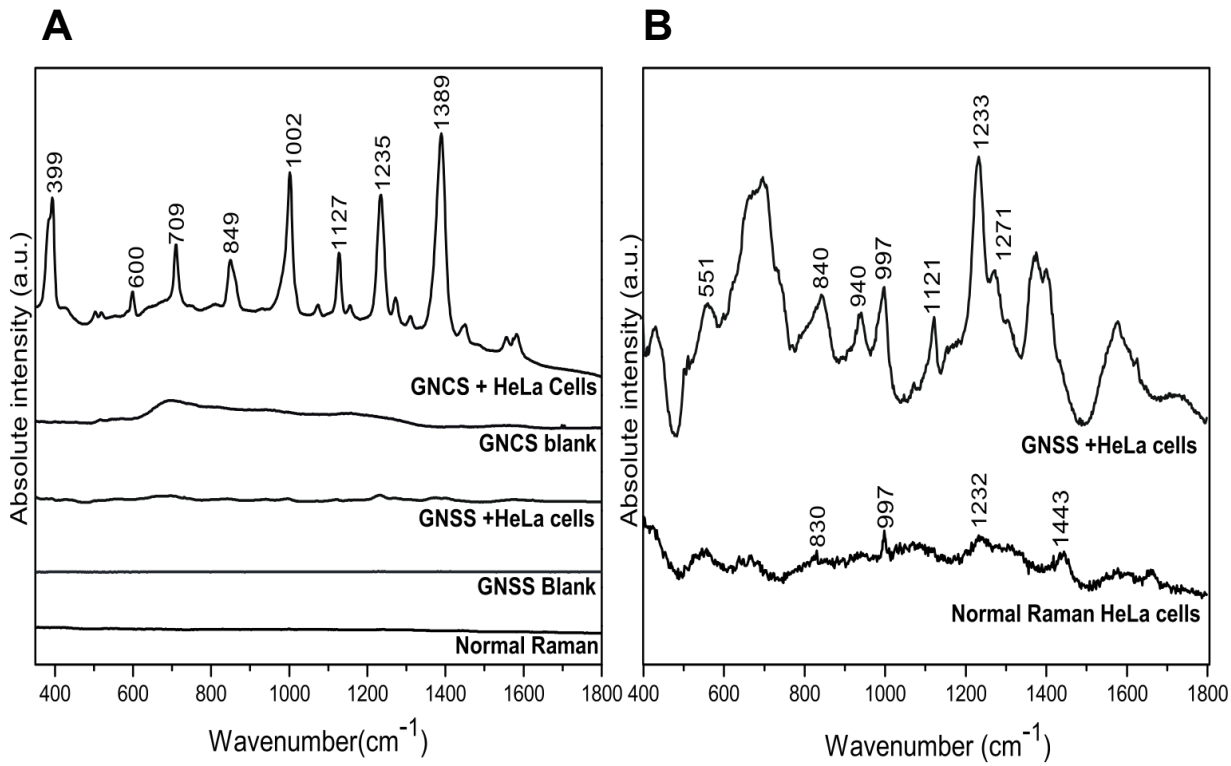

Figure 3. A) Comparison between SERS enhancement of HeLa cells obtained with GNCS, GNSS and Normal Raman. B) Magnification of the spectra enhanced by GNSS and normal Raman.

Tentative assignments are presented in table 1. Most of the bands are associated to proteins, amino acids residues and lipids. The SERS spectra of HeLa cells obtained with the GNCS provided rich information about the cell composition, by enhancing multiple bands in in the fingerprinting region of cells. The presence of an amide III band indicates the occurrence of a β-sheet or α-helix protein structure. Furthermore, the occurrence of strong amide functional groups suggests there is no protein denaturation. Signals corresponding to the amide III bands have helped differentiate between different cancer cell lines [12]. Moreover, the region from 1431cm^{-1} to 1481 cm^{-1} has been acknowledged as a marker band that represent the integral protein distribution in the cell [29]. The strongest band in the spectra was at 1389 cm^{-1} and can be assigned to the stretch of a carboxylate group in proteins and lipids [32].

Table 1. Tentative assignment of representative SERS bands of HeLa cells obtained with GNCS and GNSS.

SERS(cm^{-1})		Assignment	Biological molecules
GNCS	**GNSS**		
399	424	In-plane bending of aromatic C-OH bond	Aromatic aminoacids
709		C-N stretching, C-H twist+ring twist	Nucleic acids, lipids
849	840	Ring breathing,C-C stretch	Nucleic acids, lipids
1002	997	C-H in-plane deformation, ring breathing	Phenylalanine
1127	1121	C-N stretch,C-H bend ,C-C stretch	Proteins
1235	1233	Asymmetric stretching of P=O,C-H bend C-C stretch, amide III band	Nucleic acids, lipids, proteins
1273	1271	Amide III band	Proteins (α-helix structure)
1389	1399	CH_3, C-H stretch,COO- symmetric stretch	Lipids, proteins

4.Conclusions

A solid SERS active substrate formed by 3 layers of gold nanospheres and a final layer of gold nanocubes (GNCS) was studied for the label-free SERS analysis of a biological matrix (HeLa Cells). Significant enhancements in the SERS spectra were observed, and bands with very high resolution obtained, similar to those reported using substrates fabricated with more complex methods. The GNCS is non-specific, sample preparation time is minimal and fabrication by a solution based self assembly is relatively inexpensive.

It was demonstrated that a substrate fabricated by a self-assembly method generates high enhancement of bands associated protein primary and secondary structure, as well as other important marker bands and could help the qualitative analysis of important biological tissues. Since the substrates are glass based, biological samples can be immobilized, smeared or anchored if necessary. This substrate is promising for single cell analysis due to the amount of Raman bands enhanced, allowing biomolecule identification.

References

[1] M. Baranska, Ed., Optical Spectroscopy and Computational Methods in Biology. Springer, 2014.

[2] J. C. Merlin, “Resonance Raman spectroscopy of carotenoids and carotenoid-containing systems,” Pure Appl. Chem., vol. 57, no. 5, pp. 785–792, 1985.

[3] W. R. Premasiri, J. C. Lee, and L. D. Ziegler, “Surface-Enhanced Raman Scattering of Whole Human Blood, Blood Plasma, and Red Blood Cells: Cellular Processes and Bioanalytical Sensing.,” J. Phys. Chem. B, vol. 116, no. 31, pp. 9376–9386, 2012.

[4] A. Jaworska, T. Wojcik, K. Malek, U. Kwolek, M. Kepczynski, A. a. Ansary, S. Chlopicki, and M. Baranska, “Rhodamine 6G conjugated to gold nanoparticles as labels for both SERS and fluorescence studies on live endothelial cells,” Microchim. Acta, vol. 182, no. 1–2, pp. 119–127, 2014.

[5] K. Kneipp, A. S. Haka, H. Kneipp, K. Badizadegan, N. Yoshizawa, C. Boone, K. E. Shafer-Peltier, J. T. Motz, R. R. Dasari, and M. S. Feld, “Surface-Enhanced Raman Spectroscopy in Single Living Cells Using Gold Nanoparticles,” Appl. Spectrosc., vol. 56, no. 2, pp. 150–154, 2002.

[6] Q. Zhang, N. Large, and H. Wang, “Gold nanoparticles with tipped surface structures as substrates for single-particle surface-enhanced raman spectroscopy: Concave nanocubes, nanotrisoctahedra, and nanostars,” ACS Appl. Mater. Interfaces, vol. 6, no. 19, pp. 17255–17267, 2014.

[7] J. M. Romo-Herrera, A. L. González, L. Guerrini, F. R. Castiello, G. Alonso-Nuñez, O. E. Contreras, and R. A. Alvarez-Puebla, “A study of the depth and size of concave cube Au nanoparticles as highly sensitive SERS probes,” Nanoscale, vol. 8, no. 13, pp. 7326–7333, 2016.

[8] P. Matteini, M. de Angelis, L. Ulivi, S. Centi, and R. Pini, “Concave gold nanocube assemblies as nanotraps for surface-enhanced Raman scattering-based detection of proteins,” Nanoscale, vol. 7, no. 8, pp. 3474–3480, 2015.

[9] M. Li, D. P. Canniffe, P. J. Jackson, P. a Davison, S. FitzGerald, M. J. Dickman, J. G. Burgess, C. N. Hunter, and W. E. Huang, “Rapid resonance Raman microspectroscopy to probe carbon dioxide fixation by single cells in microbial communities.,” ISME J., vol. 6, no. 4, pp. 875–85, Apr. 2012.

[10] J. P. Nolan, E. Duggan, E. Liu, D. Condello, I. Dave, and S. a Stoner, “Single cell analysis using surface enhanced Raman scattering (SERS) tags.,” Methods, vol. 57, no. 3, pp. 272–9, Jul. 2012.

[11] Y.-L. Deng and Y.-J. Juang, “Black silicon SERS substrate: effect of surface morphology on SERS detection and application of single algal cell analysis.,” Biosens. Bioelectron., vol. 53, pp. 37–42, Mar. 2014.

[12] W. A. El-Said, T.-H. Kim, H. Kim, and J.-W. Choi, “Detection of effect of chemotherapeutic agents to cancer cells on gold nanoflower patterned substrate using surface-enhanced Raman scattering and cyclic voltammetry.,” Biosens. Bioelectron., vol. 26, no. 4, pp. 1486–92, Dec. 2010.

[13] G. Kuku, M. Saricam, F. Akhatova, A. Danilushkina, and R. Fakhrullin, “Surface-Enhanced Raman Scattering to evaluate nanomaterial cytotoxicity on living cells,” Anal. Chem., vol. 88, pp. 9813–9820, 2016.

[14] M. M. Martinez-Garcia, P. E. Cardoso-Avila, and J. L. Pichardo-Molina, “Concave gold nanocubes on Al-6063 alloy as a simple and efficient SERS

substrate," Asp. Colloids Surfaces A Physicochem. Eng. Asp., vol. 493, no. 493, pp. 66–73, 2016.
[15] W. Cai, X. Wang, and Y. Yan, "Controllable fabrication and sensitive detection based on SERS substrates with Au nanocubes coated Fe3O4," Mater. Res. Bull., vol. 52, pp. 1–5, Apr. 2014.
[16] S. J. Ding and J. Zhu, "Tuning the surface enhanced Raman scattering activity of gold nanocubes by silver coating," Appl. Surf. Sci., vol. 357, pp. 487–492, 2015.
[17] W. A. El-Said, T.-H. Kim, H. Kim, and J.-W. Choi, "Analysis of intracellular state based on controlled 3D nanostructures mediated surface enhanced Raman scattering.," PLoS One, vol. 6, no. 2, p. e15836, Jan. 2011.
[18] C. J. Addison and A. G. Brolo, "Nanoparticle-containing structures as a substrate for surface-enhanced Raman scattering.," Langmuir, vol. 22, no. 21, pp. 8696–702, Oct. 2006.
[19] K. C. Grabar, R. G. Freeman, M. B. Hommer, and M. J. Natan, "Preparation and Characterization of Au Colloid Monolayers," Anal. Chem., vol. 67, no. 4, pp. 735–743, 1995.
[20] P. G. Martínez-Torres, M. M. Martínez-García, P. E. Cardoso-Ávila, and J. L. Pichardo-Molina, "Facile Nanostructured Substrate Preparation Using Gold Nanocuboids for SERS," Nanomater. Nanotechnol., vol. 5, no. 12, p. 1, 2015.
[21] M. Y. Tsvetkov, B. N. Khlebtsov, V. a Khanadeev, V. N. Bagratashvili, P. S. Timashev, M. I. Samoylovich, and N. G. Khlebtsov, "SERS substrates formed by gold nanorods deposited on colloidal silica films.," Nanoscale Res. Lett., vol. 8, no. 1, p. 250, Jan. 2013.
[22] T. Wang and X. Jiang, "Size-dependent stability of water-solubilized CdTe quantum dots and their uptake mechanism by live HeLa cells.," ACS Appl. Mater. Interfaces, vol. 5, no. 4, pp. 1190–6, Feb. 2013.
[23] A. F. Palonpon, M. Sodeoka, and K. Fujita, "Molecular imaging of live cells by Raman microscopy.," Curr. Opin. Chem. Biol., vol. 17, no. 4, pp. 708–15, Aug. 2013.
[24] J. Zhang, M. R. Langille, M. L. Personick, K. Zhang, S. Li, and C. a. Mirkin, "Concave cubic gold nanocrystals with high-index facets," J. Am. Chem. Soc., vol. 132, no. 40, pp. 14012–14014, 2010.
[25] D. Lee and S. Yoon, "Gold nanocube-nanosphere dimers: Preparation, plasmon coupling, and surface-enhanced raman scattering," J. Phys. Chem. C, vol. 119, no. 14, pp. 7873–7882, 2015.
[26] C. P. Shaw, M. Fan, C. Lane, G. Barry, A. I. Jirasek, and A. G. Brolo, "Statistical Correlation Between SERS Intensity and Nanoparticle Cluster Size," J. Phys. Chem. C, vol. 117, no. 32, pp. 16596–16605, Aug. 2013.
[27] J. Zhu, J. Zhou, J. Guo, W. Cai, B. Liu, Z. Wang, and Z. Sun, "Surface-enhanced Raman spectroscopy investigation on human breast cancer cells.," Chem. Cent. J., vol. 7, no. 1, p. 37, Jan. 2013.
[28] H. Van Manen, A. Lenferink, and C. Otto, "Noninvasive Imaging of Protein Metabolic Labeling in Single Human Cells Using Stable Isotopes and Raman Microscopy," Anal. Chem., vol. 80, no. 24, pp. 9576–9582, 2008.
[29] N. Uzunbajakava, a Lenferink, Y. Kraan, B. Willekens, G. Vrensen, J. Greve, and C. Otto, "Nonresonant Raman imaging of protein distribution in single human cells.," Biopolymers, vol. 72, no. 1, pp. 1–9, Jan. 2003.

[30] M. Okada, N. Isaac, A. Flotildes, H. Endo, and S. Kawata, “Label-free Raman observation of cytochrome c dynamics during apoptosis,” PNAS, vol. 109, no. 1, pp. 28–32, 2012.
[31] J. P. Scaffidi, M. K. Gregas, V. Seewaldt, and T. Vo-Dinh, “SERS-based plasmonic nanobiosensing in single living cells.,” Anal. Bioanal. Chem., vol. 393, no. 4, pp. 1135–41, Mar. 2009.
[32] E. Podstawka, Y. Ozaki, and L. M. Proniewicz, “Adsorption of S-S containing proteins on a colloidal silver surface studied by surface-enhanced Raman spectroscopy.,” Appl. Spectrosc., vol. 58, no. 10, pp. 1147–56, Oct. 2004.

Chapter 6
Characterization of cellular systems

Spectroscopic Characterization of Radiosensitive (LY-S) and Radioresistant (LY-R) Murine Leukemia Sublines by Raman and Surface Enhanced Raman Spectroscopy (SERS)

Chapter 6

Spectroscopic Characterization of Radiosensitive (LY-S) and Radioresistant (LY-R) Murine Leukemia Sublines by Raman and Surface Enhanced Raman Spectroscopy (SERS)

1.Introduction

Around 40-50% of diagnosed cancer patients are treated with radiation therapy [1]. Radiation response varies widely amongst individual cases, and the course of action is usually determined based on the histopathological and anatomical characteristics of the tumor. Nonetheless, several biological mechanisms like repopulation capacity, tumor microenvironment [2] and intrinsic radiation sensitivity [3] have been shown to affect the therapeutic response of a tumor [4]. According to Begg et al.[3], studying the differences between normal and malignant tissues amongst individual patients is key to improve radiotherapy outcomes.

Predictive assays could potentially be used for the rapid evaluation of intrinsic radiosensitivity of some tumors [5], [6]. Intrinsic radiosensitivity can be hereditary, and depend on the tissue origin and acquired mutations [7]. Intrinsic radiation sensitivity has been predominantly determined by a clonogenic survival assay (SF2) [4], [8]. One of the main drawbacks of this technique is time consuming and difficult nature of the method [9]. Some efforts have focused on genetic and molecular biology techniques to detect differences in gene expression [7] but are still underway. It has been noted that the failure to predict radiation outcomes can be related to the minimal manifestation of quantitative differences between tumors and normal tissue, and wide tissue heterogeneity [5].

Raman spectroscopy is a promising tool for the fast analysis and classification of tissues. A high-throughput and label-free vibrational spectroscopy technique like Raman spectroscopy provides information about the chemical composition of cells, tissues and fluids that result in a specific “fingerprint” constituted by the spectra of different molecular components [10] (e.g., proteins, lipids and nucleic acids). Biochemical changes caused by a disease can translate to changes in the Raman spectra [11]. Spontaneous or normal Raman scattering can be limited by low analyte concentration and instrumental parameters. Surface Enhanced Raman Spectroscopy (SERS) is a technique that allows the amplification of the Raman signal by means of metallic nanomaterials [12].

Raman spectroscopy and SERS are routinely combined with multivariate analysis algorithms like PCA, LDA, SVM and random forest [10], [13]–[16], where the ability to differentiate between cell samples based on small changes has been demonstrated. Special interest has been made in the analysis of cancerous cells, cell lines and tumors [17]–[20]. Analysis of chemoresistant cells [21], discrimination between lymphoma samples [22],

and changes caused by doses of ionizing radiation have been studied [23]–[25]. In one of the few studies analyzing radiosensitivity by Raman spectroscopy, Yasser et al., [26] studied the acquired radioresistance of oral cancer sublines and observed changes in the bands associated to DNA and proteins.

In this work, cells from two established lymphoma sublines known for their intrinsic radioresistance (LY-R) and radiosensitivity (LY-S) were analyzed by Raman spectroscopy. The L5178Y (LY) Murine lymphoma cell line was derived from an induced thymic tumor. The parent line (LY-R) is resistant to ionizing radiation, and highly tumorigenic in DBA/2 mice [27], [28]. The LY-S subline is sensitive to ionizing radiation. In addition to their different radiation sensitivity, the LY-S and LY-R cells present different responses to external physicochemical agents [27]; the LY-R subline is radiation resistant but more sensitive to UV-C radiation and hydrogen peroxide [28]. To the best of our knowledge, no previous study has addressed the characterization of the LY-S and LY-R sublines by vibration spectroscopy techniques. Therefore, a complete normal Raman characterization of both sublines was carried out using different excitation wavelengths. In addition, Surface Enhanced Raman Spectroscopy (SERS) using gold nanoparticles (AuNPs) and silver nanoparticles (AgNPs) was carried out. Principal component analysis (PCA) was used to discriminate the spectral signatures of both sublines. In line with other recent work, this study represents an initial approach to help understand the intrinsic spectroscopic characteristics of radiosensitive and radioresistant cells, in order to contribute to the development of radiosensitivity predictive assays.

2.Experimental details

2.1. Reagents

Silver nitrate ($AgNO_3$, 99%), sodium borohydride ($NaBH_4$, 99%), Gold (III) chloride solution ($HAuCl_4$, 99%, 30 wt. % in dilute HCl), trisodium citrate dihydrate (99%), and formaldehyde 37 wt. % were acquired from Sigma–Aldrich (Sigma-Aldrich, USA). Glutaraldehyde 25 wt. % was purchased from Merck (Merck, Germany). Reagents were used without further purification. Water used for washing material and preparation of aqueous solutions was ultrapure (Resistivity> 18.2MΩ cm), purified with a MQ system (Millipore Corp., USA).

2.2. Cell culture

L5178Y-R (ATCC® CRL-1722TM) and L5178Y-S (ATCC®CRL-1723TM) cell lines were cultured in RPMI 1640 medium containing L-Glutamine (Sigma-Aldrich, Missouri, USA) supplemented with 10% Fetal Bovine Serum heat-inactivated (Gibco, Massachusetts, USA), 10 units/ml penicillin and 100 mg/ml streptomycin (Sigma-Aldrich, Missouri, USA). Cells were incubated at 37°C in 5% CO2 until a density about 1 x 106 cells/ml was achieved. Cells were then collected from the flasks, centrifuged at 1,000 rpm for 5 minutes and resuspended to the original volume in 1X PBS. A 10-ml sample of cell suspension was employed for the characterization by Raman spectroscopy.

2.3.Nanoparticle synthesis and characterization

Silver nanoparticle (AgNPs) were synthesized by a modified Creighton method [29] . 10 mL of NaNO3 (3.5mM) were added dropwise to 30 mL of a freshly prepared NaBH4 solution (7mM), under continuous stirring and placed in an ice bath. After 3 minutes, stirring was stopped and the solution was left undisturbed for 45 minutes. Subsequently, the solution was diluted in a 1:1 ratio with deionized water. The colloidal solution was stored in darkness until further use.

Gold nanoparticles were synthesized by the Frens method [30] of gold citrate reduction with slight modifications. 2 mL of HAuCl4 (28.9 mM) were added to 125 mL of deionized water, vigorously stirred and brought to a rolling boil, followed by 10 mL of a 6 mM sodium citrate solution. The solution was removed from heat, and stirring continued for 15 minutes. The colloidal solution was left to stabilize for 3 days and kept in darkness.

UV-Vis absorption spectra of AgNPs and AuNPs were acquired with a Hach DR 5000 UV-Vis spectrophotometer (Hach, USA) in the range of 300 to 700 nm.

2.4. Normal Raman measurements

2 mL of either LY-R or LY-S cell suspension were centrifuged at 1000 rpm for 3 minutes. The supernatant was removed, and 2mL of fresh PBS buffer were added. 10 µL of cell suspension in PBS buffer were deposited on a clean quartz substrate (Ted Pella, USA). Raman spectra were acquired with an InVia Raman microscope (Renishaw, UK). A 50x lens was used to focus onto the sample. Measurements were centered at 1500 cm^{-1}, with 1 s exposure and 3 acquisitions, in order to avoid cell damage. Cells were characterized

using four different excitation wavelengths (457, 514, 633 and 830 nm). Grating was 1200 l/mm for the 633nm and 830 nm lasers, and 2400 l/mm for the 457 and 514 nm lasers. Laser excitation was ~9mW for 457 nm, ~17 mW for 514nm, ~17mW for 633nm and ~10mW for 830 nm. 30 cells were probed for each subline and excitation wavelength.

2.5. SERS measurements

100 microliters of either AgNPs or AuNPs colloid were added to 370 µL of cell suspension in PBS (See section 2.4), and 130 µL of PBS buffer. The mixture was gently mixed and incubated for 1 hour. After incubation, cells were washed by centrifugation for 3 min at 1000 rpm. The supernatant was carefully removed, leaving a concentrated cell pellet. 10 µL of cell pellet were placed on a quartz substrate.

SERS enhancement can be highly variable due to the presence of hotspots, and the random distribution of nanoparticles in the cell [31], therefore, Raman spectra were acquired in a mapping mode, where at least 30 points were measured, to obtain more homogeneous, representative spectra.

SERS spectra with AgNPs were obtained with a 633 nm excitation wavelength, centered at 1500 cm^{-1} with ~1mW power. For AuNPs, 830 nm excitation was used, and measurement was centered at 1250cm^{-1}, ~1mW laser power. 10 different pellets for each subline, and nanoparticle type were analyzed. Control spectra consisting of the normal Raman spectra of cells (without nanoparticles) measured under the same instrumental conditions used for SERS were also acquired.

2.6. Electron microscopy

Cells incubated with nanoparticles were centrifuged (1000 rpm, 3 min) and the supernatant was removed. Cells were fixed with a 3% glutaraldehyde 3 % formaldehyde solution for 2 h at room temperature [32]. Afterward, the solution was carefully removed to avoid resuspending the cell pellet. Cells were dehydrated following a graded series of ethanol solutions in deionized water, with 10 min incubation for each step. Finally, cells on 100% ethanol were stored at 4^{o}C.

Cell morphology and the presence of nanoparticles in the cell surface were studied by High resolution Scanning Electronic Microscopy using a field-emission gun Hitachi S-5500 microscope (Hitachi, Japan) equipped with a BF/ADF detector.

2.7. Principal Component Analysis

Raman spectra were baseline corrected by a 5th order polynomial fitting using WiRE 4 software (Reinishaw, UK), and averaged with OriginPro 8.5 (OriginLab, USA). Principal component analysis was carried out with the Unscrambler X version 10.1 (CAMO Software A.S., Norway). For normal Raman, 30 measurements for each subline (LY-R and LY-S) measured with the excitation wavelengths that rendered the highest amount of Raman bands and better signal-to-noise ratio (514nm and 633nm) were input into the software. In the case of SERS measurements, the average spectra of 10 cell pellets for each subline (LY-R and LY-S), and nanoparticle type (AgNPs and AuNPs) were analyzed.

3. Results and discussions

3.1. Normal Raman measurements

No prior characterization of the LY-R or LY-S sublines has been reported. Thus, a range of excitation wavelengths were explored to find the experimental conditions that render the most information-rich spectra [33]. The mean spectra (30 measurements) of the radioresistant (LY-R) and radiosensitive (LY-S) sublines obtained with 457, 514, 633 and 830 nm wavelengths are presented in Fig. 1.

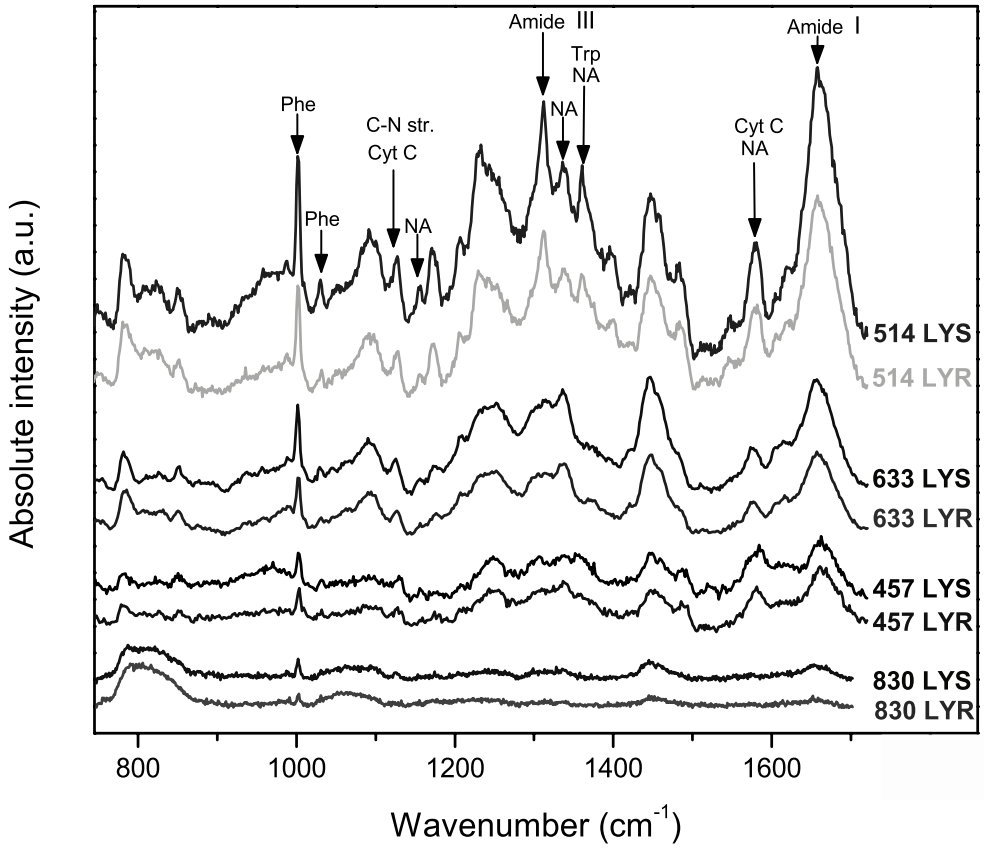

Figure 1. Normal Raman spectra of LYR and LYS cells obtained with different excitation wavelengths (average of 30 measurements). Cyt c: cytochrome c, Phe: phenylalanine , Trp: tryptophan, NA: nucleic acids.

An 830 nm excitation wavelength is generally recommended for biological samples since it can be less damaging to tissues [57] and help reduce cell autofluorescence [58]. Nevertheless, as observed in Fig. 1, the lowest signals were observed with 830 nm. Raman scattering efficiency is proportional to λ^4, where λ is the wavelength, assuming non-resonant excitation[53]. Therefore, shorter wavelengths (e.g. 457 nm, 514 nm) generate better scattering efficiencies than wavelengths approaching the infrared region (e.g., 785, 830 nm). In addition, the higher laser power needed to compensate for the low

scattering efficiency can damage the cell, and although cell autofluorescence can be reduced with longer wavelengths, fluorescence from the substrate and the objective can cause interference [59]. In contrast, a 457 nm wavelength is expected to exhibit better scattering efficiencies, but shorter wavelengths can cause photochemical damage to biological tissues and DNA [60,61]. High scattering efficiencies induce sample autofluorescence but also resonance of some molecules, which can be advantageous; heme moieties and cytochrome c can be excited with 488, 514 and 568 wavelengths [62]. The spectra acquired with 514nm (Fig. 1) presented the bands with the highest intensity. These bands are not as defined with 633nm, probably due to the lack of a resonance effect for certain molecules with aromatic rings in their structure.
The balance between high excitation efficiencies and low sample damage has been demonstrated to lie between 532 and 758 nm [63]. With good scattering efficiency, and despite cell autofluorescence, 514 and 633nm present a good choice for the analysis of LY-R and LY-S cells.

The most prominent feature observed with all excitation wavelengths emerges from the phenylalanine symmetric ring breathing at ~1002 cm^{-1} (Fig.1). Notably, this band is consistently more intense for LY-S cells with all excitation lasers. Another phenylalanine band is observed at ~1030 cm^{-1} and is assigned to C-H stretching vibrations. The band ~1097 cm^{-1} corresponds symmetric stretching of the phosphate DNA backbone [64]. Other bands that exhibited different intensities in LY-R and LY-S cells are those assigned to cytochrome c (~1127 cm^{-1}), nucleic acids (~1150 and 1360 cm^{-1}, and amide III (~ 1312 cm^{-1}). Tentative assignment of main Raman bands is presented in table 1.Bands at 751, 1131 and 1312 cm^{-1}, assigned to different vibrational modes of cytochrome c have been observed when excited with a 532 nm laser [61],[65],[66], thus under resonance scattering conditions. This is in agreement with our observations for LY-R and LY-S cells, since the band at ~ 751 cm^{-1} only arises with 455 and 514 nm excitation. Porphyrins and pyrimidine rings can also exhibit resonance at 514 nm.

Hamada et al.[65] analyzed HeLa cells with 488, 514, 532 and 633 nm excitation, and found that a 633 nm laser provided a much lower scattering signal, and the bands at 1451 and 1660 cm^{-1} were the most prominent. These prominent and broad band, that correspond to CH_2CH_3 deformations and the amide I band, respectively, have been also reported for lymphocytes by Bankapur et al.[67]. In this work the CH_2CH_3 deformation band was observed between 1441 and 1448 cm^{-1}. The band arising at 1448 is also known as protein marker band, and is representative of the protein concentration in the cell [68], and has a slight higher intensity in the LY-S subline. The amide III bands have also been associated to changes in the overall protein content [69], and this band (~1312 cm^{-1}) is also more intense in LY-S cells. The band at 1543 cm^{-1} is attributed to amide II vibrations (60% NH bending, 40% CN str.). The amide I band is assigned to a combination of C=O stretching and N-H in plane bending [70].

Information concerning the spectral signature of lymphoblasts is scarce. The normal Raman spectra of LY-R and LY-S cells is dominated by bands

corresponding to proteins (Amide I, II, III) and nucleic acids (Table 1). This is expected since LY cells have a lymphoblast morphology, characterized for a high nuclear/cytoplasmic ratio [55] similar to lymphocytes, where the nucleus can constitute up to 80% of the total cell volume [22]. In addition, these cells are able to express multiple surface proteins [27], [56], [57].

Table 1. Raman band assignment for the average spectra of LY-R and LY-S cells with 457, 514, 633 and 830 nm excitation.

Raman shift (cm^{-1})								Assignment
457nm		514 nm		633 nm		830 nm		
LY-R	LY-S	LY-R	LY-S	LY-R	LY-S	LY-R	LY-S	
640	638			643	642			Tyr C-C twist [25], [44].[54], [55]
673	675							G, C-C str.
		723	725	725	725			A [25]
748	746	750	748					T, U [47], cyt c ring breathing mode [44]
778	784	781	781	785	781	805	805	U, T, C [25], O-P-O str. (DNA backbone) [47]
825	821		822					Tyr, O-P-O [25]
850	850	852	850	850	852			Tyr [54], out of plane ring breathing [44]
	970			957	956			C-C str. [25]
1002	1002	1002	1002	1001	1001	1002	1002	Phe sym. ring breathing, C-C str.[47],[48], [47], [56]
1031	1031	1031	1030	1031	1029			Phe C-H str. [25], [44][54], [55], [57]
						1056	1077	C-N, C-C str. [25]
1091	1091	1091	1090	1090	1090			O-P-O str. [22], PO_2^- DNA phosphate backbone [40],[50]
1128	1129	1127	1127	1126	1125	1121	1125	C-N str. [22], [51] in proteins, cyt c [41],[52][58], [59]
1155	1155	1155	1155	1155	1155			Nucleic acids, C-O str., C-N str, C-C str [43],[47] [56], [60], [61]
		1170	1170	1176	1173			Tyr, Phe, C-H bend [22], C, G [51]
							1203	Phe, Tyr, Trp
		1229	1233					Amide III (C-N str and N-H bending) [25],[51]
1246	1248			1252	1252	1241	1242	Amide III [25]
				1295	1294			CH_2 twist
1309	1306	1312	1312	1314	1314			Amide III [47], C-H deformation [22], CH_3, CH_2 twisting [51] Cyt c [41]
1337	1338	1326	1335	1335	1338	1335	1338	Nucleic acid mode indicating the nucleic acid content in tissues [51], CH_3, CH_2 torsion [47]
1355	1352	1360	1360					Nucleic acids [53], Trp [51].
1448	1448	1447	1447	1446	1441	1446	1441	CH_2CH_3 deformation [40] CH_2 scissoring and bending [51]
		1486	1483					Nucleic acids and DNA backbone[43], deoxyribose [43]
1543	1538				1544			Trp [54]
		1573	1578	1577	1573			Pyrimidin ring from nucleic acids and heme proteins [51] Nucleic acids (G,A) ring breathing [40], [47], Cyt c [41],[52] [58], [59]
				1615	1616			Tyr, Trp [25]
1662	1662	1658	1658	1656	1657			Amide I [40], [52], C=C str. of lipids [51]

Cyt c: cytochrome c, Phe: Phenylalanine, Tyr: Tyrosine, Trp: Tryptophan, A: Adenine, C: cytosine, G: guanine, U: uracil, T: thymine.

Visual inspection of Raman spectra is not sufficient to determine variations between sublines, as Raman spectra of biological matrixes are constituted by the signals arising from the different molecules present in the sample [54]. Principal component analysis was carried out for further exploration of the data. PCA score plots of the spectra obtained with the 633 and 514 nm lasers are shown in Fig. 2A and B, respectively. Spectra obtained 633 and 514 nm were selected since these spectra presented a higher quantity of prominent bands with high intensity, as seen in Fig. 1.

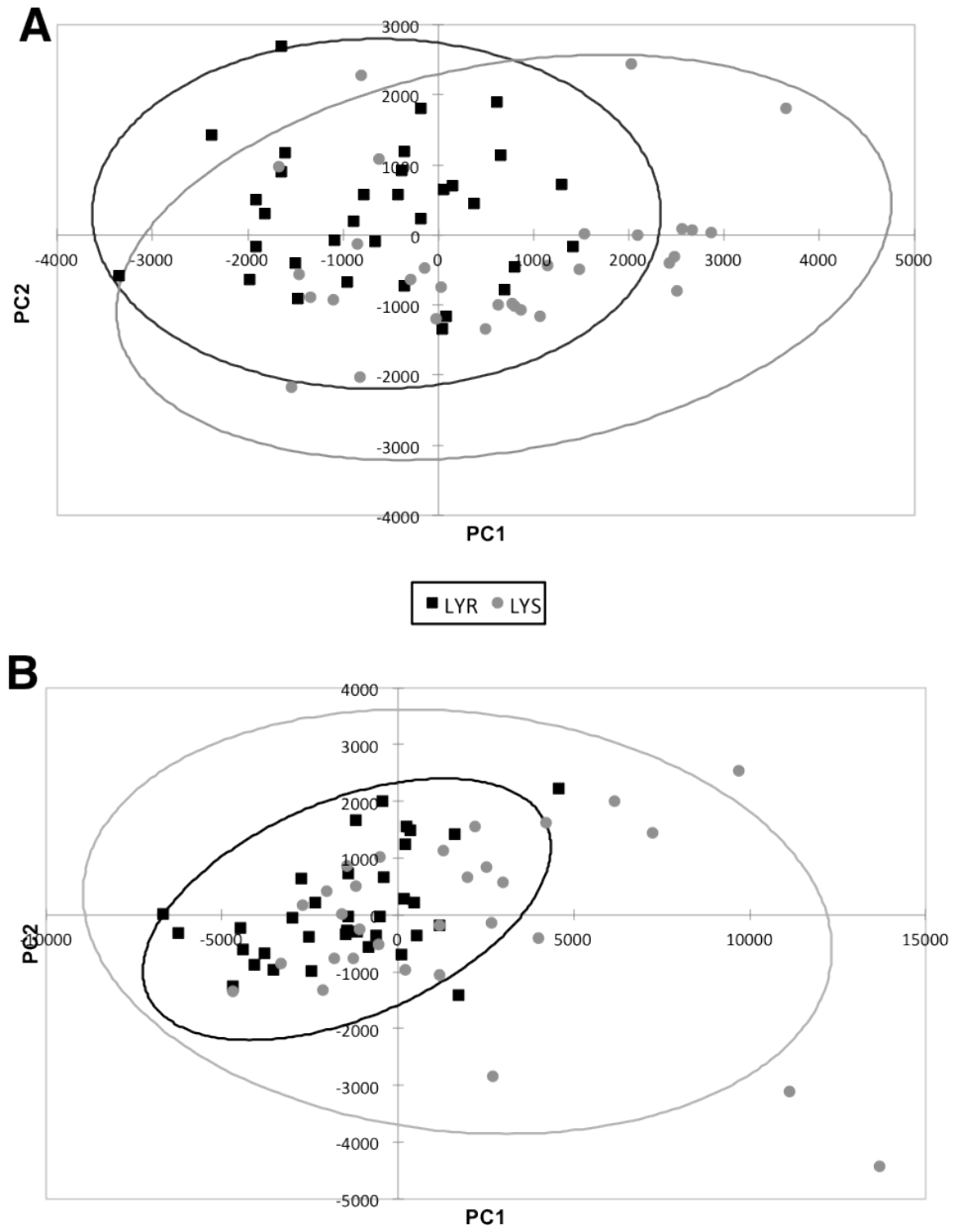

Figure 2. PCA score plots of A) cells measured using a 633 nm excitation laser, and B) cells measured with a 514 nm laser.

Data treatment by principal component analysis indicates that discrimination of LY-R and LY-S samples, based on the complete range of their Raman spectra, was not attained with this preliminary approach. In order to find a better resolution between sublines, future work will be focused on the exhaustive analysis of truncated sections of the spectra, for example the range between 1000 and 1150 cm^{-1}, that showed minor differences upon visual inspection of the mean normal Raman spectra.

3.2. Nanoparticle synthesis and characterization

Fig. 3 shows the absorption spectra of AuNPs and AgNPs. The λmax of AuNPs was 533 nm (Fig. 3A). According to data from literature, said absorption maxima corresponds to AuNPs of 54-59 nm diameter [30], [58], [59]. It has been reported that nanoparticles of sizes ~60 nm are known to generate higher enhancement than smaller diameters [31], [60]. Size distribution histograms will be calculated once TEM microscopy is carried out. The λmax of AgNPs was located at 394 nm (Fig. 3B), corresponding to a to diameters ~19 nm particle size. The modified Creighton method used herein is based on a comprehensive study carried out by our research group, where different parameters were explored in order to establish the synthesis conditions that generate the highest SERS enhancements. It was found that larger nanoparticles (~19 nm) with a slight degree of aggregation were the most suitable for SERS analysis [61].

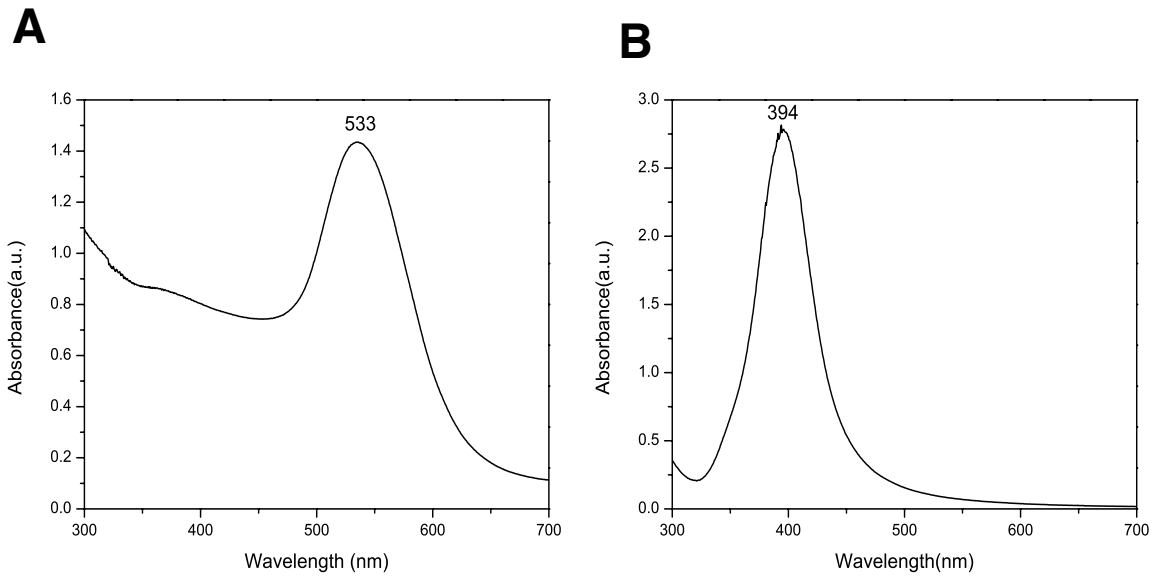

Figure 3. UV-Vis absorption spectra of A) AuNPs and B) AgNPs.

AuNPs synthesized by the Frens [30] method do not require additional stabilizer besides citrate ions. As well, in the case of AgNPs, excess $NaBH_4$ ions function as stabilizing agents. Synthesis methods requiring additional stabilizing agents like CTAB were avoided as interfering SERS signal from the stabilizer can arise. Most stabilizers can be easily removed once nanoparticles are immobilized in a substrate; however, nanoparticles were

required to be in colloidal solution to be used for cell incubation. Removal of stabilizer by centrifugation [31], [62] can cause loss of stability and aggregation.

3.3. SERS measurements

3.3.1. SERS analysis using AgNPs

SERS spectra of LY-R and LY-S cells incubated with AgNPs are presented in Fig. 4A. SERS spectra show small differences from the normal Raman spectra and between sublines. The spectral region between 600-800 cm^{-1} varies amongst LY-R and LY-S cells, with slightly higher signal intensities observed for LY-S cells. This region comprises the vibrational signature of nucleic acids and aromatic aminoacids (Table 1), suggesting that AgNPs can be in proximity to both proteins and nucleic acids. The amide I band is also higher in LY-S cells. LY-S are known to exhibit higher resistance to oxidant agents [28], and toxicity of AgNPs in cells is associated to the generation of reactive oxygen species (ROS)[63], [64]. Therefore, a higher enhancement with AgNPs could be related to the higher tolerance of LY-S to oxidative stress.

Preliminary data treatment by PCA (Fig. 4B) shows an overlap of confidence ellipses, and therefore a lack of discrimination between the sublines. Nonetheless, most of the data from LY-R cells is concentrated in the PC1 (-1500 to 0) quadrant, and further chemometric analysis using an algorithm like support vector machine (SVM) could feasibly achieve improved discrimination between sublines.

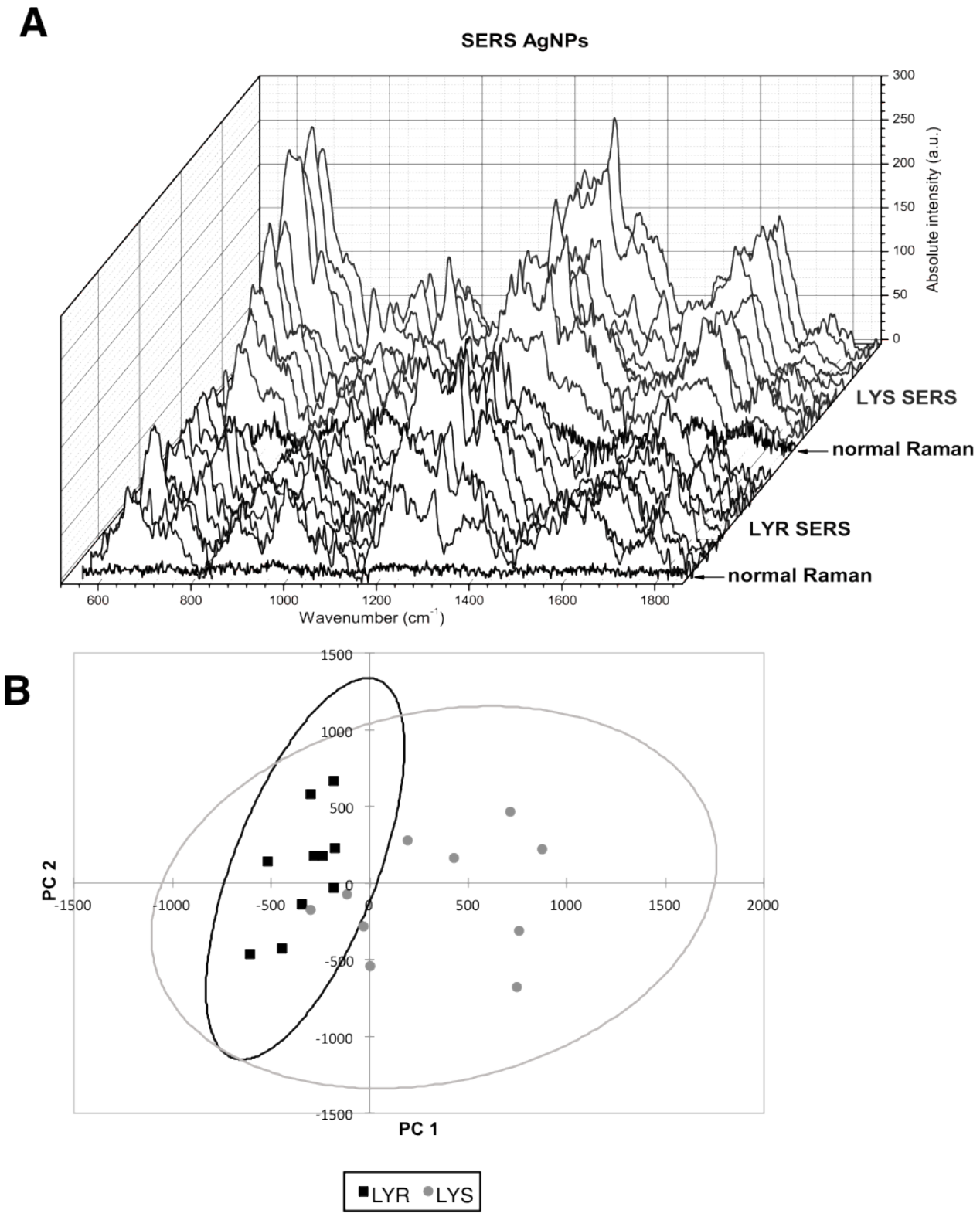

Figure 4. A) SERS spectra of cells incubated with AgNPs; 10 cell pellets were measured for the LY-S and LY-R subline. B) PCA score plots of cell of cells incubated with AgNPs (confidence interval of 95%).

3.3.2 SERS analysis using AuNPs

Fig. 5A shows the average spectra per cell pellet obtained using AuNPs, along with normal Raman spectra of each subline acquired with the same sampling conditions used for SERS. Under the same instrumental conditions, normal Raman spectra do not generate sufficient information when compared to the SERS spectra. Spectra obtained with AuNPs showed a notable difference between the LY-R and LY-S sublines, as can be evidently noticed by visual inspection of the spectral morphology. This was confirmed by PCA analysis; Fig. 5B shows a clear separation of the data corresponding to each subline. Along with higher SERS enhancements for LY-R cells, high spectral variability is observed, which translates into more disperse data in the PCA score plot. Given the known variability of SERS enhancements, pellets consisting of cell aggregates were analyzed in order to obtain more robust measurements. Cell concentration of the samples was 1 x 10^6 cells/ml, and 10 µL of cell pellet were deposited for each measurements, so ~6 000 cells are present in each pellet.

SERS enhancement can be affected by the presence of hotspots and aggregates, as well as the distribution of nanoparticles in the cell [12], [31], [65]. Even tough AgNPs tend generate higher enhancements than AuNPs, AuNPs have better biocompatibility [66]. Moreover, AuNPs clusters have been proven to exhibit similar enhancements than AgNPs when working with near infrared excitation [67], as was used in this work (830nm). Nonetheless, SERS allowed for a clear separation of both subline, especially when working with AuNPs.

Most bands enhanced in LY-R cells incubated with AuNPs are observed in the region between 1000 and 1500 cm^{-1}, arising mainly from proteins and nucleic acid (see table 1). SERS is a proximity effect, and the enhanced bands usually correspond to the molecules located in the vicinity of the metallic nanoparticles [67], so this could indicate an interaction of AuNPs with surface proteins, and also a degree of nanoparticle internalization. The band mostly enhanced in LY-S cells was the amide I band, possibly related to an interaction of AuNPs with surface proteins.

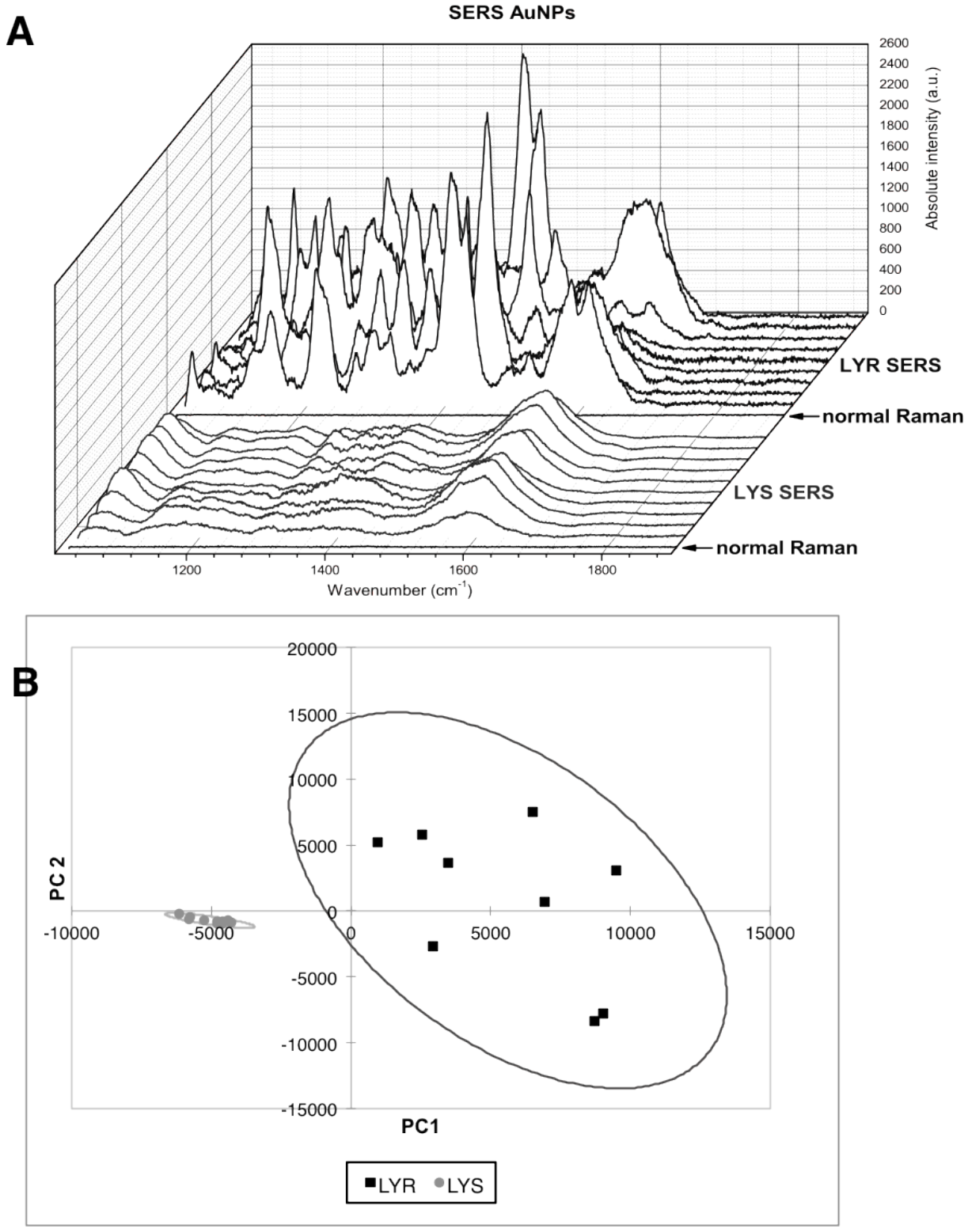

Figure 5. A) SERS spectra of cells incubated with AuNPs. B) PCA score plots of cells incubated with AuNPs. (confidence interval of 95%).

3.2.3. Cell interaction with metallic nanoparticles

Cells were incubated with colloidal nanoparticles in PBS buffer at physiological pH of 7.4. Surface charge (z-potential) of different cells like HeLa, MCF-7 and erythrocytes has been reported to be negative under physiological conditions (PBS buffer, pH 7.4)[68]. Both AgNPs and AuNPs are stabilized by negative ions, and tend to have a net negative charge at neutral pH[63], which can be modified to a net positive charge by lowering the pH of the solution. Future studies regarding z-potential are needed to elucidate the interaction between LY sublines and colloidal nanoparticles at neutral pH levels, since preliminary SERS observations show a possible selective interaction between metallic nanoparticles and LY-R and LY-S cells.

Differences in the electrophoretic pattern of LY-R and LY-S plasma membranes have been reported in initial studies of the sublines, and cells from the LY-S subline tend to form aggregates and exhibit higher osmotic fragility [27]. According to Szumiel [69], LY-R and LY-S present different ion transport, and nuclear matrix proteins.

3.4. Electron microscopy

Fig. 6 shows SEM micrographs of LY-R and LY-S cells incubated with AgNPs. For both sublines, nanoparticles were localized in the cell surface even after cell fixation steps. It is known that proteins with cysteine residues can potentially bind to metallic nanoparticles [63], and lymphoblast can present a variety of membrane proteins [70], [71].

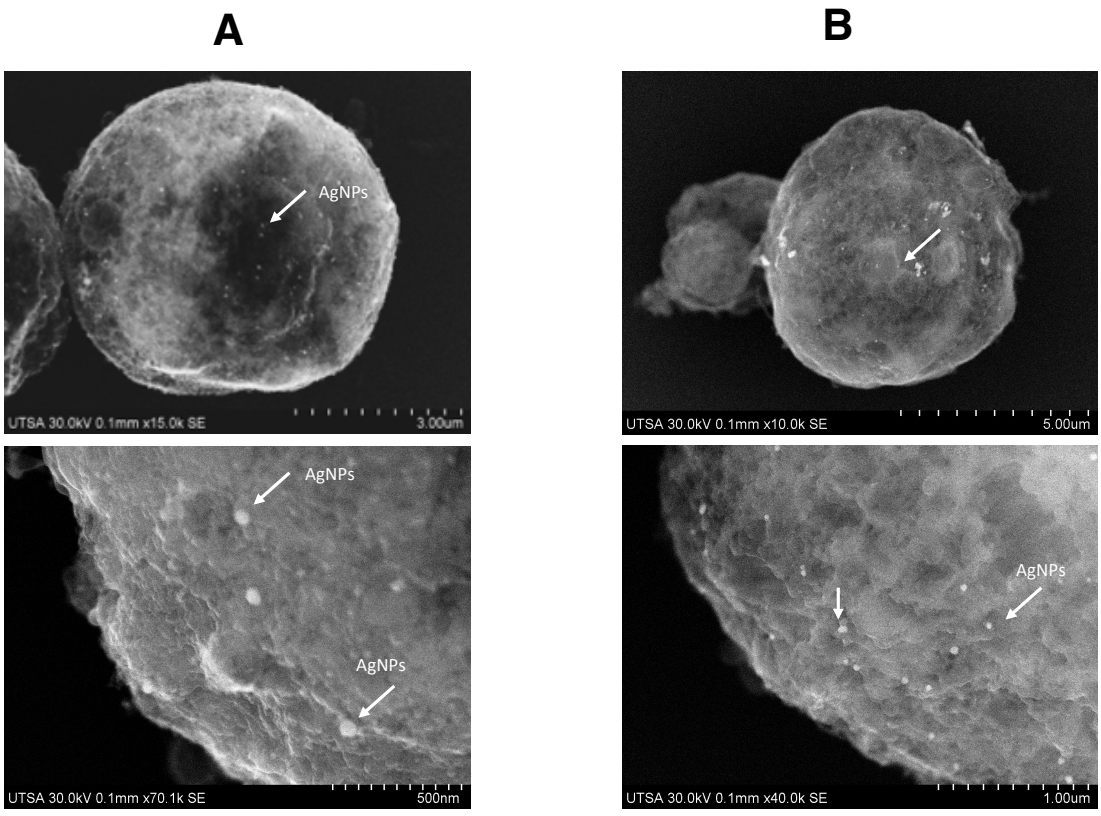

Figure 6. Scanning electron microscopy of A) LY-R and B) LY-S cells incubated with AgNPs.

Initial experiments showed that AgNPs rendered high SERS enhancements, so electron microscopy micrographs were obtained samples incubated solely with AgNPs. In an effort to expand the dataset, subsequent SERS measurements with AgNPs were carried out, and the initial high SERS enhancements were not attained. In an effort to obtain better SERS spectra, incubation with AuNPs was also tested. Since electron microscopy equipment is not widely available, SEM micrographs of cells incubated with AuNPs have not been acquired, but will be carried out in future work.

4. Conclusions

To the best of our knowledge, this is the first work exploring the vibrational spectroscopy characterization of the radioresistant (LY-R) and radiosensitive (LY-S) murine lymphoma sublines. Normal Raman analysis provided important information about chemical the constituents of both sublines, despite the lack of separation observed by preliminary principal component analysis (PCA). SERS was successfully used to enhance Raman spectra, and preliminary data treatment with PCA showed a clear separation between sublines incubated with AuNPs. Therefore, small biochemical differences can be identified based on changes in the spectral fingerprint. The development of predictive radiosensitivity assays based on tumor biochemistry and molecular biomarkers is still underway, but the biological parameters underlying the response to radiation can potentially be used in conjunction with established techniques to aid the selection of an adequate therapeutic treatment of cancer patients.

Future work will focus on the analysis of truncated spectral regions, as well the application of different chemometric techniques for the differentiation of both sublines. In addition, further studies are needed to evaluate possible differences in nanoparticle-cell interaction presented by the LY-R and LY-S sublines.

References

[1] A. Yaromina, M. Krause, and M. Baumann, “Individualization of cancer treatment from radiotherapy perspective,” vol. 6, 2012.

[2] N. von Moos and V. I. Slaveykova, “Oxidative stress induced by inorganic nanoparticles in bacteria and aquatic microalgae--state of the art and knowledge gaps.,” Nanotoxicology, vol. 8, no. 6, pp. 605–630, 2014.

[3] A. C. Begg, F. A. Stewart, and C. Vens, “Strategies to improve radiotherapy with targeted drugs,” Nat. Rev. Cancer, vol. 11, no. April, pp. 239–253, 2011.

[4] L. J. Forker, A. Choudhury, and A. E. Kiltie, “Biomarkers of Tumour Radiosensitivity and Predicting Bene fi t from Radiotherapy Statement of Search Strategies Used and Sources of Information,” Clin. Oncol., vol. 27, no. 10, pp. 561–569, 2015.

[5] D. G. Hirst and T. Robson, “Molecular biology : the key to personalised treatment in radiation oncology ?,” Br. J. Radiol., vol. 83, pp. 723–728, 2010.

[6] K. I. Altman and J. T. Lett, Eds., Relative Radiation Sensitivities of Human Organ Systems, Part III. Volume 15 of Advances in Radiation Biology Relative radiation sensitivities of human organ systems. Elsevier, 2016.

[7] S. J. Mcmahon, K. M. Prise, A. L. Mcnamara, J. Schuemann, and H. Paganetti, “A general mechanistic model enables predictions of the biological effectiveness of different qualities of radiation,” Sci. Rep., no. April, pp. 1–14, 2017.

[8] C. M. L. West, S. E. Davidson, S. A. Roberts, and R. D. Hunter, “Intrinsic radiosensitivity and prediction of patient response to radiotherapy for carcinoma of the cervix,” Br. J. Cancer, vol. 823, no. June, pp. 819–823, 1993.

[9] A. Brahme, Ed., Comprehensive Biomedical Physics. Volume 1: Nuclear Medicine and Molecular Imaging. Elsevier, 2014.

[10] M. Diem, A. Mazur, K. Lenau, J. Schubert, B. Bird, M. Miljković, C. Krafft, and J. Popp, “Molecular pathology via IR and Raman spectral imaging.,” J. Biophotonics, vol. 6, no. 11–12, pp. 855–86, Dec. 2013.

[11] K. Kong, C. Kendall, N. Stone, and I. Notingher, “Raman spectroscopy for medical diagnostics - From in-vitro biofluid assays to in-vivo cancer detection.,” Adv. Drug Deliv. Rev., Mar. 2015.

[12] R. La Rocca, G. C. Messina, M. Dipalo, V. Shalabaeva, and F. De Angelis, “Out-of-Plane Plasmonic Antennas for Raman Analysis in Living Cells,” Small, vol. 11, no. 36, pp. 4632–4637, 2015.

[13] F. M. Lyng, I. R. M. Ramos, O. Ibrahim, and H. J. Byrne, “Vibrational Microspectroscopy for Cancer Screening,” pp. 23–35, 2015.

[14] A. J. Popp, C. Krafft, M. Schmitt, I. Schie, D. Cialla-may, C. Matthaeus, and T. Bocklitz, “Label-free molecular imaging of biological cells and tissues by linear and non-linear Raman spectroscopic approaches,” Angew. Chem. Int. Ed. Engl., 2016.

[15] A. Maguire, I. Vega-Carrascal, J. Bryant, L. White, O. Howe, F. M. Lyng, and A. D. Meade, “Competitive evaluation of data mining algorithms for use in classification of leukocyte subtypes with Raman microspectroscopy,” Analyst, vol. 140, no. 7, pp. 2473–2481, 2015.

[16] H. J. Butler, L. Ashton, B. Bird, G. Cinque, K. Curtis, K. Esmonde-white, N. J. Fullwood, B. Gardner, P. L. Martin-, M. J. Walsh, M. R. Mcainsh, N. Stone, F. L. Martin, H. J. Butler, and P. L. Martin-hirsch, “Using Raman spectroscopy to characterize biological materials,” Nat. Protoc., vol. 11, no. 4, pp. 1–47, 2016.

[17] N. P. Damayanti, Y. Fang, M. R. Parikh, A. P. Craig, J. Kirshner, and J. Irudayaraj, “Differentiation of cancer cells in two-dimensional and three-dimensional breast cancer models by Raman spectroscopy.,” J. Biomed. Opt., vol. 18, no. 11, p. 117008, Nov. 2013.

[18] C. Krafft, K. Wilhelm, A. Eremin, S. Nestel, N. von Bubnoff, W. Schultze-Seemann, J. Popp, and I. Nazarenko, “A specific spectral signature of serum and

plasma-derived extracellular vesicles for cancer screening," Nanomedicine Nanotechnology, Biol. Med., vol. 13, no. 3, pp. 835–841, 2017.
[19] T. Tolstik, C. Marquardt, C. Matthäus, N. Bergner, C. Bielecki, C. Krafft, A. Stallmach, and J. Popp, "Discrimination and classification of liver cancer cells and proliferation states by Raman spectroscopic imaging.," Analyst, vol. 139, no. 22, pp. 6036–43, 2014.
[20] C. Krafft and V. Sergo, "Biomedical applications of Raman and infrared spectroscopy to diagnose tissues," vol. 20, pp. 195–218, 2006.
[21] D. Franco, S. Trusso, E. Fazio, A. Allegra, C. Musolino, A. Speciale, F. Cimino, A. Saija, F. Neri, M. S. Nicolò, and S. P. P. Guglielmino, "Spectrochimica Acta Part A : Molecular and Biomolecular Spectroscopy Raman spectroscopy differentiates between sensitive and resistant multiple myeloma cell lines," Spectrochim. Acta - Part A Mol. Biomol. Spectrosc., vol. 187, pp. 15–22, 2017.
[22] J. W. Chan, D. S. Taylor, T. Zwerdling, S. M. Lane, K. Ihara, and T. Huser, "Micro-Raman Spectroscopy Detects Individual Neoplastic and Normal Hematopoietic Cells," Biophys. J., vol. 90, no. 2, pp. 648–56, 2006.
[23] S. J. Harder, Q. Matthews, M. Isabelle, A. G. Brolo, J. J. Lum, and A. Jirasek, "A Raman spectroscopic study of cell response to clinical doses of ionizing radiation," Appl. Spectrosc., vol. 69, no. 2, pp. 193–204, 2015.
[24] S. J. Harder, M. Isabelle, L. Devorkin, J. Smazynski, W. Beckham, A. G. Brolo, J. J. Lum, and A. Jirasek, "Raman spectroscopy identifies radiation response in human non- small cell lung cancer xenografts," Sci. Rep., no. October 2015, pp. 1–10, 2016.
[25] Q. Matthews, A. Brolo, J. Lum, X. Duan, and A. Jirasek, "Raman spectroscopy of single human tumour cells exposed to ionizing radiation in vitro," Phys. Med. Biol., vol. 56, no. 1, pp. 19–38, 2011.
[26] M. Yasser, R. Shaikh, M. K. Chilakapati, and T. Teni, "Raman Spectroscopic Study of Radioresistant Oral Cancer Sublines Established by Fractionated Ionizing Radiation," PLoS One, vol. 9, no. 5, 2014.
[27] J. Z. Beer, E. B, E. Niepokojczycka, O. Rosiek, I. Szumiel, and M. Walicka, "Loss of Tumorigenicity during In Vitro Growth of L5178Y Murine Lymphoma Cells," Cancer Res., vol. 43, no. October, pp. 4736–4742, 1983.
[28] I. Szumiel, "L5178Y sublines: a look back from 40 years. Part 1: General characteristics," Int. J. Radiat. Biol., vol. 81, no. 5, pp. 353–365, 2005.
[29] M. G. Albrecht and J. A. Creighton, "Anomalously Intense Raman Spectra of Pyridine at a Silver Electrode," J. Am. Chem. Soc., vol. 99, pp. 5215–5217, 1977.
[30] G. Frens, "Controlled Nucleation for the Regulation of the Particle Size in Monodisperse Gold Suspensions," Nat. Phys. Sci., vol. 241, no. 105, pp. 20–22, 1973.
[31] Q. Zhang, X. Lu, P. Tang, D. Zhang, J. Tian, and L. Zhong, "Gold Nanoparticle (AuNP)-Based Surface-Enhanced Raman Scattering (SERS) Probe of Leukemic Lymphocytes," Plasmonics, pp. 1–8, 2016.
[32] A. M. Schrand, J. J. Schlager, L. Dai, and S. M. Hussain, "Preparation of cells for assessing ultrastructural localization of nanoparticles with transmission electron microscopy.," Nat. Protoc., vol. 5, no. 4, pp. 744–757, 2010.
[33] L. T. Kerr, J. Byrne, and B. M. Hennelly, "Optimal choice of sample substrate and laser wavelength for Raman spectroscopic analysis of biological specimen," Anal. Methods, vol. 0, pp. 1–12, 2015.
[34] K. Tsia, Understanding Biophotonics: Fundamentals, Advances and Applications. CRS press, 2016.
[35] F. LaPlant, "Lasers, Spectrographs, and Detectors," in Emerging Raman Applications and Techniques in Biomedical and Pharmaceutical Fields, P. Matousek and M. Morris, Eds. Springer, 2010, pp. 1–13.

[36] I. Notingher, S. Verrier, H. Romanska, a. E. Bishop, J. M. Polak, and L. L. Hench, “In situ characterisation of living cells by Raman spectroscopy,” Spectroscopy, vol. 16, no. 2, pp. 43–51, 2002.
[37] B. Kann, H. L. Offerhaus, M. Windbergs, and C. Otto, “Raman microscopy for cellular investigations − From single cell imaging to drug carrier uptake visualization ☆,” Adv. Drug Deliv. Rev., vol. 89, pp. 71–90, 2015.
[38] P. Lasch and J. Kneipp, Biomedical Vibrational Spectroscopy. Wiley, 2008.
[39] A. Downes and A. Elfick, “Raman spectroscopy and related techniques in biomedicine.,” Sensors (Basel)., vol. 10, no. 3, pp. 1871–89, Jan. 2010.
[40] I. W. Schie, L. Alber, A. L. Gryshuk, and J. W. Chan, “Investigating drug induced changes in single, living lymphocytes based on Raman micro-spectroscopy.,” Analyst, vol. 139, no. 11, pp. 2726–33, Jun. 2014.
[41] K. Hamada and K. Fujita, “Raman microscopy for dynamic molecular imaging of living cells,” vol. 13, no. August 2008, pp. 5–8, 2008.
[42] a. Rygula, K. Majzner, K. M. Marzec, a. Kaczor, M. Pilarczyk, and M. Baranska, “Raman spectroscopy of proteins: a review,” J. Raman Spectrosc., vol. 44, no. 8, pp. 1061–1076, Aug. 2013.
[43] A. Bankapur, E. Zachariah, S. Chidangil, M. Valiathan, and D. Mathur, “Raman tweezers spectroscopy of live, single red and white blood cells.,” PLoS One, vol. 5, no. 4, p. e10427, Jan. 2010.
[44] S. Corsetti, T. Rabl, D. McGloin, and G. Nabi, “Raman spectroscopy for accurately characterising biomolecular changes in androgen-independent prostate cancer cells,” J. Biophotonics, 2017.
[45] Q. Wang, S. D. Grozdanic, M. M. Harper, N. Hamouche, H. Kecova, T. Lazic, and C. Yu, “Exploring Raman spectroscopy for the evaluation of glaucomatous retinal changes.,” J. Biomed. Opt., vol. 16, no. 10, p. 107006, Oct. 2011.
[46] I. Rocha-Mendoza, D. R. Yankelevich, M. Wang, K. M. Reiser, C. W. Frank, and A. Knoesen, “Sum frequency vibrational spectroscopy: the molecular origins of the optical second-order nonlinearity of collagen.,” Biophys. J., vol. 93, no. 12, pp. 4433–44, Dec. 2007.
[47] S. Managò, C. Valente, P. Mirabelli, D. Circolo, F. Basile, D. Corda, and A. C. De Luca, “A reliable Raman-spectroscopy-based approach for diagnosis, classification and follow-up of B-cell acute lymphoblastic leukemia,” Sci. Rep., vol. 6, no. April, p. 24821, 2016.
[48] J. Zhu, J. Zhou, J. Guo, W. Cai, B. Liu, Z. Wang, and Z. Sun, “Surface-enhanced Raman spectroscopy investigation on human breast cancer cells.,” Chem. Cent. J., vol. 7, no. 1, p. 37, Jan. 2013.
[49] F. Wei, D. Zhang, N. J. Halas, and J. D. Hartgerink, “Aromatic amino acids providing characteristic motifs in the Raman and SERS spectroscopy of peptides.,” J. Phys. Chem. B, vol. 112, no. 30, pp. 9158–64, Jul. 2008.
[50] J. M. Benevides, S. A. Overman, and G. J. Thomas, “Raman , polarized Raman and ultraviolet resonance Raman spectroscopy of nucleic acids and their complexes,” pp. 279–299, 2005.
[51] Z. Movasaghi, S. Rehman, and I. U. Rehman, “Raman Spectroscopy of Biological Tissues,” Appl. Spectrosc. Rev., vol. 42, no. 5, pp. 493–541, Sep. 2007.
[52] S. Casabella, P. Scully, N. Goddard, and P. Gardner, “Automated analysis of single cells using Laser Tweezers Raman Spectroscopy,” Analyst, pp. 689–696, 2016.
[53] C. Matthäus, B. Bird, M. Miljković, T. Chernenko, and M. Romeo, “Infrared and Raman Microscopy in Cell Biology,” Methods Cell Biol., vol. 89, no. 8, pp. 275–308, 2008.
[54] A. Maguire, I. Vegacarrascal, L. White, B. McClean, O. Howe, F. M. Lyng, and A. D. Meade, “Analyses of Ionizing Radiation Effects In Vitro in Peripheral Blood

Lymphocytes with Raman Spectroscopy," Radiat. Res., vol. 183, no. 4, pp. 407–416, 2015.
[55] P. Greaves, Histopathology of Preclinical Toxicity Studies: Interpretation and Relevance in Drug Safety Evaluation, Third edit. Academic Press, 2007.
[56] A. J. Hobro, Y. Kumagai, S. Akira, N. I. "Raman spectroscopy as a tool for label-free lymphocyte cell line discrimination," Analyst, vol. 384, p. ec186, 2016.
[57] I. Szumiel, "L5178Y sublines: a look back from 40 years. Part 2: response to ionizing radiation.," Int. J. Radiat. Biol., vol. 81, no. 5, pp. 353–365, 2005.
[58] D. Ghosh, D. Sarkar, A. Girigoswami, and N. Chattopadhyay, "A fully standardized method of synthesis of gold nanoparticles of desired dimension in the range 15 nm-60 nm.," J. Nanosci. Nanotechnol., vol. 11, no. 2, pp. 1141–1146, 2011.
[59] N. G. Bastús, J. Comenge, and V. Puntes, "Kinetically controlled seeded growth synthesis of citrate-stabilized gold nanoparticles of up to 200 nm: Size focusing versus ostwald ripening," Langmuir, vol. 27, no. 17, pp. 11098–11105, 2011.
[60] N. D. Israelsen, C. Hanson, and E. Vargis, "Nanoparticle Properties and Synthesis Effects on Surface-Enhanced Raman Scattering Enhancement Factor : An Introduction," vol. 2015, 2015.
[61] I. Aguilar-hernández, N. Kristian, T. López-luke, F. F. Contreras-torres, J. Petter, and N. Ornelas-soto, "Vibrational Spectroscopy Surface enhanced Raman spectroscopy of phenolic antioxidants : A systematic evaluation of ferulic acid , p - coumaric acid , caffeic acid and sinapic acid," vol. 89, pp. 113–122, 2017.
[62] a. J. Caires, R. P. Vaz, C. Fantini, and L. O. Ladeira, "Highly sensitive and simple SERS substrate based on photochemically generated carbon nanotubes–gold nanorods hybrids," J. Colloid Interface Sci., vol. 455, pp. 78–82, 2015.
[63] A. Ravindran, P. Chandran, and S. S. Khan, "Biofunctionalized silver nanoparticles: Advances and prospects," Colloids Surfaces B Biointerfaces, vol. 105, no. August 2012, pp. 342–352, 2013.
[64] S. Agnihotri, S. Mukherji, and S. Mukherji, "Size-controlled silver nanoparticles synthesized over the range 5–100 nm using the same protocol and their antibacterial efficacy," RSC Adv., vol. 4, no. 8, pp. 3974–3983, 2014.
[65] D. Cialla, A. März, R. Böhme, F. Theil, K. Weber, M. Schmitt, and J. Popp, "Surface-enhanced Raman spectroscopy (SERS): progress and trends.," Anal. Bioanal. Chem., vol. 403, no. 1, pp. 27–54, Apr. 2012.
[66] A. Samanta, S. Jana, R. K. Das, and Y.-T. Chang, "Wavelength and shape dependent SERS study to develop ultrasensitive nanotags for imaging of cancer cells," RSC Adv., vol. 4, no. 24, p. 12415, 2014.
[67] K. Kneipp, A. S. Haka, H. Kneipp, K. Badizadegan, N. Yoshizawa, C. Boone, K. E. Shafer-Peltier, J. T. Motz, R. R. Dasari, and M. S. Feld, "Surface-enhanced raman spectroscopy in single living cells using gold nanoparticles," Appl. Spectrosc., vol. 56, no. 2, pp. 150–154, 2002.
[68] O. V Bondar, D. V Saifullina, I. I. Shakhmaeva, I. I. Mavlyutova, and T. I. Abdullin, "Monitoring of the Zeta Potential of Human Cells upon Reduction in Their Viability and Interaction with Polymers," Acta Naturae, vol. 4, no. 12, pp. 78–81, 2012.
[69] I. Szumiel, "From radioresistance to radiosensitivity : In vitro evolution of L5178Y lymphoma," Int. J. Radiat. Biol., vol. 91, no. 6, pp. 1–7, 2015.
[70] J. Talukdar, M. C. Kalita, and B. C. Goswami, "Influence of Dissolved Inorganic Carbon and Nitrogen Sources on Growth , Total Lipid Content and Calorific Value of the Freshwater Oleaginous Microalgae Ankistrodesmus falcatus (Corda) Ralfs," vol. 3, no. 3, pp. 14–25, 2012.
[71] M. D. Ralston and R. C. Howe, "Experimental Cell Research 123 (1979) 237-245," vol. 123, 1979.

Chapter 7

Conclusion

7. Conclusion

7.1. Contributions

Detection of molecules of interest

- A comprehensive and systematic evaluations of different synthesis parameters of silver nanoparticles was carried out, which helped select the adequate synthesis conditions that ensure the highest enhancement capability. PCA analysis was employed to cluster silver colloids prepared using different synthesis parameters, and SERS enhancement of colloids was studied with a test molecule (glycine). The selected colloidal solution was used for detection of phenolic antioxidant at low concentrations ($2.5x10^{-9}$M). For *p*-coumaric acid and caffeic acid, these low detections were reached for the first time. In previous reports limits of detection are within the range of 10^{-3} to 10^{-4} M. In addition, SERS analysis of SA using silver colloids was carried out for the first time.

- A novel SERS-active substrate was obtained by using carbon nanofibers (CNFs). Chemical modification of CNFs allowed the immobilization of AUNPs providing good nanoparticle coverage, including non-superficial layers. SERS enhancement was tested with Rh110, reaching a 1×10^{-6} M detection limit, which was high but help set the basis for further modification of the substrate.

Analysis of cellular systems

- Biochemical changes caused by the interaction of CdTe quantum dots with the freshwater microalgae *H. pluvialis* in stressed and non-stressed stage were detected via SERS. It was determined that CdTe@TGA QDs interact with *H. pluvialis* after 5 minutes of exposure. *H. pluvialis* in non-stressed stage was more vulnerable to CdTe@TGA QDs. SERS enhancements were obtained using AuNPs, and SERS spectra showed changes in non-stressed *H. pluvialis* cells, specially in bands associated to chlorophyll. No changes were detected in stressed cells after incubation with QDs. The effect of the interaction of QDs with *H. pluvialis* was reported for the first time.

- SERS analysis of HeLa cells was achieved using a multilayer solid substrate formed by 3 layers of gold nanospheres and a final layer of gold nanocubes (GNCS). Significant enhancements in the SERS spectra were observed, and bands with very high resolution were obtained, similar to those reported using substrates fabricated with more complex methods.

  The substrates fabricated by a self-assembly method generated high enhancement of important marker bands and could help the qualitative analysis of biological tissues. Since the substrates are glass based, biological samples can be immobilized, smeared or anchored if necessary. Few works have addressed the use of this kind of substrate for cell analysis.

The comprehensive Raman and SERS characterization of a radioresistant (LY-R) and radiosensitive (LY-S) murine lymphoma cell line was carried out. This is the first work exploring the vibrational spectroscopy characterization of the radioresistant (LY-R) and radiosensitive (LY-S) murine lymphoma sublines. Normal Raman analysis provided important information about chemical the constituents of both sublines, despite the lack of separation observed by preliminary principal component analysis (PCA).
So far, SERS was successfully used to enhance Raman spectra, and promising preliminary results obtained with PCA showed a clear separation between sublines incubated with AuNPs.
Despite overlapping of confidence ellipses for SERS spectra obtained with AgNPs, other chemometric methods might be able to discriminate between sublines. Future work will focus on the analysis of specific truncated spectral regions, improvement of spectral acquisition, and the application of different chemometric techniques for the differentiation of both sublines. Also, further studies will be carried out to evaluate possible differences in nanoparticle-cell interaction presented by the LY-R and LY-S sublines.

7. 2. General conclusions

Nanostructured substrates fabricated by wet-chemical synthesis methods were SERS active and allowed the label-free detection of single molecules of interest, as well as complex biological samples (microalgae and mammalian cell lines). The developed SERS substrates are viable for biochemical and chemical sensing applications.